



UNIVERSITÀ DEGLI STUDI DI TRIESTE

XXIX CICLO DEL DOTTORATO DI RICERCA IN

NANOTECNOLOGIE

**Photoionization Experiments In The Study
Of Energy Transfer In Nanostructured
Materials And Their Precursors**

Settore scientifico-disciplinare: CHIM/02 CHIMICA FISICA

**DOTTORANDO
CESARE GRAZIOLI**

**COORDINATORE
PROF. LUCIA PASQUATO**

**SUPERVISORE DI TESI
PROF. GIOVANNA FRONZONI
DR. MARCELLO CORENO**

ANNO ACCADEMICO 2015/2016

Contents

Abstract	v
Acknowledgements	vii
List of Abbreviations	ix
1 Introduction: molecules in material science	1
2 Photoionization and photoexcitation experiments	7
2.0.1 Background	7
2.0.2 Photoelectron Spectroscopy	10
2.0.3 X-ray Absorption Spectroscopy	13
2.0.4 Interpretation of NEXAFS	15
2.0.5 Experiments vs theory	17
2.1 Synchrotron based photoionization studies	20
2.1.1 Synchrotron radiation	20
2.1.2 Beamline Gas Phase at ELETTRA	21
2.1.3 Beamline I311 and D1011 at MAX-II	22
2.2 Detectors and spectrometers	24
2.2.1 Total ion or electron yield	24
2.2.2 Electron energy analyzer	27
2.2.3 ULLA, and end station for high resolution measurements at GasPhase	29
3 Electronic structure of organic molecules	39
3.1 Oligothiophenes	40
3.1.1 Introduction	40
3.1.2 Photoemission	41
3.1.3 C <i>K</i> -edge NEXAFS	45
3.2 The electronic characterization of biphenylene	54
3.2.1 Introduction	54
3.2.2 Isolated biphenylene molecule - valence and core-levels	57

3.2.3	Band structure and molecular orientation of biphenylene films	62
3.3	Vibronic contribution in pyridines	72
3.3.1	Theoretical aspects	72
3.3.2	Experimental and theoretical results	73
4	Transition metal macrocyclic compounds	87
4.1	The role of the central atom in transition metal phthalocyanines	89
4.1.1	Experimental and computational details	91
4.1.2	Experimental results	93
4.2	Grafting of double decker phthalocyanines on Si(100)-2×1	99
4.2.1	LuPc ₂ on passivated Si(100)-2×1:H	100
4.2.2	LuPc ₂ on pristine Si(100)-2×1	111
5	Mapping out the future: the new generation sources	121
5.1	CITIUS: an IR-XUV light source for ultrafast science	123
5.1.1	The laser system and the beamline	124
5.1.2	HHG performance	127
5.1.3	Characterization of harmonic pulse duration	129
5.1.4	Ultrafast demagnetization of permalloy	131
5.2	Low Density Matter beamline at FERMI	133
5.2.1	Introduction	133
5.2.2	Photon transport system	133
5.2.3	Commissioning and present status of the beamline	136
6	Conclusions and perspectives	139
6.1	Experiments with novel light sources	141
	List of papers	145

Abstract

This thesis deals with the study of the electronic structure of substances relevant to molecular materials technology. Detailed investigations were carried out by means of core and valence photoionization spectroscopy (Near-Edge X-ray Absorption Fine Structure, NEXAFS and PhotoEmission Spectroscopy, PES), supported by Density Functional Theory (DFT) calculations. An approach similar to the “bottom-up” strategy was adopted, starting from the study of the simpler molecular building blocks as model systems and increasing complexity to larger molecular systems and deposited films.

In the first part, three simple organic systems were characterized in detail. A systematic study of oligothiophenes was performed as a function of the chain length. The evolution of the C1s NEXAFS spectral features is analyzed as a function of the number of thiophene rings; a tendency to a stabilization for increasing chain length is found. Theoretical computation assisted in the assignment of PES core hole peaks to the different carbon sites on the basis of both the inductive effects generated by the presence of the S atom, as well as of the aromaticity. For biphenylene, a small antiaromatic molecule proposed also as building block for novel 2D materials, the characters of the non-equivalent carbons were separated in gas phase core hole spectra. The growth on a metallic substrate [Cu(111)] was also studied. The adsorbed biphenylene film is characterized by important intermolecular interactions but maintains, substantially, a molecular character. The molecules choose an ordered arrangement and switch their orientation from lying to standing on the surface for increasing coverage. In the study of pyridines and fluorinated derivatives the contributions of molecular vibrations were added in the analysis and simulation of the NEXAFS experiments at the N *K* and at the C *K* edges. This study is particularly appealing in view of its sufficient reliability and low computational cost of our computational protocol that calculates band positions with Time-Dependent DFT and Transition Potential DFT.

The second part is dedicated to Transition Metal Phthalocyanines (TM-Pc's), which are systems of higher complexity than the previous ones. They are widely studied for the possibility to deposit them in molecular films suitable for a variety of technological applications. Fe- and Mn- Pc's were chosen since the different metal in the molecular center gives rise to Highest Occupied Molecular orbitals (HOMO) with different atomic characters. Our analysis reveals that the electronic structure of the Pc molecules rises from the combination of orbitals of all the atoms in the molecule - carbon, nitrogen and the metal in the molecular center - and that the HOMO and HOMO-1 features depend on the hybridization between the metal atom and mostly C $2p$ and N $2p$ orbitals.

In the third part, a parallel research activity towards the development of novel light sources in view of their application for time resolved photoionization studies of energy transfer processes in novel materials. First the main features of CITIUS, a new light source for ultrafast science is presented. CITIUS provides tunable, intense, femtosecond pulses in the spectral range from infrared to extreme ultraviolet (XUV). The generated pulses (about $10^5 - 10^8$ photons/pulse in the range 14-80 eV) are produced by laser induced high- order harmonic generation (HHG) in gas and then monochromatized by a time preserving monochromator. We present the results of two pump-probe experiments: one to characterize the temporal duration of harmonic pulses; the second one to demonstrate the capability for selective investigation of the ultrafast dynamics in a magnetic compound. Secondarily, the Low Density Matter (LDM) beamline is described. LDM has been built as part of the FERMI free electron laser (FEL) facility to serve the atomic, molecular and cluster physics community. The LDM beamline was designed for experiments with supersonic beams of atoms, molecules or clusters to explore nonlinear multiple ionization processes and energy redistribution processes after photoexcitation. The LDM beamline is ideal for performing experiments over a broad range of topics (e.g. photofragmentation or even ultrafast demagnetization) particularly because of its ability to take advantage of the full control of the FEL pulse polarization. The design and characterization of the LDM photon transport system is described, detailing the optical components of the beamline.

Acknowledgements

Omnia vincit amor
(*Love conquers all*)
(Vergilius, Eclogues, Book X, line 69)

Our hearts are drawn to stars
Which want us not.
(Edgar Lee Masters, Spoon River Anthology)

Io non c'ho una lira, io c'ho solo possibilità!
(Marcello Coreno)

First of all I want to thank my supervisor Prof. Giovanna Fronzoni, for accepting me as a PhD student, for being a support and for her suggestions. And for the effort, by Mauro Stener and her, to try and to teach me DFT. Secondarily I want to thank Monica de Simone for providing me always with major help: during the experiments, in the analysis, and in the thankless job of correcting the first draft of this thesis. My thanks go also to the staff of Gas Phase beamline: Kevin, Robert, Michele. Thank you for bearing all the mess that I was doing. And to Antti Kivimäki, who is now in Sweden: see you soon! I want to thank also Carlo Callegari for the opportunity to participate to the first heroic experiments at the beginning of the activities at LDM; and for the patience in waiting the paper about the optical transport of the beamline. A thank also to the staff of LDM, Oksana and Paola, who had already been colleagues of mine and with whom I was pleased to collaborate once more. A special thank also to Michele Di Fraia: you will always be my senior PhD! And I want to thank also the members of the CITIUS group: Prof. Giovanni De Ninno and Dr. Barbara Ressel of the University of Nova Gorica and Dr. Carlo Spezzani of Elettra. Giovanni invited me to join his group and to take part in the construction of the CITIUS laboratory, together with Carlo, who was already a long-standing friend. The laboratory was moved to the department of Ajdovščina where it is operating, thanks also to

the determination and the skills of Barbara. I thank also the people of the IFN in Padua, part of the CITIUS collaboration: Luca Poletto, Fabio Frassetto and Paolo Miotti. I am always pleased to collaborate with you, since that terrible November in Padua when Fabio and I were mounting the monochromator of CITIUS in the complete or semi-darkness. And I am always happy to host Paolo when he comes to Trieste. (someone said that when I am with Paolo and Michele D.F. I look like “*Madonna with her boys*”... well, that must be due to my instinctive body language)

At this point I thank from my heart Carla Puglia and her division at the University of Uppsala. Carla is a great woman with a big heart and I still miss the four months that I spent with her in Uppsala and with her collaborators: Teng and Valeria. And I miss the beamtimes with them in Lund at MaxLab together with Ieva Bidermane and Roberta Totani. I rarely had so much fun during beamtimes, while drinking coffee, chewing wasabi nuts and working till collapsing! Luckily Copenhagen was close by, where I could load my energies (thank you so much, Nis!). In Uppsala I could also work close to Barbara Brena and Johann Lüder; I send a special thank to them. A special thank also to Nadine Witkowski, with whom I had two fruitful beamtimes in Lund. I look forward to collaborate with her again. And many thanks also to Ambra Guarnaccio and Antonio Santagata, two other great collaborators with whom having beamtimes at Gas Phase appears cheerful... and that’s something! Finally a big, big thank to Marcello Coreno. I thank him for supporting, supervising and also for (sometimes) tormenting me. Without him I would have never made it through.

But there is another group of people that I must thank. I thank the Generous Lenders from the deep of my heart. These are all the people in Elettra, Fermi, MaxLab, Uppsala etc. who - willingly or not - lent to me the components that sometimes I was urgently needing: flanges, adapters, copper or viton gaskets, manipulators etc. Thank you, Generous Lenders. Should you ever read my thesis you will see that your generosity (and your loans) helped me in building one laboratory, one beamline and one end station to perform the experiments discussed here... and many more to come. You are more than welcome to join, but don’t expect to ever have them back.

List of Abbreviations

BE	Binding energy
DOS	Density of States
DFT	Density Functional Theory
EF	Fermi energy
EELS	Electron energy loss spectroscopy
FEL	Free electron LASER
FWHM	Full width at half maximum
He I	Helium I light (21.2 eV)
He II	Helium II light (40.8 eV)
HH	Higher harmonic
HOMO	Highest Occupied Molecular orbitals
IPL	In-plane polarization
LUMO	Lowest Unoccupied Molecular orbitals
MO	Molecular orbitals
OPL	Out-of-plane polarization
Pc	Phthalocyanine

pDOS	Partial density of states
PES	Photoemission spectroscopy
SOMO	Semi-occupied molecular orbital
SR	Synchrotron radiation
SUMO	Semi-unoccupied molecular orbital
TD-DFT	Time-Dependent Density Functional Theory
tDOS	Total density of states
TEY	Total electron yield
TM	Transition metal
DFT-TP	Density Functional Theory in the Transition-Potential approach
NEXAFS	Near edge X-ray absorption fine structure spectroscopy
VB	Valence band
VE	Vertical energy
XPS	X-ray photoemission spectroscopy

Chapter 1

Introduction: molecules in material science

Brevis esse laboro, obscurus fio
(It is when I struggle to be brief that I become obscure)
(Horace)

The word “molecule” dates back to the 18th century and comes from the diminutive of Latin *moles* “mass, barrier”, in the sense of “extremely minute particle”. It defines a group of atoms that form the smallest identifiable unit into which a pure substance can be divided. While the size of device components in modern technology is gradually decreased, single molecules have been considered as potential future systems in molecular technology, as pointed out by R. Feynman [1]. In his lecture, Feynman envisaged the use of single atoms or molecules in a totally new way of design, and in fact recently a molecule transistor [2] and even a single atom transistor [3] have been demonstrated.

However, the realization of single molecule industrial applications is still a long way off, and in this prospect a key issue is the use of molecules as building blocks for electronic devices because they offer an almost infinite pool of geometries and functional groups. The growth and characterization of novel materials based on the assembly of molecular components on proper surfaces or substrates is nowadays an extremely active and expanding field [4]. The possibility to manage the available length scales and structural complexities via organic chemistry methodologies and the creative assembly of the diverse components can thus lead to unique behaviors [5]. On the other hand, by decreasing the size of devices new effects come into play, whose study is essential to determine a higher degree of

miniaturization.

A consequence of the complexity is the need for various tools for materials characterization, and theoretical analysis. Some technologically useful properties may be derived by the properties of the molecule or ion, or by a cooperative solid-state property, via molecule-molecule or molecule-substrate interaction. Hence, characterizing the properties of isolated molecules as well as their competitive interactions in the solid state is essential to predict, control, and manipulate such behaviors.

This thesis work presents the results of three “investigations”, where the term refers to a group of experiments associated together for their arguments. Even though these investigations may look heterogeneous, they blend together as the steps of a larger experimental project, which is to characterize molecules as isolated particles, molecular monolayers or films adsorbed on surfaces. These films constitute the foundation for a wide range of possible applications: from model system studies to devices for sensing, catalysis, energy conversion or optoelectronic components.

The original nucleus of this thesis was centered on the characterization of molecules in the gas phase - which is still a particularly challenging study. The context of this research was calling for the coupling of a state-of-the-art electron spectrometer with a well developed molecular vapors source, to a tunable photon source of high flux and good energy resolution. The realization of this facility - the assembly of ULLA and the coupling to the Gas Phase beamline - was carried out at the very beginning of this work and is extensively described in Chapter 2 together with all main experimental details. It laid the ground for planned experiments exploiting its high performances, whose description provide most of the motivation for this thesis, and extends throughout all the other chapters.

X-ray spectroscopies are here applied for the experimental determination of the electronic structure of substances important for technology, with an emphasis on carbon based molecules. The investigations presented fall within the following fields of research: (1) gas-phase molecular spectroscopy, (2) photoemission and absorption study of molecular film, and (3) laser-induced reactions on molecules in gas phase. The approach adopted is similar to the “bottom-up” strategy. This strategy is one of the two general roads followed to produce nanomaterials, that uses atoms or molecules as starting building blocks and let them organize or assemble into higher order structures, and is opposite to the so-called “top-down” approach. In a similar way, this work deals first with the study of the very first building blocks studied as isolated molecules (i.e. the model

system) and is carried on further with increasing complexity. The scientific goal of the project is important in the context of research on non bulk-like properties of nanostructures, which can provide the inspiration for the development of new nanostructured materials. This project, although oriented to basic research, responds to a fundamental need in the science to create collections of reliable and detailed data about the properties of their building blocks, i.e. the molecules and the clusters.

Photons in the soft X-ray spectral region (50eV to 2.5keV) are well matched for reaching core level resonances in most elements. For lighter elements, such as carbon, nitrogen and oxygen, the innermost energy level ($1s$) can be reached and for heavier elements like $3d$ transition metals one could use the second or even the third level, $2p$ and $3d$. Core levels of different elements have specific energies and are well separated from each other. These core levels may shift in energy depending on the chemical environment of the atoms. But the largest effect is felt by the outermost electronic states (valence electrons) in the atoms as they will rearrange upon chemical bonding between atoms. Core and valence excitations are used to investigate the bonding mechanism between atoms in molecules or between molecules and other condensed materials, and they are interpreted and modeled in terms of quantum mechanical models.

An example of this approach is the study of short chain thiophene molecules, discussed in Sec. 3.1. In the field of organic electronic devices the thiophene based polymers and oligomers have been particularly investigated and frequently used for their unique electronic, optical and redox properties [6]. The high polarizability of the sulphur atom in the rings stabilizes the conjugated chain conferring excellent charge transport properties which are of fundamental importance for applications in organic and molecular electronics. In this sense, several works pointed out that in films of short chain thiophenes the chain length and morphology strongly influence the side chain packing and interdigitation [7, 8]; thus they can influence the supramolecular arrangement leading to high performance devices or, on the contrary, to small domains and poor performances. In spite of this findings, that are extremely important for the application of polythiophene derivatives in organic and molecular electronics, a systematic study of the electronic structure and charge dynamics in short chain thiophenes - starting from the most simple building blocks and increasing the complexity by adding more and more components - is still missing.

A similar approach, looking for the differences in the electronic structure at the increasing complexity of the system, has been used

in the study of biphenylene molecules and surfaces. Biphenylene is a small anti-aromatic molecule similar to naphthalene that has been suggested to be a building block for a possible new 2D material [9, 10, 11]. It was first characterized in the isolated form in a joint experimental and theoretical work that allowed to separate the character of the different carbons (Sec. 3.2.2). In a second step, the growth on a metallic substrate and the orientation as a function of the film thickness were characterized (Sec. 3.2.3). Another step of increasing complexity will include also a first attempt to analyze the contributions of molecular vibrations in the experimental data of pyridine, 2-fluoropyridine, and 2,6-difluoropyridine. This method is accurate enough for a general description of the spectra, and is illustrated in Sec. 3.3.

Chapter 4 is dedicated to phthalocyanines, larger molecular systems that are widely studied for the possibility to deposit them in supramolecular architectures suitable for a variety of technological applications. This chapter is in fact more dedicated to films. In Section 4.1 the role of the central atom in phthalocyanines is investigated in detail in free molecules and also in films by studying the low-energy region of their valence band. Metal phthalocyanines are compared to the metal-free one; their atomic orbital composition is analyzed experimentally, by making use of the variation in photoionization cross-sections with photon energy, and theoretically, by means of density functional theory. The atomic character of the Highest Occupied Molecular Orbital (HOMO), reflected on the energy region of the outermost valence band, is different particularly for MnPc as compared to the other two molecules. Section 4.2 shows an investigation of lutetium double-decker phthalocyanines deposited on silicon. Silicon is one of the most widely studied materials due to its use in technologically advanced areas. There have been numerous studies, experimental as well as theoretical, carried out to characterize the surfaces of Si [12, 13] and its interactions with different types of adsorbates [14, 15, 16, 17]. These studies are of interest due to the complex processes that happen at the interface between the substrate and the adsorbate. The adsorption can induce different phenomena like charge redistribution, in both substrate and adsorbate. The goal of this study is to investigate the adsorption as well as the interaction of LuPc₂ on pristine silicon Si(100)-2 × 1 (pristine Si) as compared to passivated silicon and to identify the changes in the molecular features and electronic structure induced by the substrate.

As already mentioned, an important part of this work was devoted to the activity of instrument development. First of all the im-

provement in the techniques of photoemission and photoabsorption have been very important for the collection of the data described in the text, as it is illustrated in detail throughout chapter 2; the obtained detection power has allowed to characterize the electronic states under investigation. On the other hand the access to ultrafast laser sources like FERMI and CITIUS-Lab (section 5.1 and 5.2) have provided the experience in the techniques of temporal correlation and made possible the development of pump-probe set-ups for the study of the temporal evolution of the photoelectron signal. This will represent a further improvement in the investigation of novel materials, because it is a direct measure of the electronic energy transfer, in the domain of picoseconds when coupled to synchrotron radiation and in the ultrafast femtosecond domain radiation photoemission in the Free Electron Laser (FEL).

Chapter 6 summarizes the achievements and draws the future perspectives. The most important stimulus to this thesis work has been the large collaboration, that has extended the initial project - studying the molecular building blocks in gas phase - to the investigation of the electronic structure of films and to time resolved pump-probe experiments. The results of this collaboration are reported linearly and divided by arguments in the following chapters, while actually they evolved in the years spontaneously and sometimes unexpectedly. An example is the aforementioned realization of ULLA (Section 2.2.3, that was used successfully at Gas Phase for state of the art experiments in gas phase (Chapters 3 and 4), but served also as test end station for the characterization of CITIUS light source (Section 5.1). In turns, the experience gained with the characterization of CITIUS was extremely useful when testing the performances of LDM beamline (Section 5.2).

At the end of the thesis the publications released during the doctoral activity are listed. The items from **PAPER I** to **PAPER VIII** provide the material discussed here.

Chapter 2

Photoionization and photoexcitation experiments

2.0.1 Background

Photoionization and photoexcitation experiments are traditionally used for investigating the energy distribution of electronic states (electronic structure) in atoms, molecules, and solids. The techniques are based on the interaction of photons with a well defined energy $h\nu$ and the electrons surrounding the atoms, either by exciting the system or by removing an electron from the system. The atom (or molecule) A is provided with additional energy which causes the transition from the ground state to an energetically higher state.

Photoionization involves the ejection of electrons from atoms or molecules following bombardment by monochromatic photons (Fig 2.1). If $h\nu$ is higher than the *ionization potential* IP of the electron (the minimum energy required to extract an electron from its orbital) the latter gets excited into the continuum via the photoelectric effect.



The ejected electrons e_{ph}^- are called photoelectrons and a minimum photon energy, known as ionization threshold, is required to remove an electron from an atom or a molecule. As the photon energy increases, the kinetic energy of the ejected electrons also increases linearly.

Photons with energy below the ionization threshold can still be absorbed, but in this case a bounded electron is moved to an empty

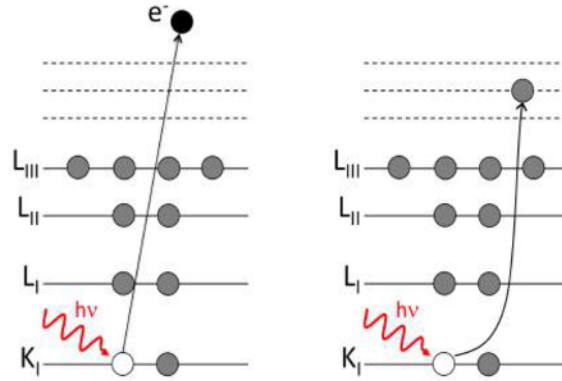


Figure 2.1: Photoionization (left) and photoexcitation (right)

orbital and the atom or molecule is left in a neutral excited state (Fig 2.1). This process is called *resonant photoexcitation* or *resonant photoabsorption*.



In general, the probability per unit time of a transition between an initial state $|i\rangle$ and a final state $|f\rangle$ is given by the *Fermi Golden Rule*:

$$\Gamma_{i \rightarrow f} = \frac{2\pi}{\hbar} |\langle i | \bar{V} | f \rangle|^2 \delta(E_i - E_f + h\nu) \quad (2.3)$$

where E_i and E_f are the electron energies in the initial and final states, while the term of $\delta(E_i - E_f + h\nu)$ function derives from the conservation of energy after the absorption of a photon $h\nu$. \bar{V} is the operator describing the interaction between radiation and matter and it can be written as an infinite sum of increasingly complex terms $\bar{V} = \bar{V}_1 + \bar{V}_2 + \dots$ accounting for processes with one photon, two photons and so on. In the following only one photon processes will be taken into account; two or more photon processes will be mentioned only in Sections 5.1 and 5.2.

\bar{V} can be further approximated if we assume that the transition is driven by a harmonic time dependent perturbation of the form $\hat{\epsilon}(e^{-i(\omega t - \mathbf{k}\mathbf{r})} + e^{-i(\omega t + \mathbf{k}\mathbf{r})})$ which corresponds to a monochromatic plane wave with polarization unit vector of the photon electric field $\hat{\epsilon}$. By applying the time dependent perturbation theory and introducing the *dipole approximation*, the resulting expression for the transition

Table 2.1: Excitation energies in eV of many important elements studied here; core levels were taken from Ref. [18] while absorption edges were taken from [19].

	1s core levels	<i>K</i> edges
B	189	193
C	285	284
N	398 (BN)	410 (gas)
O	531 (Al ₂ O ₃)	536 (gas)
	2p core levels	<i>L</i> edges
S	164 - 165	163
Mn	639 - 650	284
Fe	707 - 720	707
Co	778 - 793	536

probability is:

$$\Gamma_{i \rightarrow f} = \frac{2\pi}{\hbar} |\langle i | \hat{\epsilon} \cdot \mathbf{r} | f \rangle|^2 \delta(E_i - E_f + h\nu) \quad (2.4)$$

From Eq. 2.4 the absorption cross section¹ σ can be derived

$$\sigma = 4\pi^2 \alpha \omega \hbar |\langle i | \hat{\epsilon} \cdot \mathbf{r} | f \rangle|^2 \delta(E_i - E_f + h\nu) \quad (2.5)$$

Photoionization and photoexcitation techniques are extremely useful because they can point out important informations about the material under investigation, like its chemical, physical and electronic state. Moreover they can also turn on atomic and molecular processes and allow us to study their dynamics.

Many electronic core transitions of the most abundant elements, like resonances and spectral edges of elements with low or intermediate atomic numbers Z have energies that fall in the soft X-rays region (between 100 and 2000 eV). The 1s and 2p core level excitations of many important elements lie below 1000 eV (see Table 2.1). For an explanation of the labeling for absorption edges, see Section 2.0.3. This implies that the energy range covered at the synchrotron soft X-rays beamlines like the ones described further on (see section 2.1.2) is useful to provide a sensitive instrument for elemental characterization. On a less versatile level, they are also available from anode sources that use Mg or Al $K\alpha$ emission lines (1253.6eV and 1486.6eV, respectively).

Since soft X-rays are strongly absorbed in many materials, experiments need conditions of ultra high vacuum (UHV) to be performed. At the synchrotron radiation laboratories plenty of soft

¹The absorption cross section σ is a measure for the probability of an absorption process. σ has units of cm² molecule⁻¹, see Eq. 2.9. In the older literature, the absorption coefficient is sometimes given in base 10 and molar units, in which case it is given the symbol ϵ

x-rays spectroscopies have been developed, using synchrotron radiation as excitation source. These techniques are employed on a variety of specimens ranging from atoms and molecules in gas and liquid phases, to solid materials like metals, semiconductors and insulators, just to mention a few.

2.0.2 Photoelectron Spectroscopy

PhotoElectron Spectroscopy (often referred to as PES) is based on the photoelectric effect sketched in Fig.2.1 (left), where an electron is photoionized. During a PES experiment a diagram of the kinetic energy distribution of the photoemitted electrons is collected, and this is what we call a ‘PE spectrum’. In a schematic one-electron picture, which means that the interaction of the photoelectron with the remaining electrons of the system is neglected², the process can be described by the following relation that derives from the energy conservation:

$$E_B = h\nu - E_K - \phi \quad (2.6)$$

where E_B is the binding energy of the electron in the initial state, $h\nu$ is the photon energy, E_K is the kinetic energy of the photoemitted electron, and ϕ is an energy reference that depends on the experimental conditions. In gas phase measurements the energy are referred to the vacuum level and $\phi = 0$. When measuring surfaces the energies are referred to the Fermi edge of the system, ϕ is non zero quantity called ‘work function’, and it is a property of the sample[21].

The photoemission technique is divided into subtechniques depending on the energy range of the incident photons. For example, XPS uses x-rays as the incident photons (typically $h\nu$ about 1000 eV) and is useful to investigate at the strongly bound core electrons for elemental analysis. Ultraviolet photoelectron spectroscopy (UPS) utilizes UV light (typically from gas discharge lines $h\nu < 50$ eV) and is useful for investigating the valence and weakly bound core electrons. The typical energy resolution of UPS is significantly higher than XPS making it better suited to investigation of the VB states.

With a good approximation, Eq. 2.6 gives the binding energy of the emitted electron. This allows the XPS technique to be used

²This derives from Koopmans’ theorem[20], which makes possible the identification of calculated orbital energies with ionization potentials but it does not take into account for electronic relaxation.

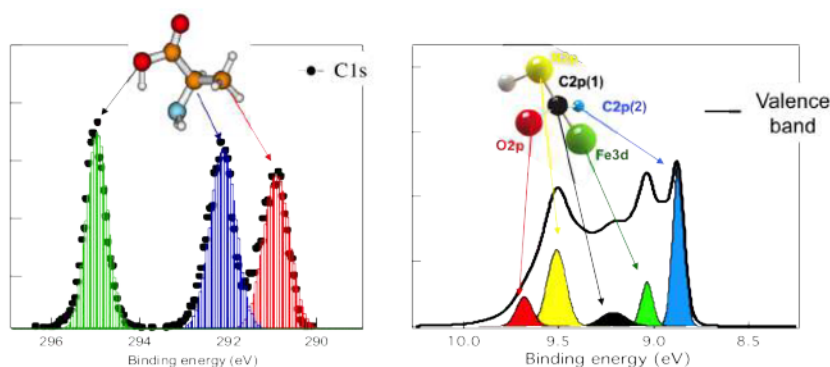


Figure 2.2: Illustration of the site assignment with core level (left) and with valence band (right) photoemission

as a probe to identify the chemical elements present in the sample by means of core levels analysis, in which case it is also called ESCA (Electron Spectroscopy for Chemical Analysis). Core levels - the atomic like levels that do not take part in chemical bonding - can provide informations about the chemical environments of each specific atomic site in a molecule. These deviations from a pure “atomic” binding energy are known as chemical shifts, and provide the XPS technique the ability to distinguish atoms of the same species in different molecular environments, and constitutes the property of atomic selectivity. This advantage is illustrated in Fig. 2.2 and has been used to pinpoint the different carbon sites in biphenylene and oligothiophenes molecules in sections 3.2.2 and 3.1 respectively.

The photoemission process of a core level leaves the system in an excited state, which can be energetically de-energized by two different processes. The first process is the fluorescence, in which the core vacancy is filled by an electron from a higher shell or the valence band. The energy released in this process is emitted in the form of a photon. This process must satisfy the dipole selection rule ($\Delta L = \pm 1$). The second process is the Auger process, in which an electron from a higher shell or the valence band fills the core vacancy but the excess energy is released to a second electron, which leaves the material. The Auger final state is therefore a two-hole final state. Both processes lead to a final state that is energetically more favorable than the final state of the PES. The Auger decay due to a hole in the C 1s level can be filled by an electron from the C 2s level and the energy can be transferred to an electron in the C 2s or C 2p level or be filled by an electron from the C 2p and the energy

transferred to a C $2p$ electron. The resulting three Auger decay channels are designated KL_1L_1 , $KL_1L_{2,3}$ and $KL_{2,3}L_{2,3}$.

After photoemission, there is also a finite probability that the atoms is left in an excited state. This results in the formation of a satellite peak a few electron volts higher in binding energy than the main peak. For example, in the carbon C $1s$ signal, molecules with a pronounced π character often lead to wider peaks with higher binding energies. These “shake-up” peaks are shifted up to 10 eV, and they occur when the photoelectron induces during its emission a ($\pi - \pi^*$) transition and thereby loses some of its energy. The displacement quantitatively corresponds to an optical HOMO-LUMO transition. More than one satellite of a principal photoelectron line can also be observed. The displacements and relative intensities of shake-up satellites can sometimes be useful in identifying the chemical state of an element, as discussed in Section 3.2.3.

In photoionization detection, an important parameter is the photoemission cross section σ_{ph} , that represents the number of electrons emitted in the unit of time and for each scattering center, divided by the number of incident photons in the unit of time and unit of area[22]. σ_{ph} can be calculated from the transition probability of Eq. 2.5 promoting an electron from a bounded state to a continuum state with a kinetic energy sufficiently high to be described by a plane wave. The photoionization cross sections can therefore be calculated and tabulated[23, 24].

The cross section σ_{ph} is a scalar that only quantifies the intrinsic rate of the photoemission event. In contrast, the differential cross section $d\sigma_{ph}/d\Omega$ is a function that quantifies the intrinsic rate at which the emitted electrons can be detected at a given angle and is even more important because it is the real quantity that we measure. For linearly polarized photons in the dipole approximation, the photoelectron angular distribution can be written as [25]

$$\frac{d\sigma_{ph}}{d\Omega} = \frac{\sigma_{ph}}{4\pi} \left[1 - \frac{\beta}{4}(3\cos^2\theta - 1) \right] \quad (2.7)$$

where β is the dipole asymmetry parameter and θ is the angle between the polarization vector and the electron emission direction. From Eq. 2.7 one can see that the detection is complicated further by the anisotropic nature of the photoemission event, resulting in an angular dependence of the number of photoelectrons emitted. Accounting for these asymmetry effects implicate that the geometry of the experiment needs to be considered. The best geometry that one can adopt is at a detection angle $\theta = 54.7$ deg, that cancels off the second term of Eq. 2.7 and makes the photoemission signal

independent of angular contributions.

2.0.3 X-ray Absorption Spectroscopy

While PES allows to perform a spectroscopic study of populated electronic levels in atoms, molecules and solids (core and valence states), XAS (X-ray Absorption Spectroscopy) is an experimental technique that offers the possibility to study the unoccupied electronic structure. In XAS a core electron is excited into an empty orbital $|f\rangle$ whose transition probability is given by Eq. 2.4 . Like for XPS, the strongly localized nature of the core hole makes the XAS spectroscopy very sensitive to the electronic structure and to the local environment of the absorbing atom even when it is embedded in a complex situation.

The absorption of radiation with energy $h\nu$ and intensity I_0 and the associated loss through matter can be described by the Lambert-Beer's law:

$$I(h\nu) = I_0 e^{-\mu(h\nu)d} \quad (2.8)$$

that takes into account the density of the sample material d and the absorption coefficient $\mu(h\nu)$. Generally, the absorption coefficient is inversely dependent on photon energy (i.e. photons with higher energies are more penetrating except at the absorption edges). The absorption cross section $\sigma(h\nu)$ reported Eq. 2.5 is proportional to $\mu(h\nu)$ according to the formula

$$\mu(h\nu) = \sigma(h\nu)lc \quad (2.9)$$

where l is the path length, and c is the concentration.

By scanning the energy $h\nu$ around the ionization threshold, a resonant transition occurs when the energy of X-ray photons matches exactly the energy difference between the initial orbital and the final orbital. These transitions are superimposed on the step-like shape corresponding to the onset of the ionization potential (see Fig. 2.3).

At these energies the material has a strong X-ray absorption referred to as atomic absorption edge. After this edge the absorption probability decreases monotonically. The atomic absorption edge depends on the electron binding energy (BE) which is the minimum energy required to ionize the specific electron. As the BE is related to atomic number (Z), each element absorbs X-rays at determined energies, resulting in an element-specific, orbital-projected technique. X-ray absorption edges are labeled after the initial core electron states. For example K , L_1 , L_2 , L_3 , etc. correspond to

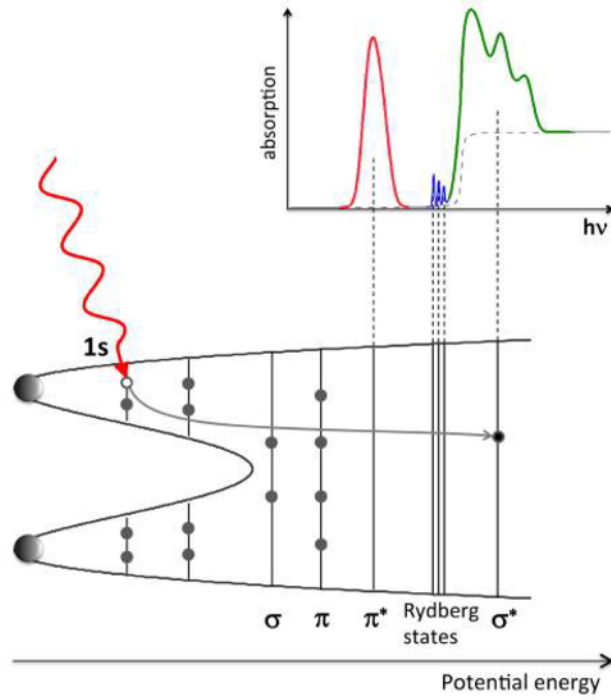


Figure 2.3: Bottom: schematic potential of a diatomic molecule. Top: the corresponding NEXAFS spectrum at the K edge ($1s$ core level) which includes Rydberg and unfilled molecular orbitals. unoccupied molecular orbitals are called σ^* or π^* , depending on their symmetry.

the creation of electron holes in the $1s$, $2s$, $2p_{1/2}$, $2p_{3/2}$ etc. atomic subshells (nl_j notation).

Basically, Eq. 2.4 can be re-written [26, 27] as:

$$\sigma(E) = \frac{4\pi^2\hbar^2 e^2}{m^2} \frac{1}{\hbar c \hbar\omega} \zeta(E) |\langle i | \hat{\epsilon} \cdot \mathbf{r} | f \rangle|^2 \delta(E_i - E_f + \hbar\omega) \quad (2.10)$$

where $\zeta(E)$ is the energy density of final state. The matrix elements $|\langle i | \hat{\epsilon} \cdot \mathbf{r} | f \rangle|$ in Eq. 2.10 is subject to the dipole selection rules according to which only transitions that change the angular momentum quantum number l by one, $\Delta l = \pm 1$, may occur in the XAS process. While the spin is conserved, $\Delta s = 0$, the orbital momentum of the z -component must change by zero or one, $\Delta m = \pm 1, 0$. In particular, $\Delta m = +1$ for left circular polarized light and $\Delta m = -1$ for right circular polarized light. In a molecular orbital (MO) description of the electronic structure, the initial state $|i\rangle$ is substantially represented by the atomic wave function of the excited atom, with a well defined l quantum number. The final state of a transition

to a bound state can be represented by a LCAO wave function of the corresponding final molecular orbital, provided that it is dipole allowed. Therefore, the fine structures around the K -edge are essentially formed by $s \rightarrow p$ dipole allowed transitions, while the L -edge structures are $p \rightarrow d$ dipole allowed transitions. The dipole matrix term is also the theoretical basis for the polarization-dependence of NEXAFS measurements, discussed in the next Section.

For the discussion of absorption transitions or intensities of resonances, instead of absorption cross-section, the optical oscillator strength f is used. f is a dimensionless quantity is related to the X-ray absorption cross-section by:

$$\sigma(E) = C \frac{df}{dE} \quad (2.11)$$

where $C = 2\pi^2 e^2 \hbar / mc = 1.1 \times 10^2$ Mb eV. f is the energy integral of the cross section and is a measure of the intensity of a resonance. The expression for “ f ” is:

$$f = \frac{2}{m\hbar\omega} |\langle i | \hat{\epsilon} \cdot \mathbf{r} | f \rangle|^2 \quad (2.12)$$

and can be converted to cross-section by using equation 2.12:

$$\sigma(E) = \frac{2\pi^2 e^2 \hbar}{mc} f \zeta(E) \quad (2.13)$$

2.0.4 Interpretation of NEXAFS

More in detail, NEXAFS spectroscopy refers to the energy region that extends between 30-50 eV after the absorption edge in X-ray absorption spectrum and probes the absorption of X-ray radiation for the excitation of core electrons into unoccupied molecular orbitals, Rydberg orbitals or the continuum. The region after 50 eV is referred to as Extended X-ray Absorption Fine Structure (EXAFS) spectroscopy and is usually used for studying samples in order to determine the number, distance, and type of the ligand groups attached to the absorbing atom, but it is not explored in this work. A schematic X-ray absorption edge is represented in Fig. 2.4.

NEXAFS at the C- K edge is particularly useful for the analysis of organic systems, offering the advantage - compared to the XPS - to characterize the unoccupied molecular orbitals depending on their character. For example, π^* orbitals are the lowest unoccupied

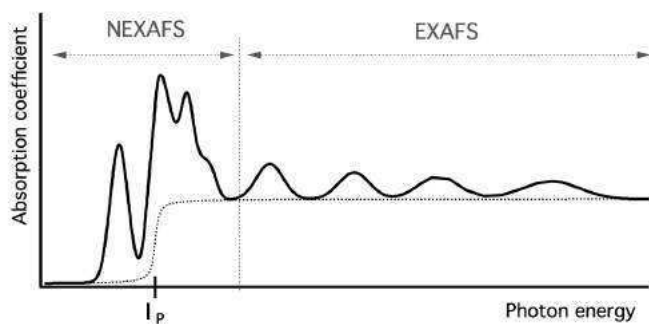


Figure 2.4: Schematic representation of an X-ray absorption edge. The absorption coefficient is displayed as a function of the excitation energy (photon energy). I_P is the ionization potential. The spectrum is divided into the NEXAFS and the EXAFS regions.

orbitals; their corresponding signal, also called " π^* resonances", are pulled below the ionization potential by electron hole Coulomb; on the contrary σ^* orbitals are found at higher energies, usually above the ionization potential. Between the π^* and σ^* resonances few eV below the ionization potential a further group of resonances represents the transitions to the Rydberg orbitals as sharp but weak peaks. In condensed phase or strongly chemisorbed molecules, Rydberg resonances are quenched by the delocalization of the orbitals [26].

Due to the strong directional character of the π^* and σ^* MOs, it is possible to determine the orientation of the molecule on a substrate by means of linearly polarized light using the so called "search light effect" [26]. In fact for oriented molecules and polarized X-rays the intensities of the π^* and σ^* NEXAFS features should exhibit a pronounced angular dependence, a technique that works especially well for molecules with planar symmetry, as shown in chapter 3.2.3. Fig. 2.5 displays an example of the technique for two polarization geometries: in-plane polarization (IPL) and out-of-plane polarization (OPL). The different geometries are realized rotating the sample with respect to the incoming beam. The σ^* transitions are polarized in the $x - y$ plane of the molecule and π^* transitions are polarized along z direction. By these facts, it is possible to measure a linear dichroism and to derive conclusions about the molecular orientation. When, for example, the molecules are lying parallel to the substrate π^* transitions have their maximum intensity at grazing incidence compared to normal incidence; for σ^* transitions we have the other way around. In a vertical orientation of the molecules, the

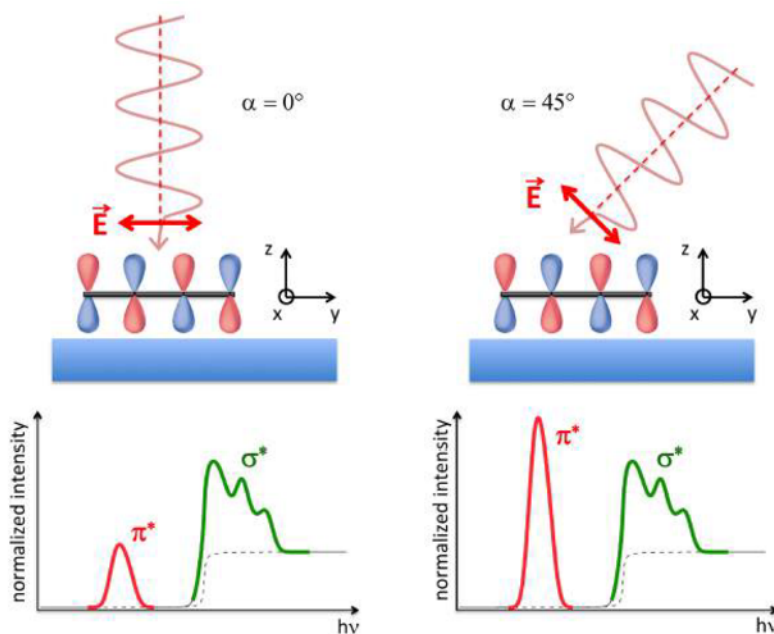


Figure 2.5: Schematic illustration of the “search light” effect in polarization dependent C K NEXAFS on a molecule lying flat on a surface (side view). α is the angle between the propagation of the light and the normal to the surface. Two geometries are represented: in-plane polarization (IPL, left) and out-of-plane polarization (OPL, right). At the bottom the corresponding NEXAFS spectra are represented. They are composed by a part having π^* character (red) and a part with σ^* character (green).

two transitions behave exactly opposite to the previous example.

2.0.5 Experiments vs theory

It is important to assist the interpretation of the experimental spectrum by means of theoretical calculations, in order to propose a rationalization and assignment of the experimental spectral features. With the advances in computer technology it is possible nowadays to simulate atoms, molecules and condensed matter with a reasonable use of computational resources. The quantum mechanical solution of the Schrödinger remains still a prohibitively complex task for multiparticle systems and therefore methods based on different types of approximations have been developed to solve it in terms of single-particle equations and an effective potential.

State-of-the-art electronic structure calculations such as using Density Functional Theory (DFT), developed by Hohenberg and Kohn [28], has been quite successful for the interpretation of the

experimental data[29].

The Density Functional Theory is nowadays one of the most used methods for calculating electronic structure of many body systems. To point out why this approach is so commonly applied and so powerful, some basic lines of the many body problem will be addressed. At the quantum mechanical level, to obtain information about a N particle system, one has to solve the Schrödinger Equation which describes the problem

$$H\Psi = E\Psi \quad (2.14)$$

The total wave function Ψ is a complicated function, as it depends upon both the coordinates of the electrons and the nuclei of the treated system. The nuclear motion problem can be treated separately if the motion of the electrons is much faster than nuclei motion, this approximation is the so called Born-Oppenheimer (B-O) approximation. At this level the problem is reduced to the determination of the electronic wavefunction at fixed nuclear positions.

In DFT the physical quantity involved in the theory is the electron density which depends only on the three spatial coordinates. DFT provides a variational principle which can be rigorously employed to describe the Ground State (GS) of electronic systems such as atoms, molecules and solids. Once the electron density is known, the external potential, and consequently the Hamiltonian of the system are in principle uniquely determined. The knowledge of Hamiltonian in its turn determines the total electronic wave function. Consequently, every quantum mechanical observable is a functional of the ground state density. For a system without external perturbations the cusps in the electronic density determine the positions of the nuclei, the gradients of the density at the nuclei their nuclear charges and the integrated density the total number of electrons in the system.

The first step in the construction of a practical DFT is to consider a fictitious system of non-interacting particles. Each particle in the system moves independently in an effective local potential. This non-realistic potential is called Kohn Sham (KS) Potential (V_{KS}). In the KS approach, the density of such system is required to be the same of the interacting particles in the real system. The V_{KS} consists of three parts:

1. An external potential V_{ext} which represents the Coulomb field generated by the nuclei and an external field (if present)

2. The Hartree potential from the Coulomb interaction with the electron density
3. The exchange-correlation potential V_{XC}

and therefore it can be written as follows:

$$V_{KS} = V_{ext}(\mathbf{r}) + \int \frac{\rho(\mathbf{r}')}{|\mathbf{r} - \mathbf{r}'|} d^3\mathbf{r}' + V_{XC}[\rho](\mathbf{r}) \quad (2.15)$$

The V_{XC} is a density functional and in principle it contains all the many-body exchange and correlation effects, due to the non-classical electro-electron interaction. The effective field V_{KS} defines the KS Hamiltonian and a correlation to the kinetic energy functional of the non-interacting system

$$H_{KS} = -\frac{1}{2}\nabla^2 + V_{KS} \quad (2.16)$$

and the KS equations are so defined:

$$H_{KS}\phi_i(\mathbf{r}) = \epsilon_i\phi_i(\mathbf{r}) \quad (2.17)$$

which consist of one-electron Schrödinger-type equations. Formally they include electron correlation, and their solutions (eigenvalues and eigenfunctions) are the KS energies and KS orbitals, respectively.

The KS potential depends upon the electron density $\rho(\mathbf{r})$. The electron density is exactly obtained by summing the squares of the KS orbitals and multiplying them by their occupation numbers n_i which leads to a function of \mathbf{r}

$$\rho(\mathbf{r}) = \sum n_i |\phi_i(\mathbf{r})|^2 \quad (2.18)$$

Since the KS potential $V_{KS}(r)$ and the density $\rho(\mathbf{r})$ are not independent, the equations have to be solved in an SCF³ scheme, meaning that the effective potential $V_{KS}(r)$ is calculated from the density, iteratively. The density of the previous cycle is used to calculate $V_{KS}(r)$ until convergence is reached. Convergence criteria are usually met when, for example, the difference in the energy or the density matrix between two subsequent SCF cycles goes below a fixed threshold. At the end, the molecular orbitals ϕ_i are obtained and the corresponding eigenvalues ϵ_i represent the orbital energies.

³The Self-Consistent Field (SCF) method is an iterative method: it selects an approximate Hamiltonian, solves the Schrödinger equation to obtain a better (i.e. more accurate) set of orbitals; the results are used to solve the Schrödinger equation again until the results converge.

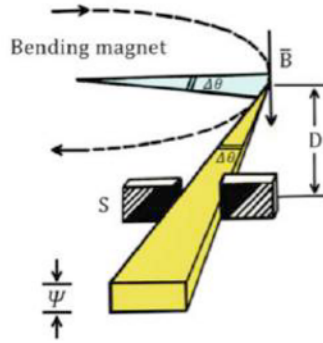


Figure 2.6: Synchrotron radiation emitted in a bending magnet at a distance D from the orbit. The magnetic field \mathbf{B} is perpendicular to the orbit (from Ref [30]).

2.1 Synchrotron based photoionization studies

2.1.1 Synchrotron radiation

A synchrotron radiation source consists of a storage ring where charged particles (usually electrons) are accelerated and forced on a well-defined orbit by means of an array of magnetic fields. When the charged particle is moving at relativistic speed (i.e. $v \approx c$), part of their kinetic energy is transformed into electromagnetic radiation known as synchrotron radiation and is emitted into a cone that is tangential to the orbit of the electrons (see Fig.2.6)

The opening angle Θ of the cone of emitted radiation is inversely proportional to the energy of the electrons E ,

$$\Theta = \frac{m_0 c^2}{E}. \quad (2.19)$$

Combined with the fact that the power of the emitted radiation by a single electron is proportional to the fourth power of the electron's energy,

$$P = \frac{2}{3} \frac{e^2 c}{R^2} \left(\frac{E}{m_0 c^2} \right)^4 \left(\frac{1}{4\pi\epsilon_0} \right) \quad (2.20)$$

it is obvious that the higher the electrons energy in a storage ring is, the more powerful and more collimated the emitted radiation will be. According to Eq. (2.20) the rest masses of the accelerated particles should be as small as possible to increase the radiation power, and therefore electrons are widely used in storage rings. The bending magnets installed in the arc sectors of the storage rings are the simplest radiation sources, with a continuous emission spectrum

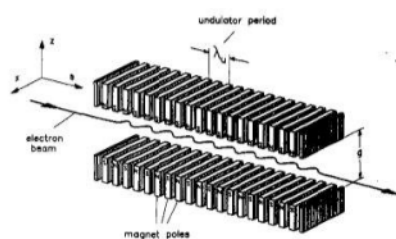


Figure 2.7: Radiation emission in an undulator (from Ref [31]).

that extends over a very broad energy range. However periodic magnetic arrays like undulators are insertion devices designed for very intense but not necessarily continuous emission.

The operation principle of an undulator is illustrated in Fig.2.7. The charged particles are forced into an oscillating motion across the axial direction that - usually - follows a sinusoidal trajectory. Depending on the parameters of the insertion device, constructive interference shapes the spectrum into a series of intense and narrow peaks. The synchrotron radiation is led to a beamline, whose main purpose is to monochromatize the radiation so that it could be used for experiments. The following section will give a more detailed description of the storage rings and the beamlines relevant to this thesis.

2.1.2 Beamline Gas Phase at ELETTRA

ELETTRA is a third generation synchrotron radiation facility operational since October 1993 in Trieste, Italy and provides light with photon energies in the range from 10 eV to 30 keV, and with a spectral brilliance up to 10^{19} photons/s/ mm²/mrad²/0.1%bw. Electrons are periodically injected in the storage ring in the top-up mode and are accelerated to 2-2.4 GeV.

The Gas Phase Photoemission beamline of ELETTRA is based on a 36- period undulator which produces high intensity synchrotron radiation in the energy range of 15 - 850 eV; reduced intensity is still available well above 850 eV.

The period of the magnetic array is 125 mm, yielding a total length of 4.5 m. In addition, the undulator is divided into three independently controlled parts of 12 periods, whose gaps can be varied separately. This enables a so- called 'tapered' mode of the undulator, in which the three gaps have slightly different widths, resulting in undulator peaks much wider than in the normal mode (all gaps have equal values).

The beamline has been designed primarily for studies of gases and vapors involving high resolution photoemission and coincidence detection. A variable angle spherical grating monochromator is used to disperse the light coming from the undulator. A toroidal mirror focuses the light vertically onto the entrance slit and horizontally onto the exit slit of the monochromator. Between the slits a plane mirror and spherical grating monochromatize the light. One of five gratings is selected according to the energy range required. The following two mirrors focus the beam both horizontally and vertically to the source region of the spectrometers. The resolving power has been measured in photoabsorption to be equal to or above 10 000 up to 500 eV photon energy and well above 7000 even at a photon energy of about 850 eV. The optical layout of the beamline is presented in Fig. 2.8. A detailed description of the beamline is presented in Refs. [32, 33]

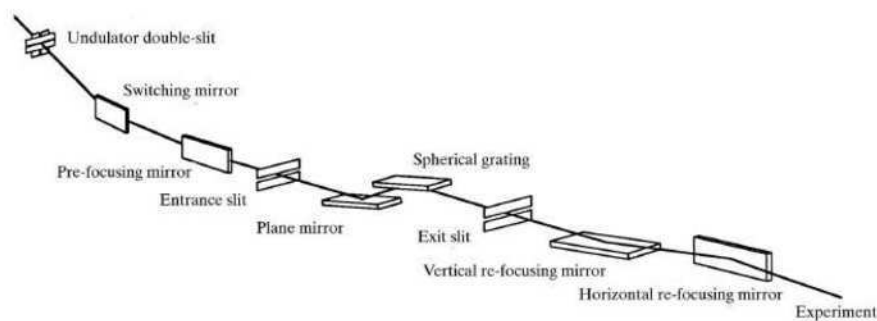


Figure 2.8: Schematic diagram of the optical layout of the gas-phase beamline.

The end station used for this work comes from a collaboration between CNR-IOM and the University of Uppsala, and is equipped with an hemispherical electron energy analyzer (Scienta SES-200) and facilities to detect total or partial electron and ion yield. The gaseous samples can be inserted through a gas inlet (gas or vapor form a liquid), or can be produced as a diffused beam from a heated oven.

2.1.3 Beamline I311 and D1011 at MAX-II

The third generation storage ring MAX-II (the name derives from the first accelerator of the lab: Microtron Accelerator for X-rays) in Lund, Sweden was one of the three storage rings in MAX-lab. MAX-II was operated at 1.5 GeV electron energy, and the ring was injected once a day using a 500 MeV linear accelerator and 500 MeV MAX-I ring. The MAX-II ring provided radiation from about 10 eV

to 20 keV. The brightness of the undulator sources was about 10^{18} photons/s/mm²/mrad²/0.1%bw i.e. about one order of magnitude lower than ELETTRA.

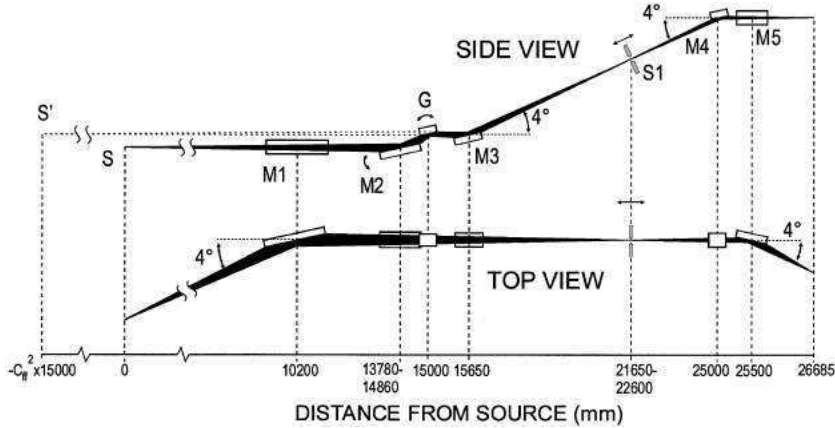


Figure 2.9: Optical layout of the I311 at MAX-II storage ring.

Beamline I311 was an undulator based soft X-ray beamline at the MAX II storage ring of MAX-lab. It was operational between 1999 and 2015. It provided linear polarized light, in the energy range 42.5 to 1500 eV (for the Spectroscopy endstation). The original design of the beamline, is described in Ref.[34], though the original magnetic lattice of the undulator described in the article was replaced in July 2010 with a new one that had 45 periods with length equal two 54.4 mm. The Layout of the beamline is described schematically in Fig.2.9. The light from the undulator is focused horizontally by means of a cylindrical pre-mirror (M1) toward the monochromator, a modified version of the SX-700 plane grating monochromator consisting of the original plane mirror (M2) - plane grating (G) combination plus a spherical focusing mirror (M3). The refocusing system consisted of two spherical mirrors mounted in a Kirkpatrick Baez arrangement. The vertically deflecting mirror (M4) focuses the exit slit onto the sample while the horizontally deflecting mirror (M5) images the focus of M1 onto the sample position. With a fixed radius of M4 the vertical focusing is optimal only for a specific exit slit position which was chosen to correspond to a c_{ff} (fixed-focus constant) value of 4.5 (moderate high resolution and suppression of the higher orders). The spot size on the sample at the spectroscopy station was then about 0.5 mm horizontally and 0.1 mm vertically. The first station was used for high resolution XPS and XAS. It consisted of separate analyzer and preparation chambers accessible via a long-travel manipulator. The preparation chamber included

the usual equipment for preparation and characterization of surfaces (ion sputtering gun, LEED optics etc.). A hemispherical electron energy analyzer (Scienta SES-200) was used for photoelectron spectroscopy.

D1011 was also a beamline dedicated to surface physics experiments. Photons were provided by a bending magnet and the monochromator was a version of the SX-700 design, with a 1220 l/mm grating and a plane-elliptical focusing mirror [35] modified to incorporate a premirror to collect a large horizontal angle of radiation..

2.2 Detectors and spectrometers

2.2.1 Total ion or electron yield

The measurement of the absorption coefficient through the direct application of the Lambert-Beer law (Eq. 2.8) is rather inconvenient in the soft-ray region. The most common way to produce a spectrum corresponding to an absorption measurement then is to collect the current caused by ions or electrons generated during the excitation and ionization processes. As mentioned above the photoabsorption process taking place when the incident photons hit the sample results in the creation of an excited state that can decay either radiatively by the emission of a fluorescent photon, or non-radiatively by the emission of an Auger electron (and consequently an ion). Both fluorescence and Auger channels are a direct result of the core hole created in the X-ray photoabsorption process and thus provide a basis to determine the absorption cross section. For low-Z elements (C, N, O) the Auger channel is much more efficient than the fluorescence one, making it better suited for low-Z molecules. With Total Ion Yield (TIY) or Total Electron Yield (TEY) one provides a field in the source region such that all the ions or electrons generated by the Auger decay are attracted to a detector of charged particles (usually a channeltron or multi channel plate detector).

The disadvantage of these detection techniques is that although the signal recorded will exhibit all resonances present in the X-ray absorption coefficient, it will typically not follow the X-ray absorption coefficient quantitatively. It can still be used for the identification of the spectral structures of NEXAFS[26]. In addition, electron detection provides the higher surface sensitivity and in the majority of studies published in the literature this so-called electron yield detection scheme has been employed. The reason for the higher surface sensitivity is the relatively low kinetic energy of the electrons and the corresponding mean free path in solid matter, which is typically less

than 1 nm for energies between 250eV and 600eV. The inelastic scattering process leads to an electron current consisting only of those electrons whose energy is sufficient to overcome the work function of the material. The resulting effective escape depth and, therefore, the information depth of electron yield, has been estimated to be of the order of 5 to 10 nm [26]. A further option is Auger electron yield (AEY) detection where only elastically scattered Auger electrons are recorded. For its “elastic” character, AEY surface sensitivity is comparable to PES and provides the best surface sensitivity of the different detection modes for NEXAFS, but requires an electron energy analyzer in order to detect the Auger peaks. This is the set up adopted during the measurements at beamline I311 at MAX-II for the experiments shown in section 3.2.3

The TIY mode is very efficient for gas phase measurements, where the yield of ion after Auger process is very high. The TIY measurements shown in this dissertation were recorded with a Microsphere Plate (MSP) detector. It consists of small glass beads (typically their diameter is between 20 and 100 nm) sintered to form a thin porous plate. The surface of the glass beads is covered with partially conductive material that serves also for the emission of secondary electrons. The two faces of the plate are coated with conductive electrodes. A voltage of several thousand volts between the two electrodes establishes an electric field with an average direction normal to the faces of the plate and enables secondary electron multiplication and passages between the glass beads (see Fig. 2.10).

For the gas phase measurements with samples requiring high temperatures of vaporization (i.e. some TM-phthalocyanines), the high flux of electrons generated by the surfaces of the Knudsen cell⁴ were interfering with the ion detection. In order to complete the experiments, an in-house built ion yield detector was designed to repel the thermally generated electrons with a grid. Fig. 2.11 shows the design for such partial ion yield (PIY) detector; it is assembled using two high transmission metal grids for retardation and a channeltron assembly for electron multiplication. The first grid is operated at retardation voltage $-V_R$ and the second grid is usually grounded. Most electrons cannot pass through these two grids, while positive ions are accelerated towards the channeltron. The ion signal is amplified by the application of a voltage ($V_{ch} \approx -4000$ eV) on the channeltron and the current is collected by a current to voltage amplifier

⁴An effusion cell developed by Martin Knudsen (1871-1949), designed to deliver molecular beams with highly constant evaporation rates by indirect resistive heating.

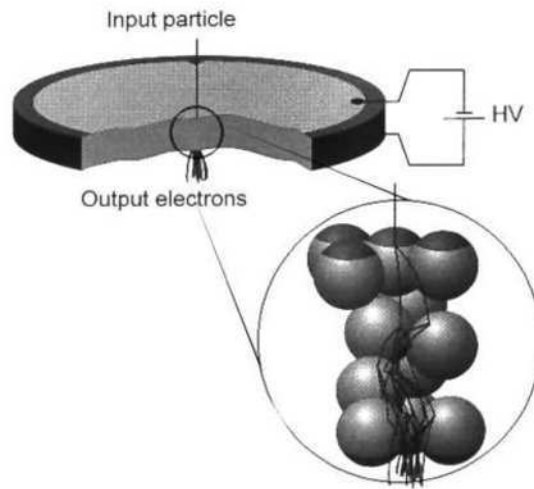


Figure 2.10: Schematics of an MSP design and of the multiplication chain (from [36]).

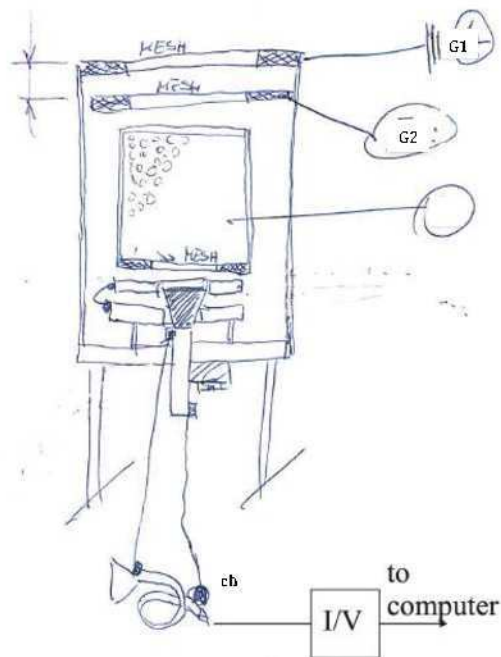


Figure 2.11: Schematics of the PEY detector with corresponding electronics. G1 and G2 are the two grids, ch is the channeltron, I/V the current converter; $-V_R$ the retarding voltage, V_{ch} the voltage on the channeltron.

2.2.2 Electron energy analyzer

The aim of an electron spectrometer is to analyze kinetic energy of the electrons in an electron cloud. The working principle to separate their energy is based on the use of either electric or magnetic fields according to the deflection applied by the Lorentz force

$$\mathbf{F} = q \cdot \mathbf{E} + q \cdot (\mathbf{v} \times \mathbf{B}) \quad (2.21)$$

where \mathbf{E} and \mathbf{B} are the electric and the magnetic field, respectively. In this way electrons can be separated spatially and their number recorded as a function of their kinetic energy. Most of electron energy analyzers use electrostatic fields to deflect electron trajectories. By varying the field it is possible to create conditions so that only the electrons with desired incoming angle $\theta \pm \delta\theta$ and kinetic energy $E_K = E_p \pm \Delta E$ will pass through the deflecting field and hit the detector. The goal of energy analysis is to combine high energy resolving power E_K/E_p with a high collection, though nature will oppose that. The latter can be achieved by using proper electrostatic lenses that can focus the electrons in the analyzer with the largest collection angle; the former is dependent on parameters of the analyzer that are fixed, like its dimensions and design and directly proportional to the kinetic energy. For this reason it is desirable to retard the electrons before they are deflected so that E_p is constant. This operation can be done using an additional lens and provides a constant resolution. E_p is the ‘pass energy’. The energy resolution for an hemispherical analyzer is given by equation

$$\Delta E = \frac{E_p S}{2R} \quad (2.22)$$

where S is the entrance slit and R is the mean radius of the analyzer.

The photoelectron spectra shown here were recorded using SES-200 hemispherical analyzers (mean radius $R = 200 \text{ mm}$) by Scienta [37, 38]. The electron detection is based on a combination of a multichannel plate and a fluorescent screen, where the intensity is recorded indirectly by monitoring the fluorescence using a CCD camera. The efficiency of this multichannel detection system can be further increased by using a gas cell that increases remarkably the sample density in the interaction region. SES-200 analyzer is shown in Fig. 2.12; both Gas Phase beamline at ELETTRA and the surface science end stations of beamlines I311 and D1011 at MAX-II were provided with analyzers of this class.

This type of analyzer represented a break in the 90s in the field of high resolution photoemission [39]. The electron-optical system

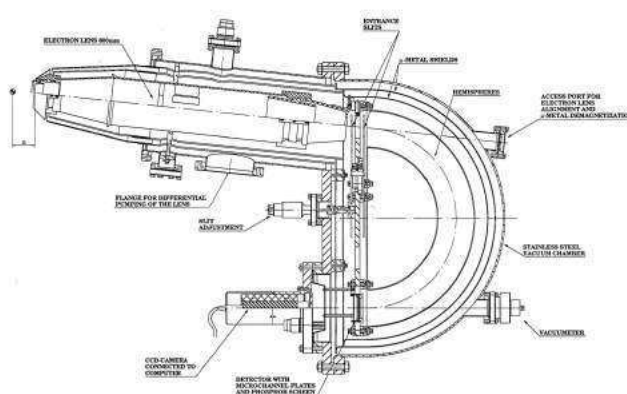


Figure 2.12: Hemispherical SES-200 electron energy analyzer

consists of a classic hemispherical analyzer with Herzog-plate termination and an electrostatic focusing lens system. It is a development and a reduced version of the older Scienta ESCA-300 instrument[40], with a main radius of the hemispheres of 200 mm. The acquisition software and power supplies were also changed, in order to achieve a better control of the focusing system with the electrostatic lenses. It is possible to choose either an imaging mode, where the magnification can be optimized with regard to the size of the excitation area, or an angle resolving mode, where electrons emitted in different directions are refocused to different points on the detector. The high performance of such spectrometers is related to the high efficiency of the photoelectron detection, that makes use of a two dimensional detector MCP- CCD (charge-coupled device) that allows a simultaneous measurement of photoelectrons with different kinetic energies and angle or coming from different spatial points in the interaction region (either the vapor beam or the sample surface). SES-200 detector can also be run in two modes: Pulse Counting mode, in which individual pulses are counted, and the analog to digital converter mode (ADC) in which integrated CCD charge is recorded. The lens voltages are continuously varied during the recording of a spectrum. The voltages are defined by a set of tables, which for each pass energy give the correct voltages for a discrete number of calibration kinetic energies. The appropriate voltages are then calculated by a cubic spline interpolation of the calibration energies. The first lens acts also as a deflection stage, which is extremely useful because it can be used to correct misalignments in the experimental set up. Typically such misalignments at a synchrotron occur from an experiment to the following one due to tiny changes in the position of

the end station or even during a single experiment due to problems connected with the running of the storage ring.

2.2.3 ULLA, and end station for high resolution measurements at GasPhase

For the high-resolution spectra at the Gas Phase beamline at Elettra, another SES-200 was upgraded to allow photoemission studies of vapors. The SES-200 used is the first prototype built at the Department of Physics in Uppsala described in [38] and had been originally dedicated to surface science research. The analyzer was mounted on its original UHV chamber - also manufactured by Scienta - and positioned at the beamline on a support that allowed the detection of photoelectrons in the dipole plane at the magic angle (see Eq. 2.7) with respect to the electric vector of the incident light. In order to bring the samples to the interaction region, the chamber was provided with a sample stage with a needle for the introduction of gases in vacuum and also with an in-house built Knudsen effusion cell for the vaporization of solid samples *in situ*. The position of the sample stage could be adjusted with the use of an xyz-manipulator, and made the end station very flexible for the study of gaseous, liquid and solid samples. Some measurements could also be done with diffused gases, whereby a sample gas was let in the chamber via a leak valve, without a needle and far away from the interaction region (commonly for calibration purposes). The resulting end station ULLA (ULtrafast Laser Assisted photoemission) was used for testing the performances of CITIUS laboratory (section 5.1.3) and then used at Gas Phase as a permanent facility. The assembled chamber is shown in Fig. 2.13.

Tests of resolution and intensity

The Scienta SES-200 analyzer can be operated with the preselected pass energies and the analyzer slits listed in Table 2.2 together with the theoretical resolution. Since the real resolution and transmission depend strongly on the position and shape of the light source, we have performed a complete set of test measurements on the analyzer real performances. The resolution tests were made with the Ar $3p$ and $2p$ photoelectron lines, whose linewidth are well known[41, 42]. The $3p$ line, which has an IP of 15.760 eV and the spin orbit splitting of 0.1775 eV[41], was used at the photon energies of 25.5 and 140 eV. At the lower photon energy, the pass energies 5-50 eV were tested. Fig. 2.15 shows the Ar $2p$ photo-



Figure 2.13: The assembled end station ULLA.

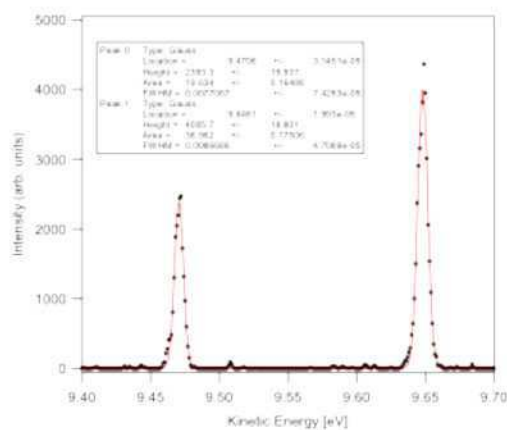


Figure 2.14: The Ar $3p$ photoelectron spectrum (dots) measured at the photon energy of 25.5 eV. The pass energy of 5 eV and analyzer slit of 0.3 mm were used. The red solid curve displays the fit of two Gaussian lines whose parameters are given in the insert. The measuring time was 1 sweep/5 frames ($=0.071$ s at each energy point). The small ripple is mostly due to the readout noise of the CCD camera.

Table 2.2: SES-200 slit dimensions and pass energies available. For the slits, the shape, dimension and width in mm are reported. The expected resolutions calculated with Eq. 2.22 are listed in italic, in meV. At the bottom, the available Kinetic Energies for each PE are reported, in the High Pass (HP) and Low Pass (LP) detection mode.

Slits			Available Pass Energies [eV]								
shape	length	width	1	2	5	10	20	50	100	200	500
curved	25 [mm]	0.2 [mm]	<i>0.5</i>	<i>1.00</i>	<i>2.5</i>	<i>5</i>	<i>10</i>	<i>25</i>	<i>50</i>	<i>100</i>	<i>250</i>
curved	25 [mm]	0.3 [mm]	<i>0.75</i>	<i>1.50</i>	<i>3.75</i>	<i>7.5</i>	<i>15</i>	<i>37.5</i>	<i>75</i>	<i>150</i>	<i>375</i>
curved	25 [mm]	0.5 [mm]	<i>1.25</i>	<i>2.50</i>	<i>6.25</i>	<i>12.5</i>	<i>25</i>	<i>62.5</i>	<i>125</i>	<i>250</i>	<i>625</i>
curved	25 [mm]	0.8 [mm]	<i>2.00</i>	<i>4.00</i>	<i>10.00</i>	<i>20</i>	<i>40</i>	<i>100</i>	<i>200</i>	<i>400</i>	<i>1000</i>
curved	25 [mm]	1.0 [mm]	<i>2.5</i>	<i>5.00</i>	<i>12.50</i>	<i>25</i>	<i>50</i>	<i>125</i>	<i>250</i>	<i>500</i>	<i>1250</i>
curved	25 [mm]	1.5 [mm]	<i>3.75</i>	<i>7.50</i>	<i>18.75</i>	<i>37.5</i>	<i>75</i>	<i>187</i>	<i>375</i>	<i>750</i>	<i>1875</i>
straight	30 [mm]	1.9 [mm]	<i>4.75</i>	<i>9.50</i>	<i>23.75</i>	<i>47.5</i>	<i>95</i>	<i>237</i>	<i>475</i>	<i>950</i>	<i>2375</i>
straight	30 [mm]	2.5 [mm]	<i>6.25</i>	<i>12.50</i>	<i>31.25</i>	<i>62.5</i>	<i>125</i>	<i>312</i>	<i>625</i>	<i>1250</i>	<i>3125</i>
straight	30 [mm]	4.0 [mm]	<i>10</i>	<i>20.00</i>	<i>50.00</i>	<i>100</i>	<i>200</i>	<i>500</i>	<i>1000</i>	<i>2000</i>	<i>5000</i>
			0-76	0-104	1-107	1-112	3-121	7-150	15-197	77-291	400-614 (LP)
			0-76	0-152	1-381	1-761	3-1522	7-1550	15-1597	86-1691	400-2000 (HP)

Table 2.3: The kinetic energy resolutions in meV extracted with Eq. 2.23. They were tested at different pass energies and analyzer slit widths. Empty cells indicate combinations where the Ar $3p$ spin-orbit splitting was no longer resolved. The photon energy used in the experiment was 25.5 eV.

Slit (mm)	tested Pass Energies [eV]			
	5 eV	10 eV	20 eV	50 eV
0.3	5.75	7.35	15.8	62.1
0.5	6.96	9.00	16.8	60.0
0.8	7.16	10.7	20.9	64.0
1.0	7.87	15.2	32.4	90.7
1.5	11.4	21.0	39.7	114
1.9	18.0	36.1	80.3	
2.5	25.7	57.6	113	
4.0	34.4	70.7		

electron line taken with 5-eV pass energy and 0.3-mm analyzer slit, which gave the narrowest observed peaks. The fit results obtained with Gaussian fit using the Igor program are included in the figure. The FWHM of the Ar $3p_{3/2}$ line, 8.67 meV, deviates slightly from the FWHM of 8.55 meV given by the Scienta measuring program during the measurement. The small asymmetry on the bottom-left flanks of the peaks may have been caused by charging of the needle, which was clearly observed in other measurements.

The widths and areas of the photoelectron lines given by the acquisition program are used in the following analysis. The analyzer resolution, Γ_A , was calculated from the measured FWHM values $= \Gamma_T$ using the equation

$$\Gamma_T^2 = \Gamma_A^2 + \Gamma_M^2 + \Gamma_D^2 \quad (2.23)$$

where Γ_M is the photon band width and Γ_D is the Doppler broadening.

With the chosen monochromator slit of 10/10 μm we got $\Gamma_M=1.6$ meV at the photon energy of 25.5 eV. Γ_D was calculated to be 6.125 meV for the Ar $3p_{3/2}$ photoelectron line, see e.g. [43]. The results for the kinetic energy resolution and photoelectron intensity are reported in Tables 1 and 2 as well as in the graphical form in Fig. 2.

The pass energies of 100 and 200 eV, that are more suited for core level spectroscopy, were tested by measuring the Ar $2p$ photoelectron spectrum (BE= 248.4 and 250.6 eV) at the photon energy of 400 eV. The spectra were also taken with 50 eV pass energy for comparison. The photon energy resolution with 30/30 μm slits is estimated to be 60 meV (see [44]), whereas the Doppler broadening is about 24 meV. Since the Ar $2p$ states have a significant lifetime broadening

Table 2.4: The intensity (area) of the Ar $3p_{3/2}$ photoelectron line at different pass energies and analyzer slit widths. The peak intensity given by the Scienta measuring program was multiplied by the step size. Empty cells indicate combinations where the Ar $3p$ spin-orbit splitting was no longer resolved. The photon energy used in the experiment was 25.5 eV.

Slit (mm)	tested Pass Energies [eV]			
	5 eV	10 eV	20 eV	50 eV
0.3	63.5	157.8	302.4	673
0.5	107	247	520.8	1011
0.8	182.3	436.8	868	1757
1.0	310.2	791	1486.4	2842
1.5	430.6	1074	1992.8	3678
1.9	743.5	1913.8	3495.2	
2.5	1110.9	2704	4884	
4.0	1376	3238		

$\Gamma_L = 118 \pm 4$ meV[43], in order to extract the analyzer contribution the following approximation⁵ was used

$$\Gamma_T^n = \Gamma_G^n + \Gamma_L^n \quad (2.24)$$

where the exponent $n(1 < n < 2)$ depends on the ratio Γ_L/Γ_T . The obtained kinetic energy resolutions and normalized intensities are given in Fig. 2.16.

The results of Fig. 2.16 are useful to deduce the order of magnitude and relative behavior. We note, for instance, that the kinetic energy resolution with $E_p=50$ eV and small slit sizes are about twice bigger in Fig. 3 than in Fig. 2, the results of which are more accurate. The accuracy of the analyzer resolution values given in Fig. 2.16 improves, when the lifetime broadening is not the predominant factor in the observed total linewidths.

The O $1s$ photoelectron spectrum of CO₂

In order to test the SES-200 analyzer in core photoelectron spectroscopy, the O $1s$ photoelectron line was measured at the photon energy of 628 eV. The beamline slits were set at 20/20 μm , resulting in the photon energy resolution of approximately 120 meV[44]. The results in two different counting modes, ADC and pulse counting, are shown in Fig. 2.17. The pass energy of 20 eV and the analyzer slit of 1.5 mm were used in the electron analyzer, which according to Table 2.3 corresponds to about 40 meV kinetic energy resolution. Vibrational resolution was achieved, which is not too difficult in this case because the vibrational structure is dominated by the large energy (~ 0.3 eV) of the asymmetric stretching mode. It appears from

⁵Dr. Antti Kivimäki, private communication.

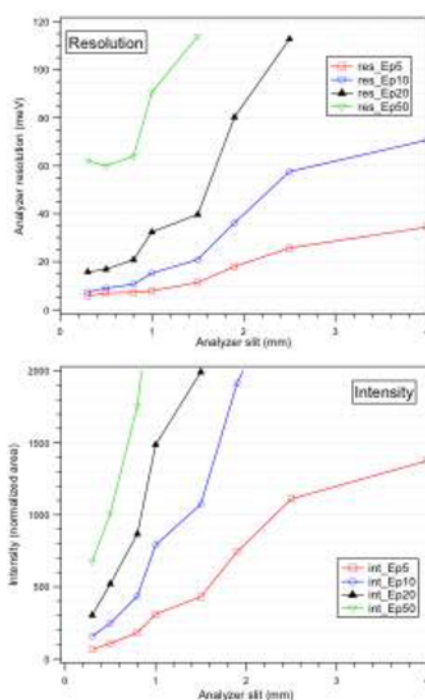


Figure 2.15: Kinetic energy resolution (upper panel) and the relative collection efficiency (lower panel) of the SES-200 analyzer at different pass energies and analyzer slit widths. The data are from the Ar 3p photoelectron spectra were measured at the photon energy of 25.5 eV.

these spectra that it does not matter which measuring mode is used at this count rate. The order of magnitude of the counts in the ADC mode is, however, inflated. Fig. 2.17 is useful for an approximate conversion factor between the two modes.

The same spectrum measured with diffused gas at the pressure of 7.2×10^{-6} mbar is shown in Fig. 2.18. The measuring time of the spectrum was the same as for the spectra of Fig. 2.17, but a higher pass energy (50 eV) and a larger slit size of the monochromator (30/50 μm slits) were used. The pressure, in contrast, was slightly lower. The measuring conditions were thus very different in the two measurements, but an order of magnitude estimate gives that the use of the needle increased the photoelectron intensity (taken as the area of the peak) by a factor of 25 as compared to the diffused gas. The needle in the measurement of the spectrum of Fig. 2.17 was just above the photon beam, so that low-energy electrons, which originated when the beam hits the needle, were no longer observed.

The F 1s shake-up spectrum of the C_6F_6 molecule

As an example of still more difficult measurements, we recorded

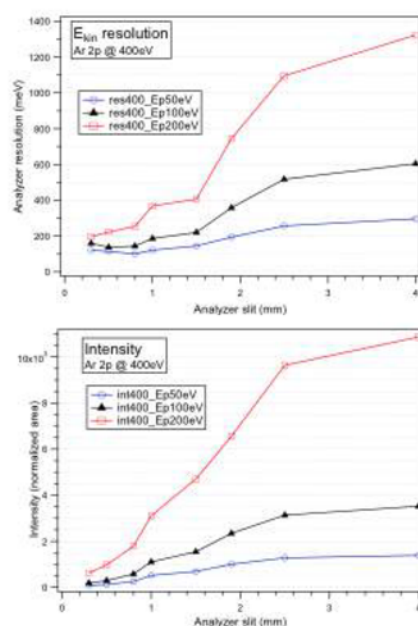


Figure 2.16: Kinetic energy resolution (upper panel) and the relative collection efficiency (lower panel) of the SES-200 analyzer for the pass energies 50, 100 and 200 eV with different analyzer slit widths. The data were extracted from the Ar $2p$ photoelectron spectra measured at the photon energy of 400 eV.

the F $1s$ shake-up spectrum of the hexafluorobenzene molecule (C_6F_6) at the photon energy of 783 eV. Due to the low intensity, the pass energy was increased to 100 eV and the beamline slits were set 50/50 μm , which corresponds to 0.5 eV photon resolution. The spectrum of Fig. 2.19 was collected for a total measuring time of almost 2 hours. Weak shake-up structures, for instance at 74 and 78 eV kinetic energy, barely rise up from the noise. The FWHM value of the F $1s$ main line in Fig. 2.19 is about 1.1 eV. This proves the high transmission of the apparatus.

Transmission of the SES-200 analyzer: the $N_{4,5}OO$ Auger spectrum of xenon

The measurement of the $N_{4,5}OO$ Auger spectrum of xenon provides with a quick method to check approximately the transmission of the electron analyzer in the kinetic energy range of 8-35 eV, because the transmission corrected Auger spectra have been published in the literature[45]. We performed the measurement at the photon energy of 130 eV using the pass energies of 10 and 20 eV. The measurement with $E_p=20$ eV is shown in Fig. 2.20 in comparison with the transmission corrected spectrum from Ref. [45]. The intensity ratios of the Auger peaks in the two spectra are similar, which indi-

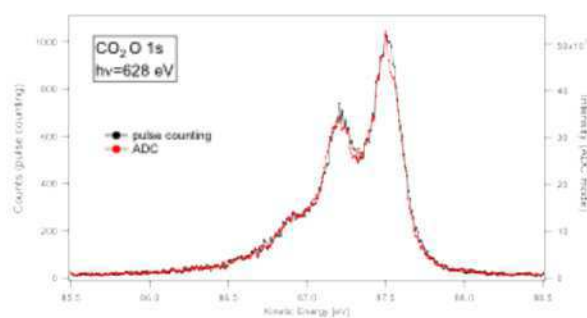


Figure 2.17: The O 1s photoelectron spectrum of the CO_2 molecule measured with 20 eV pass energy and 1.5 mm slit of the analyzer. The gas was inserted *in vacuum* with a needle. The two spectra were collected in different counting modes (pulse counting and ADC) during identical times.

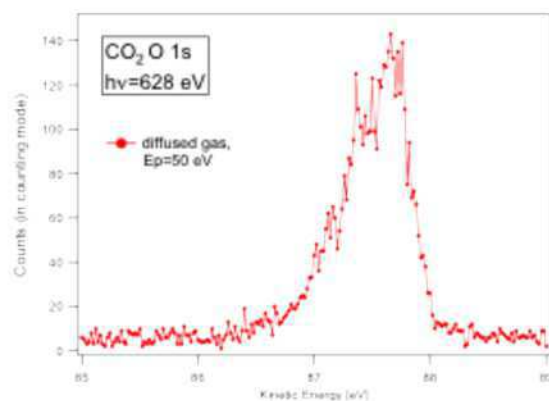


Figure 2.18: The O 1s photoelectron spectrum of the CO_2 molecule measured from the diffused gas with 50-eV pass energy and 1.5-mm slit of the analyzer.

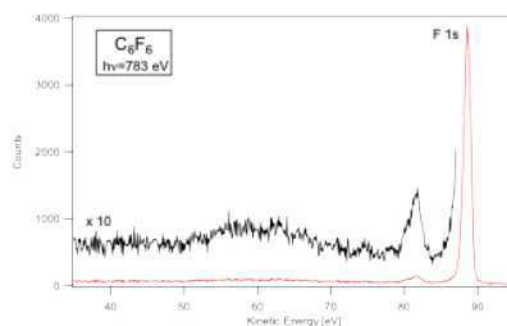


Figure 2.19: The F 1s shake-up spectrum of the C_6F_6 molecule measured in the pulse counting mode at the 783 eV photon energy, i.e. almost 90 eV above the F 1s ionization energy of 694.2 eV. The black curve shows the shake-up part of the spectrum magnified by the factor of 10.

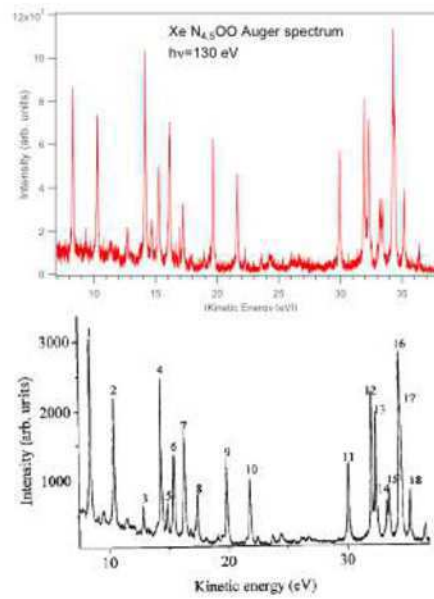


Figure 2.20: The upper panel shows the $N_{4,5}OO$ Auger spectrum of xenon measured in this work with 20 eV pass energy and 130 eV photon energy. The lower panel shows the transmission-corrected Auger spectrum that was taken at 133 eV photon energy[45].

cates that the transmission of the SES-200 analyzer is fairly flat in this kinetic energy range.

Chapter 3

Electronic structure of organic molecules

We are still a long way from realizing the vision of a bottom-up nanotechnology exploiting the surface-confined self-assembly of functionalized molecular building blocks and their interaction with appropriate surfaces as sketched in chapter 1. However, researchers are busily laying the basis for forthcoming nanoscale engineering: for example with the development of optoelectronic devices based on semiconducting π -conjugated materials, as alternative to inorganic semiconductors, for advantages that include low cost manufacture, simple processing, mechanical flexibility.

Detailed investigations are reported in this chapter, by means of core and valence photoionization spectroscopy supported by Density Functional Theory (DFT) calculations. The adopted approach is similar to the “bottom-up” strategy, starting from the study of the simpler molecular building blocks as model systems and increasing complexity to larger molecular systems and deposited films.

In Section 3.1 a systematic study of oligothiophenes in the gas phase was performed as a function of the chain length, where the comparison of experimental and calculated spectra provides a complete description of the main experimental features and allows their attribution. The evolution of the spectral features as a function of the number of thiophene rings confirms a tendency to a stabilization for increasing chain length.

In Section 3.2.2 detailed insights in biphenylene molecule were collected and the characters of the non-equivalent carbons were separated in gas phase core hole spectra. The growth on a metallic substrate [Cu(111)] was also studied.

In the study of pyridines and fluorinated derivatives shown in Section 3.3 the contributions of molecular vibrations has been added

in the analysis and simulation of the experiments.

3.1 Oligothiophenes

3.1.1 Introduction

The thiophene-based oligomers (shown in Fig. 3.1) consist of covalently linked thiophene rings (which has the formula C_4H_4S) connected via the ‘ α -carbon’ atoms, adjacent to the sulphur atom. The high polarizability of the S atom in the rings stabilizes the conjugated chain conferring excellent charge transport properties which are of fundamental importance for applications in organic and molecular electronics[46, 47].

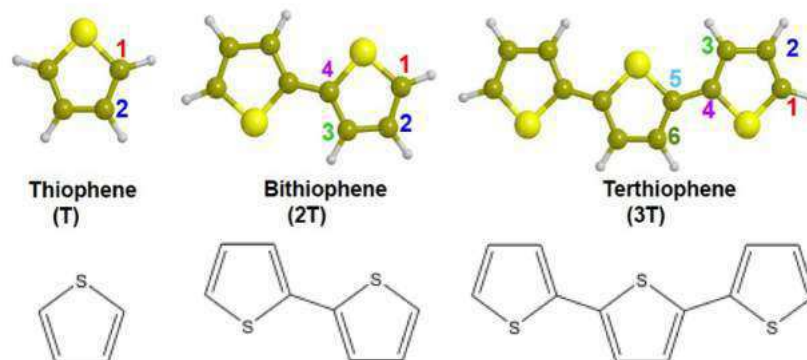


Figure 3.1: Upper panel: schematic illustration of thiophene (T), bithiophene (2T) and terthiophene (3T). The nonequivalent carbon atoms are labeled. Lower panel: Structures with the evidence of the double bonds. The molecular plane corresponds to the xy-plane.

Several works (see for example Ref. [7] and [8]) pointed out that in films of short chain thiophenes the chain length and morphology strongly influence the side chain packing and interdigitation; thus they can influence the supramolecular arrangement leading to high performance devices or, on the contrary, to small domains and poor performances. In spite of this findings, that are extremely important for the application of polythiophene derivatives in organic and molecular electronics, a systematic study of the electronic structure and charge dynamics in short chain thiophenes - starting from the most simple building blocks and increasing the complexity by adding more and more components - was still missing.

In this section, we report our investigation of the electronic properties of thiophene, 2,2'-bithiophene and 2,2':5',2''-terthiophene (re-

spectively, 1T, 2T and 3T) (Fig. 3.1) that are among the simplest building blocks of this class of compounds. They were studied as isolated molecule in the gas phase by core level photoemission and absorption spectroscopies. Since these techniques are sensitive to the local core hole on each specific atomic site, they appear very appealing to study the effect of the increasing complexity of our systems. The XPS and NEXAFS experimental results collected at the Gas Phase beamline of Elettra have been interpreted with the support of Density Functional Theory (DFT) calculations performed in the group of Prof. G. Fronzoni at the Department of Chemical and Pharmaceutical Sciences at the University of Trieste. The Transition Potential approach of the DFT (see Sec. 2.0.5) was used to deconvolve the spectral features into contribution of each atomic site and to interpret it in terms of their orbital character.

The commercially available Sigma-Aldrich high purity samples (with purities higher than 97%) have been used for the analysis. 1T and 2T are liquid at room temperature. They were inserted in vacuum after several freeze-pump-thaw cycles of purification and dosed via a stainless steel variable leak valve. 3T sample is solid at room temperature. It was sublimated in vacuum using a custom built resistively heated furnace set at $T=66^\circ$ after a purification treatment at 30 degrees for 12 hours. Preliminary PES of the valence region recorded at low photon energies confirmed the purity of the vaporized samples (see Section 3.2). Measurements were performed at the Gas Phase beamline of Elettra, using the SES200 electron analyzer introduced in Section 2.2.2 and the ion detector of Section 2.2.

3.1.2 Photoemission

Photoemission at the C1s core levels was recorded at a photon energy of 332 eV with an overall resolution of 150 meV. The peak positions were calibrated with respect to the C1s binding energy of CO₂ (297.6 eV [48]). The spectra are shown in Fig. 3.3 together with an analysis of the experimental line shapes by fitting procedures. The C1s peaks were fitted using an in-house written procedure running for IGOR PROTM analysis program that was inspired by the work of Giertz et al. (see Ref. [49]). In the cited work, the C1s photoemission spectrum of thiophene was found to be affected by a pronounced vibrational envelope and was analyzed by means of the theoretically calculated vibrational profile. In this work reproduce that, we have fitted each spectral feature using a main peak followed by a progression of smaller peaks at higher binding energies (dashed lines in Fig. 3.3). In this way we have built a function that

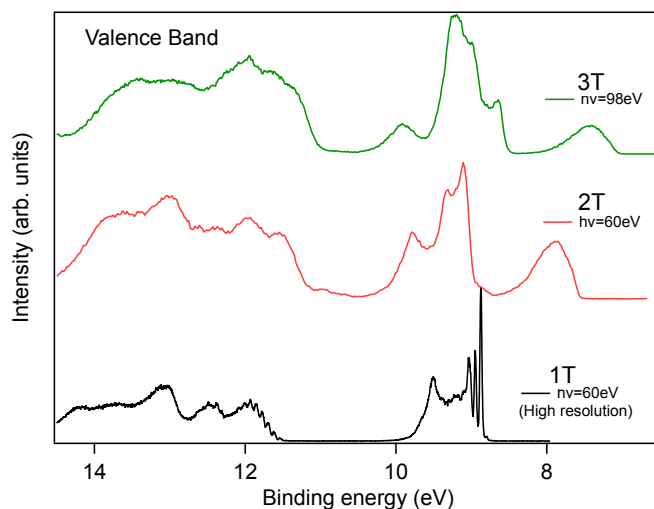


Figure 3.2: Valence band spectra of 1T, 2T and 3T after sample purification. The overall resolution for 2T and 3T was 170 meV, while 1T was recorded with higher resolution (25meV).

accounts for an adiabatic peak accompanied by a vibrational "tail", and the function has been repeated for each different carbon sites C_i (thin solid lines in Fig. 3.3). The line shape for all C_i 's of one molecule was kept fixed, i.e. the widths of all sub-peaks were the same and their relative intensities were also fixed. This choice, that is reasonable for 1T but can be considered arbitrary for the larger molecules, turns out to work quite well as shown in Fig. 3.3.

One should also consider that the overall energy resolution during the measurements was almost twice as the resolution of Giertz et al. [49], therefore a detailed vibrational analysis by fitting methods is not possible. Moreover, this approach allows better to study the evolution of the line shape when the size of the molecule increases. Remarkably, while the vibrational tail is very intense for 1T, it decreases remarkably for 2T and is very low for 3T, though it is still necessary to perform an acceptable fitting. The intensity of the vibrational tails is about 40% for 1T, 27% for 2T and only 8% for 3T.

For a more detailed analysis of the spectral shapes we compare them to the calculated Δ KS binding energies BE, which are displayed as vertical bars. In Table 3.1 they are listed together with the results of the fit. It would be too difficult to calculate the absolute intensity of the XPS lines since the unbound photoelectron wave function should be employed in the dipole transition moment. Therefore we simply assumed that the intensity of each $C1s$ line

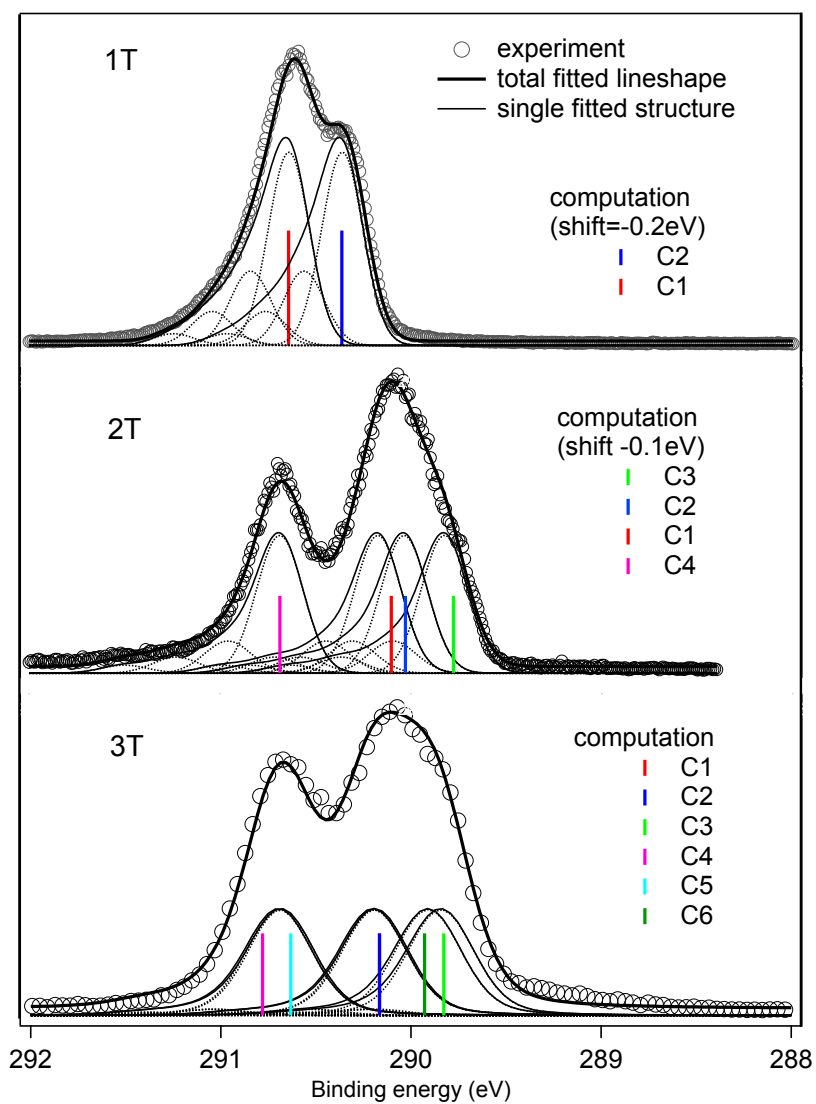


Figure 3.3: C 1s XPS spectra of 1T, 2T and 3T: experimental data (circles) are shown together with the results of the peak fitting procedure described in the text. The solid thick lines are the total fitted line shape, while the thin black solid lines are the line shapes for each carbon site, which are decomposed in a series of Voigt functions. The vertical colored lines are the BE calculated at the Δ KS level (Sec. 2.0.5); the line intensity is proportional to the multiplicity of the carbon atoms and the energy scale for thiophene and bithiophene has been shifted respectively by -0.2 and -0.1 eV.

Table 3.1: Calculated BE with corresponding carbon site (second column). Experimental BE extracted with the fitting procedure described in the text (last column).

	BE (eV)	
	computed	EXP (fit)
Thiophene		
C1	290.662	290.60
C2	290.383	290.35
Bithiophene		
C1	290.787	290.70
C2	290.204	290.19
C3	290.130	290.07
C4	289.878	289.89
Terthiophene		
C1	290.781	290.697
C2	290.633	290.685
C3	290.167	290.20
C4	290.166	290.19
C5	290.929	290.91
C6	290.828	290.85

is proportional to the number of equivalent carbon atoms (in each molecule of the series all the carbon atoms have the same site multiplicity of 2). Note that the calculated energies of thiophene and bithiophene are shifted in energy (-0.2eV and -0.1eV respectively) to facilitate the comparison. Following the calculated BE, it is possible to define two different groups of carbon atoms: the first one at lower binding energies corresponds to the carbon atoms not bonded to a sulfur atom, while the second group at higher energies identifies the carbons adjacent to the sulfur. We can also note that in bithiophene and terthiophene the highest BE are relative to carbons bound to S atom and connecting two rings.

The higher BE of the carbons neighboring the S atom is consistent with the higher electronegativity of sulfur compared to carbon as well as charge transfer from sulfur to carbon atom not bounded with it through resonance in the π system. The further BE increase for the carbon atom connecting the rings reproduces a trend already observed in polycyclic aromatic hydrocarbons for which the calculations provides higher BE for carbon atoms non bound to any hydrogen atom compared to external carbons bound to hydrogen atoms [50]. Starting from the thiophene spectrum, the measured spectrum can be obviously interpreted as derived from the two chemically shifted carbon lines : the part at higher energy assigned to C1, atom close to sulfur, separated by 279 meV from the C2 sub-spectrum. This chemical shift is in very good agreement with the

experimental value of 0.25 eV.

For bithiophene, the calculation assigns the higher energy peak to the C1s α -carbon atom (C4), connecting the two thiophene rings; the energy shift with the other carbon atom (C1), bound to sulfur and also to an hydrogen atom, is quite significant (583 meV) so the calculated C1 line contributes to the lower energy peak together with the lower energy lines relative to the carbon atom not bonded to sulfur (C2 and C3). The lowest binding energy of C3 compared to C2 can be ascribed to an addition of valence electron charge on the C3 site as a result of changes in bonding for the aromaticity induced by the second ring. The theoretical statistical ratio of these two groups of carbon atoms is equal 2:6 and qualitatively accounts for the relative height of the two experimental peaks. We note also the significant decrease of the energy shift between C1 and C2, 74 meV to be compared with 279 meV of thiophene.

A similar trend is found also for the calculated BE of terthiophene: the higher BE refers to the two carbon atoms (C4, C5) which connect the rings and lose their equivalence in this molecule, while the lowest BE are found for the carbon atoms not bonded to S atom (C2, C3 and C6 respectively). The energy separation between C1 and C2 reduces to such an extent that the two BE are almost degenerate while the energy shift between the (C4,C5) group and the (C1, C2) one (540 meV) is similar to that found in bithiophene as well as the lowest BE calculated for the C3 and C6 sites. The presence of a second and third rings introduces slight different aromaticity effects so that the C1 and C3 sites are destabilized by an increase of charge density, in line with the calculated decrease of C1 and C2 binding energies along the series. The first peak is therefore assigned to the binding energies of C4,C5 sites while all the other carbon lines contribute to the lowest energy experimental peak. The statistical ratio is therefore 4: 8 which apparently does not match the relative heights of the experimental peaks. Also in this case the complex vibrational structures affecting the spectral peaks prevent therefore a quantitative description of the XPS spectral shape.

3.1.3 C *K*-edge NEXAFS

NEXAFS spectra at the C *K*-edge were acquired by measuring the total ion yield (TIY) with the electron multiplier detector described in Section 2.2.1 placed in the experimental chamber in front of the ionization region. The photon flux was measured simultaneously using a calibrated Si photodiode (AxVU100 IRDTM) for the spectra normalization. The energy scale of the spectra was calibrated by

taking simultaneous spectra of the samples and of CO₂, with the characteristic transition at 290.77 eV (C 1s → π*, CO₂) [51]. The photon energy resolution was around 65 meV. The C *K*-edge NEXAFS were calculated at DFT level with the GGA PW86xPerdew functional in the Transition Potential (DFT-TP, Sec. 2.0.5) approximation.

The results of the computed excitation energies and of the oscillator strengths in C *K*-edge NEXAFS spectra are collected in Table 3.2 together with the excitation energies extracted from the experiments. The calculated energies are also reported in Fig. 3.4 where the calculated lines and profile of the total spectrum are shown in black, while the colored profiles refer to the partial contributions of the carbon non-equivalent sites. Moreover, Fig. 3.4 reports the comparison of the calculated total C *K*-edge spectra with the experimental ones. The theoretical C1s ionization thresholds are also reported in the figures; they are useful to distinguish the below-edge region of the spectrum, where the present discrete orbital description is adequate, from the above-edge region, where such an approach determines a discretization of the non-resonant continuum that is in part an artifact of the calculation, so that only qualitative information could be extracted in this region. The site-resolved excitation spectra showed in Figure 3.4 substantially represent a deconvolution of the experimental spectra into components which allow a great flexibility in analysis of the transitions and facilitate the attribution of the spectral features to specific portions of the molecules. A detailed explanation about the nature of the spectral features is shown below, while the comparison between theory and experiments is discussed later in connection to Fig. 3.5.

The calculated total C1s spectrum of the thiophene molecule (Table 3.2 and upper panel of Fig. 3.4) is characterized by a first sharp peak (**A**, at 285.65eV) which is assigned to the two C1s → LUMO transitions from both C1 and C2 carbon sites. The LUMO orbital (1π*) is appreciably localized at the sulphur atom, because of the considerable aromatic character of thiophene, and this is reflected in the lower intensity of the C2 1s → 1π* compared to the C1 1s → 1π* transition. These two NEXAFS transitions have the same energy and do not reproduce the calculated and XPS binding energy splittings of 0.28 eV and 0.25 eV respectively (see Fig. 3.4 and Table 3.2). The degeneracy of the two 1π* transitions is therefore due to a final state relaxation effect on the LUMO virtual orbital: when the half-hole is created on C1 the relaxation of the LUMO is stronger compared to C2. The second calculated peak **B** is a superposition of two excitations: from C1 (at 286.93 eV) towards a

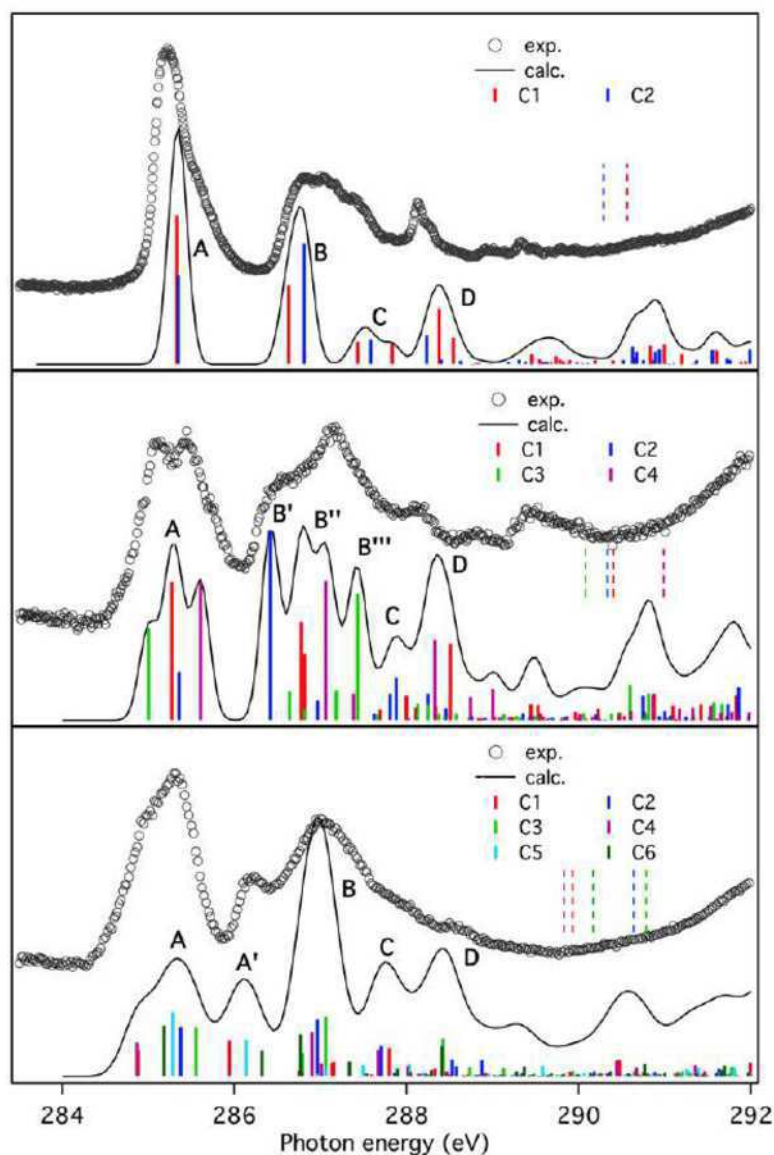


Figure 3.4: C 1s NEXAFS spectra of thiophene (upper panel), bithiophene (central panel) and terthiophene (lower panel): experimental data (circles) and calculated line shape (black solid line) with partial C_i contributions (thick colored vertical bars). The energy scale of the DFT-TP results for thiophene has been shifted of -0.35 eV in order to match the first experimental peak. The ΔKS C_{1s} ionization thresholds are also shown (colored vertical dashed bars).

Table 3.2: Experimental and calculated excitation energies (eV) and oscillator strengths of Thiophene. Only the main transitions are reported. The transition marked with (*) indicate a vibrational feature.

Peak	Site	E (eV)	fx102	Assignment	EXP
A	C1	285.64	5.86	LUMO ($1\pi^*$)	285.15
	C2	285.65	3.50	"	285.3
					285.58(*)
					285.75(*)
B	C1	286.93	3.12	σ^* (S-C)	286.69
	C2	287.11	4.73	$2\pi^*$ (C=C)	286.794
					287.047(*)
					287.166(*)
C	C1	287.73	0.89	$2\pi^*$ (C=C)	287.397
	C2	287.88	0.97	Rydberg	287.52
	C1	288.13	0.79	"	287.81
D	C2	288.53	1.15	Rydberg+	288.13
	C1	288.84	1.05	$+\sigma^*$ (C-H)	288.25
	C1	288.84	1.05	"	288.3

σ^* (S-C) virtual orbital, which is largely contributed by the S lone pairs with a smaller $2p_x$ in plane (x) component of C1, and from C2 into the second π^* ($2\pi^*$) orbital at 287.11 eV, which is localized on the four carbon atoms. The analogous $1s \rightarrow 2\pi^*$ transition from C1 is weaker and lies at 287.7 eV, therefore above the corresponding transition from C2, and contributes to the small peak **C**. The lower intensity of C1 $1s \rightarrow 2\pi^*$ compared to C2 $1s \rightarrow 2\pi^*$ transition is due to the higher localization of the $2\pi^*$ final orbital on the carbon atoms not directly bonded to the sulphur. The other two weak transitions contributing to peak **C** derive from two equivalent C1 and C2 transitions into diffuse orbitals. The last peak before threshold (peak **D** at 288.7 eV) corresponds to transitions to final C3p Rydberg MOs with some σ^* (C-H) contribution; the mixed valence-Rydberg nature of these transitions is consistent with their significant intensity. The assignment of the features substantially agrees with that previously published[52]

The bithiophene spectrum (Table 3.3 and middle panel of Fig. 3.4) shows an increased complexity due to the presence of four non-equivalent carbon sites as well as of the increased number of low-lying virtual π^* orbitals. The first structure (A, around 285.5 eV) is assigned to transitions from the four C1s non equivalent carbon atoms into the LUMO orbital, which is contributed by the valence C2 p_z and S3 p_z components and therefore comparable in nature to the LUMO orbital of thiophene. These transitions cover an energy range of about 0.6 eV due to the splitting of the C1s binding en-

Table 3.3: Experimental and calculated excitation energies (eV) and oscillator strengths of bithiophene. Only the main transitions are reported.

Peak	Site	E (eV)	fx102	Assignment	EXP
A	C3	285.00	2.68	LUMO ($1\pi^*$)	285.02
	C2	285.27	4.03	"	285.12
	C1	285.36	1.42	"	285.47
	C4	285.61	4.00	"	285.78
B'	C2	286.42	5.52	π^*	286.35
	C1	286.78	2.86	$\sigma^*(\text{S-C})$	286.53
B''	C1	286.82	1.94	π^*	286.84
	C4	287.06	4.05	$\sigma^*(\text{S-C})$	287.14
B'''	C3	287.43	3.69	π^*	287.52
C	C2	287.81	0.80	Rydberg	287.84
	C2	287.88	1.24	π^*	"
	C1	287.99	0.71	Rydberg	"
D	C4	288.33	2.34	π^*	288.17
	C1	288.50	2.23	Rydberg+ $\sigma^*(\text{C-h})$	"

ergies and their convolution gives rise to a double-peak shape with a shoulder. The relative excitation energies reflect only partly the relative energy of the core orbitals; in particular, each C1s α -carbon atom (C4), connecting the two thiophene rings, feels the proximity of the S atom and of two carbon atoms with a stronger depletion of electron density than the other carbon atoms of the rings. The C4-1s orbitals are therefore less shielded and a larger excitation energy is predicted for them which contribute to the higher energy side of peak **A**. The two C2-1s and C1-1s LUMO excitations are very close in energy and give rise to the lower energy side of peak **A** together with the C3-1s LUMO excitation, which is the lowest in energy and accounts for the most shielded C1s orbital compared to other carbon atoms, in agreement with the calculated binding energies (see Table 3.1 and Fig. 3.3). The C1 and C4 C1s \rightarrow LUMO transitions are the most intense partial contributions of the **A** peak: this is a consequence of the localization of the LUMO on C1 and C4.

The second calculated feature (**B**), around 287 eV, has a three peaked shape (denoted as **B'**, **B''** and **B'''**) as a result of the convolution of the many intense transitions falling in this energy range. The nature of these transitions roughly corresponds to those contributing to the thiophene **B** peak, namely towards the $2\pi^*$ and the $\sigma^*(\text{S-C})$ antibonding orbitals. The $2\pi^*$ orbital resembles the LUMO composition maintaining a significant $S3p_z$ component consistent with an increased aromatic character compared to thiophene. In particular, the **B'** component of the peak **B** derives from the $\text{C2} \rightarrow 2\pi^*$ transi-

tion from the C2 site (at 286.42 eV) while analogous transitions from the C1 and C3 sites (at 286.77 eV and 287.43 eV) contribute to the **B''** and **B'''** components respectively. The strongest π^* transitions still involve the carbon atoms not directly bonded to a sulphur atom, as in the thiophene. The excitations to the σ^* (S-C) antibonding orbitals contribute significantly to **B''** component and derive from the C1 and C4 carbon sites directly bonded to a sulphur atom (at 286.77 eV and 287.06 eV respectively). The assignment of the main features substantially agrees with that proposed in Ref. [53] for a multilayer film deposited on Ag(111).

Peak **C** and **D** should be characterized as superposition of valence and Rydberg excitations. The most intense transitions are towards final orbitals of π^* character (from C2 site at 287.88 eV, peak **C** and from C4 site at 288.33 eV, peak **D**), their reduced intensity compared to the lower energy π^* transitions reflects the decrease of the valence $C2p_z$ contribution of the $C1s$ excited site in the higher π^* virtual MO. The less intense lines are assigned to transitions into diffuse orbitals of mainly $C3p$ -Rydberg character.

The complexity further increases in the terthiophene spectrum (lowest panel of Fig. 3.4 and Table 3.4); in this molecule there are six non equivalent carbon atoms and even greater number of low-lying π^* orbitals. The peak **A** arises from the $C1s \rightarrow$ LUMO transitions from all the six carbon sites whose contributions are highlighted in figure 2. The larger excitation energies are predicted for the C4 and C5 carbon sites which are less shielded being directly bounded to the sulfur atoms and connecting two rings, as already found for the 2T molecule, and in agreement with the energy position of the calculated IPs. However, the differential relaxation effects on the π^* low-lying orbitals, depending on the localization of the carbon core hole, prevent an analysis of the following features based on a regular energy shift of the site-resolved excitation spectra following the energy position of the IPs.

The feature **A'** corresponds to transitions to the second π^* orbital ($2\pi^*$) from C6, C2 and C1 sites while the transition from C4 site is shifted at higher energy (286.79 eV, peak **B**). We do not observe analogous transitions from C3 and C5 sites because the $2\pi^*$ relative final orbitals have a negligible $C2p_z$ contribution of the carbon excited site. The **B** peak arises from several transitions to π^* orbitals overlapped on the stronger σ^* (S-C) transitions from the C1, C4 and C5 sites; this attribution confirms the mixed nature of peak **B** found also for thiophene and bithiophene. The **C** and **D** peaks are still contributed by transitions to virtual orbitals with π^* character; the calculations indicate that these higher energy π^* orbitals are mostly

localized on carbon atoms with a reduction of the $S3p_z$ contribution as well as of the conjugation among the rings. The progressive intensity decrease of these transitions reflects the general reduction of the $C2p_z$ valence character of the final MOs; in the region of peak **D** also transitions to diffuse MOs with Rydberg $C3p$ components are present with lower intensity.

Table 3.4: Experimental and calculated excitation energies (eV) and oscillator strengths of Terthiophene. Only the main transitions are reported.

Peak	Site	E (eV)	fx102	Assignment	EXP
A	C3	284.87	2.26	LUMO $1\pi^*$	
	C6	284.88	1.77	"	284.87
	C1	285.18	3.38	"	285
	C2	285.28	0.92	"	285.35
	C5	285.37	3.27	"	285.42
	C4	285.55	3.29	"	
A'	C6	285.94	2.39	$2\pi^*$	
	C2	286.13	4.27	"	286.15
	C1	286.32	1.70	"	
B	C1	286.77	2.80	$\sigma^*(S-C)$	
	C4	286.79	1.56	$2\pi^*$	
	C3	286.90	2.96	π^*	286.62
	C5	286.96	3.81	$\sigma^*(S-C)$	286.91
	C2	287.05	2.44	π^*	287.32
	C4	287.06	3.99	$\sigma^*(S-C)$	
	C6	287.15	0.97	π^*	
C1	287.34	1.01	π^*		
C	C3	287.67	1.75	π^*	287.9
	C5	287.70	2.05	π^*	288.04
	C6	287.80	1.88	π^*	
D	C1	288.41	2.03	Rydberg	
	C4	288.42	2.52	π^*	287.55
	C5	288.53	1.11	π^*	288.66
	C5	288.87	1.07	π^*	

In Fig. 3.5 the $C1s$ NEXAFS spectra computed by the DFT-TP scheme are compared with the gas phase experiments and with the analysis of the experimental line shapes using the second derivative. This analysis is performed filtering first the experimental noise applying the first derivative; secondarily the noise on the first derivative was further filtered and the second derivative was applied. This procedure is useful to discover structures and to determine their energy positions even when they are not immediately visible. On the other hand some informations on the small structures may be lost during the filtering; for this reason, when there is the indication of a bunch of small structures close together, only the average position

has been marked. The thiophene calculated profile (upper panel) has been shifted on the energy scale (+0.35eV) to match the first peak of the experiment. In this way, the relative energy shift among the calculated transitions, which actually represents the most significant observables, is preserved.

A general good agreement is reached between experiment and theory, in particular the theoretical results correctly describe the main features of the experimental curves and the energy separation among the peaks. A clear correspondence between calculated and experimental peaks is apparent in the thiophene spectrum; the major discrepancy concerns the broad shape of the experiment which is rich in features and is not reproduced by the calculations. Such disagreement can be caused by vibronic effects, found to influence also the XPS C1s profile especially in thiophene (see Ref. [49] and our discussion of the XPS line shape) but are not included in the present computational model. The most evident case is the LUMO of 1T, corresponding to peak **A**, where electronic calculations expect only two excitation energies, while in experiment four are found. It is straightforward to attribute the first two to C1 and C2 $1\pi^*$ orbitals, and the third at 285.58(*) and fourth at 285.75(*) to their vibrational progression. Similarly for group **A**, the features in group **B** at 286.69 and 286.794 correspond to adiabatic peaks while 287.047(*) e 287.166(*) are vibrational. The following 287.397, 287.52 and 287.81 correspond to the computed ones and most probably they overlap with the vibrations. The ones at 287.73, 287.88 and 288.13 correspond to calculated Rydberg peaks. Such effects could be also responsible for other discrepancies between theory and experiment in the bithiophene and terthiophene spectra, in particular as concerns the first peak. The intensity distribution of the experimental double-peak feature of the bithiophene spectrum is not properly reproduced by the calculation while in the terthiophene spectrum the theory underestimates the first peak intensity with respect to the second one. We would underline that the conformational flexibility of bithiophene and terthiophene does not allow a one-to-one match of the spectral features because the presence of other conformers is also possible.

In summary, a comparison between the DFT-TP electronic calculations and experiment is fully satisfactory as far as the relative excitation energies are concerned, while the intensity distribution is less quantitative. We tend to ascribe this problem to the neglect of vibrational effects in the computational approach, also on the basis of previous vibrationally resolved studies on NEXAFS C1s spectra of both simple aromatic molecules and polycyclic aromatic hydro-

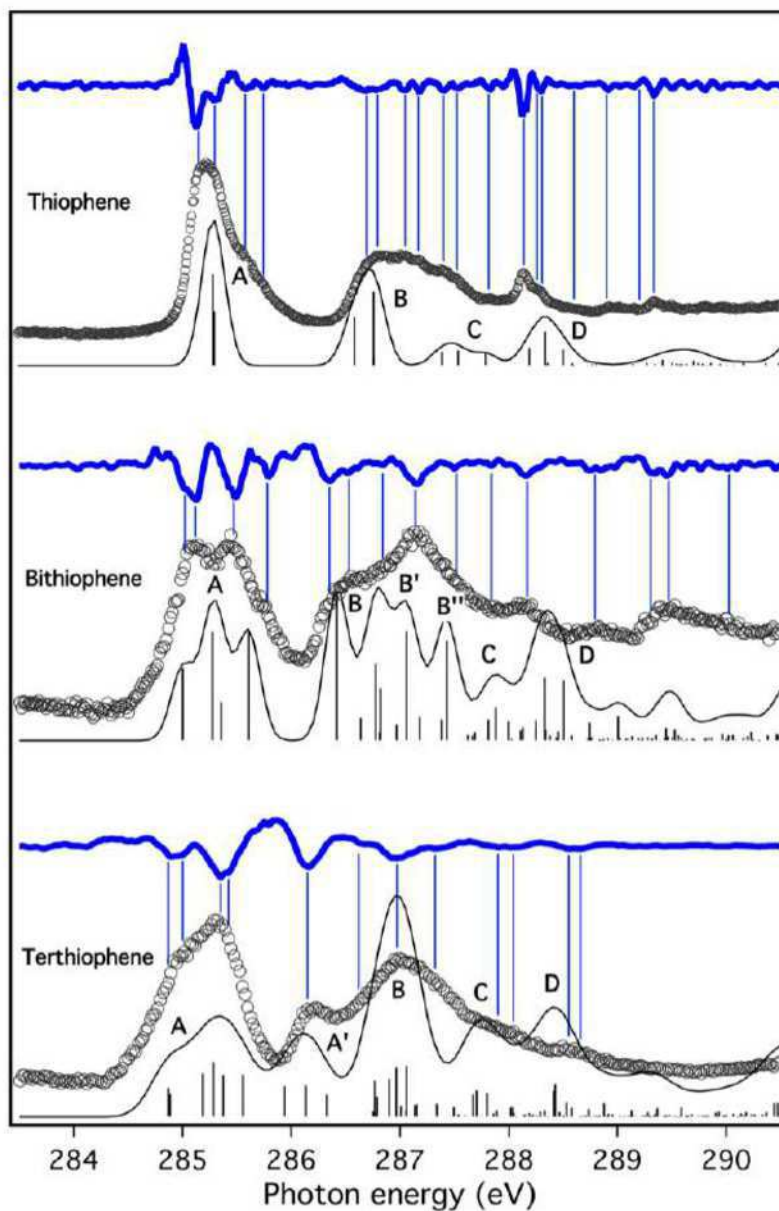


Figure 3.5: C 1s NEXAFS spectra of thiophene (upper panel), bithiophene (central panel) and terthiophene (lower panel): experimental data (circles) and calculated DFT-TP results (black solid lines and vertical bars). The energy scale of the DFT-TP results for thiophene has been shifted of -0.35 eV in order to match the first experimental peak. At the top of each spectrum the second derivative of the experiment is also shown (blue solid line); the main minima are indicated with the thin vertical blue bars.

carbons. It is worth noting that the present electronic calculations are suitable for an unambiguous assignment of the experimental features despite the vibrational effects can play a role in the intensity distribution.

We finally address the evolution of the spectral features of the oligothiophenes when increasing the number of thiophene rings. The lower energy features (**A** and **B**) maintain their nature along the series, despite the increasing complexity and the enlargement of the peaks. The first π^* peak (**C** 1s transitions to the LUMO) shifts to lower energy (about 0.5 eV) from thiophene to bithiophene while it does not change further from bithiophene to terthiophene: this trend can explain a stabilizing effect due to the aromaticity, which is stronger in passing from one to two rings than in adding a third ring. The σ^* (S-C) transitions maintain their energy almost constant along the series because the involvement of a single bond is not influenced by aromaticity and always falls in the region of peak **B** together with the π^* transitions. The number of overlapping transitions increases at higher energies (peaks **C** and **D**) preventing a strict correspondence along the series.

3.2 The electronic characterization of biphenylene

3.2.1 Introduction

The biphenylene molecule ($C_{12}H_8$), shown in Fig. 3.6, is a polycyclic aromatic hydrocarbon (PAH) composed as the conjunction of two benzyne molecules (C_6H_4). It can also be viewed as by two benzene rings connected by a cyclobutadiene ring. While benzene is highly aromatic (and highly stable), cyclobutadiene is highly anti-aromatic (and thus unstable). The electronic structure with $4n\pi$ electrons, according to Hückel's rule, categorizes biphenylene as an antiaromatic molecule, but the relatively long bond length between the two benzyne units weakens the interaction between them. For this reason biphenylene shows an intermediate character between the anti-aromatic ring and aromatic ring. In anti-aromatic molecules, the $4n\pi$ electrons typically have a more localized character with respect to the more delocalized $4n+2\pi$ electrons, which are characteristic of aromatic molecules. As a result of this different electronic structure, the anti-aromatic molecules are characterized by improved chemical reactivity and lower stability.

It is interesting to notice that biphenylene is one of the most sta-

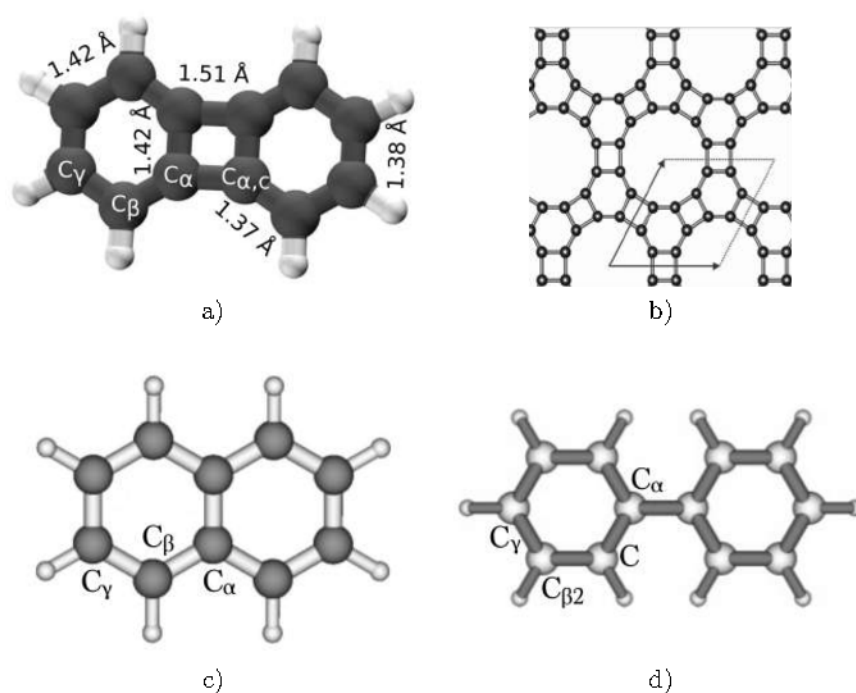


Figure 3.6: a) optimized structure of biphenylene; b) structure of BPC, from Ref. [10]; c) structure of naphthalene, from Ref. [54]; d) structure of biphenyl, from Ref. [55]

ble anti-aromatic molecules making it very suitable for traditional spectroscopic experiments. Biphenylene has been the target of several experimental and theoretical studies for it is expected to play a major role as a novel organic material: in the halide-functionalized form it is the initial precursor of a 2D porous graphite-like molecular network called biphenylene carbon (BPC, Fig. 3.6) that was first described by Balaban et al. [9]. BPC is characterized by bands with good dispersion and delocalized frontier orbitals [10, 11], so it could be an ideal structure for many electronic applications. Moreover biphenylene sheets, originating from the biphenylene dimer, have also been hypothesized as a material with expected high versatility: calculations predict that, depending on the morphology and on the dimensions of the investigated structure, a metallic or a semiconductor character can be obtained.

We have studied biphenylene in gas phase through different techniques: experimentally by x-ray photoemission spectroscopy (XPS) and near-edge x-ray absorption spectroscopy (NEXAFS) and theoretically, with DFT simulations in excellent agreement with the experimental data. The results shown in this Section appeared in J.

Table 3.5: Comparison of the calculated bond lengths in Å of biphenylene with available experimental crystallographic bond lengths provided in Ref.[56]. $C_{\alpha,c}$ denotes a C_{α} of the connected benzyne ring.

	C_{α} - C_{α}	C_{α} - $C_{\alpha,c}$	C_{α} - C_{β}	C_{β} - C_{γ}	C_{γ} - C_{γ}
experiment	1.4294	1.5137	1.3786	1.4242	1.3913
computed	1.4183	1.5065	1.3675	1.4153	1.3839

Lüder *et al.* (**PAPER VI**). In this section the electronic structure derived from the theoretical calculations is described, and it is used for the interpretation of the experimental results on gas phase in Section 3.2.2.

The study on the isolated molecule was then continued to the study of the condensed phase. First the electronic structure of biphenylene films on Cu(111) was investigated (Section 3.2.3). Secondly the molecular orientation in the overlayer was characterized performing NEXAFS for different film thicknesses. This allows us to discover a dependence of the molecular arrangement on the film thickness but it suggests also an important influence of the substrate on the film characteristics.

DFT calculations of the electronic structure were performed in the group of Dr. Barbara Brena at the University of Uppsala. Fig. 3.6 shows the optimized structure of biphenylene together with the intermolecular bond lengths. The calculated bond lengths are in close agreement with the experimental values of Table 3.5 (from [56]) being in general just 0.01 Å shorter than the latter.

Biphenylene is a flat molecule with three non-equivalent carbon atoms labeled as C_{α} , C_{β} and C_{γ} . The C_{α} are the four C atoms that connect the two benzene rings to each other, as shown in Fig. 3.6. C_{β} and C_{γ} label the middle and the outer C atoms of the benzene rings, respectively. The computed distance between two C_{γ} atoms is 1.39 Å. The bond lengths between the C_{γ} and the C_{β} as well as between C_{α} and C_{β} are slightly shorter, of 1.37 Å. The distance between the two C_{α} in the same ring is 1.42 Å, while two connected C_{α} in different rings, indicated as C_{α} - $C_{\alpha,c}$ bond, have a bond length of 1.51 Å. The relative long bond distance between the C_{α} atoms of connected benzene rings is a consequence of the anti-aromatic character of the molecule.

The molecular orbitals (MO) of the four highest occupied states, shown in Fig. 3.7, illustrate the spatial configuration and the localization/delocalization of the orbitals, as well as the character of the bonds, e.g. bonding, non-bonding or anti-bonding.

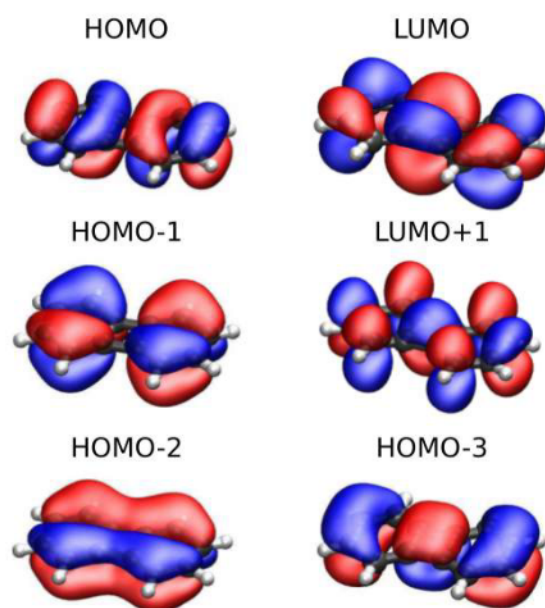


Figure 3.7: The orbitals between HOMO-3 and LUMO+1 of biphenylene are given. Orbitals are shown including their phases as red and blue isodensity surfaces.

3.2.2 Isolated biphenylene molecule - valence and core-levels

PES and NEXAFS spectra of biphenylene have been recorded at the Gas Phase beamline at Elettra. Biphenylene, which has a melting point of about 70 °C, was purchased from Sigma-Aldrich as a powder with minimum purity of 99% and introduced in the experimental chamber without further purification. The sample was sublimated using a custom built resistively heated furnace, based on a stainless steel crucible. The spectra presented in this section have been recorded at a working temperature of 85 °C. The PES data were recorded using a SES-200 electron analyzer described in Section 2.2.2. The valence band PES was recorded at a photon energy of 50 eV with an overall resolution of about 50 meV and it has been calibrated with the Xe $5p_{3/2,1/2}$ lines [57]. The C 1s spectrum has been recorded at a photon energy of 332 eV with an overall resolution of around 75 meV, and it has been calibrated with the C 1s in CO₂ (297.6 eV [48]).

The photoabsorption spectra at the C *K*-edge were acquired with a photon energy resolution of 70 meV, by measuring the total ion yield (TIY) with a channel electron multiplier placed near the ion-

ization region. The photon flux was measured simultaneously with a calibrated Si photodiode (AxVU100 IRDTM) for normalization. The energy scale of the spectrum was calibrated by taking simultaneous spectra of the samples and of CO₂, with the characteristic transition at 290.77 eV (C 1s → π* [51]).

Fig. 3.8 compares the experimental XPS spectrum, red dotted, with the theoretical curves after convolution with a gaussian function (solid lines) and a skew gaussian function (dashed lines), respectively. Additionally, the spectra originated from the three non equivalent carbon atoms are provided. The calculated XPS energies are shown as bars.

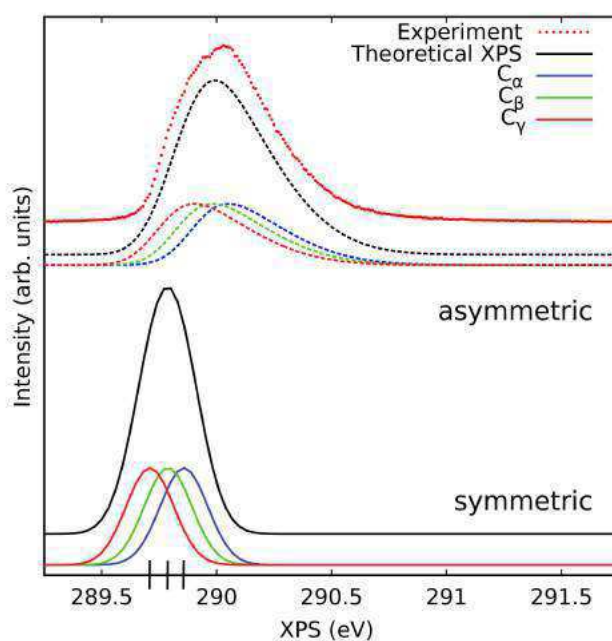


Figure 3.8: Comparison between the experimental (dotted red curve) the theoretical XPS spectrum convoluted with gaussian functions (solid curves) and with skew gaussian functions (dashed curves). The skew parameter α has been determined to be 2.14 by fitting to the experiment. Bars show explicitly the calculated XPS energies

The experimental C1s spectrum consists of a large asymmetric peak with a FWHM of almost 0.5 eV at 290.1 eV. The XPS energies of the three chemically non- equivalent C atoms in biphenylene were calculated to be 289.82, 289.75 and 289.67 eV for the C_α, the C_β and the C_γ, respectively, after alignment to the experimental spectrum. After the fitting procedure including the skew parameter described above, the main experimental features could be reproduced. For molecules like naphthalene and biphenyl (Fig. 3.6) comparable shifts

in the 1s core levels have also been found for the carbon atoms connecting the two benzene-like rings [54, 55].

The comparison of the XPS shifts can give valuable insights into the structural and chemical differences between biphenylene and similar molecules composed of two benzene rings, here naphthalene and biphenyl, as can be seen in Table 3.6. We use here the convention of labeling the inner C atoms of the benzene ring as C_α , the outer C atoms as C_γ and the C atoms between those two as C_β for biphenyl and naphthalene. This has the consequence that the biphenyl molecule has two non-equivalent C_β atoms, e.g $C_{\beta 1}$ and $C_{\beta 2}$ which are connected to the C_α and the C_γ , respectively.

Significant differences in the XPS shifts for biphenylene occur with respect to the naphthalene and biphenyl molecules. In detail, the $\Delta(C_\alpha - C_\gamma)$ shifts in the biphenylene molecule is about 0.17 eV smaller while $\Delta(C_\beta - C_\gamma)$ is larger for the biphenylene molecule and in between the shift seen in $\Delta(C_\beta - C_\gamma)$ and $\Delta(C_{\beta 2} - C_\gamma)$ for the biphenyl molecule. The latter shift indicates an accumulation of charge around the C_β which is supported by the ground state orbitals. These XPS shifts indicate some similarities in the electronic structure of these molecules.

The bond between the two benzene rings in biphenylene is of different character than the equivalent bonds in the biphenyl and in the naphthalene molecule. Also, the bonds between the C_β and the C_γ of the biphenylene molecule are more alike to the biphenyl molecule than to the naphthalene molecule. As discussed above, the anti-aromatic character of biphenylene causes distinct structural features and, in particular, it influences the bond lengths along the four-side rings. Consequently this also affects the rest of the structure and causes a localisation of charge in each of the benzene rings centered at the C_β .

Table 3.6: Relative C1s XPS shifts in eV among the non-equivalent C atoms in biphenylene, biphenyl [55], and naphthalene [54].

	$\Delta(C_\alpha - C_\gamma)$	$\Delta(C_{\beta 2} - C_\gamma)$	$\Delta(C_\beta - C_\gamma)$
Biphenylene (theory)	0.15		0.08
Biphenyl	0.34	0.14	0.03
Naphthalene	0.32		0.02

The valence band spectrum is shown in Fig. 3.9 together with the calculated DOS obtained by the DFT calculation and partial density of states (pDOS) of the individual carbon contributions. The peaks or group of peaks are labeled from **A** to **H**; **A** represents the HOMO. The calculated spectra are shifted by 1.9 eV to match

the experimental energies. The experiment are well reproduced by the calculations: especially, states between HOMO at 7.6 eV down to 10.5 eV. In this energy range there are four eigenstates, which correspond to the four experimental peaks **A** to **C**, besides the small shoulders, which are due to vibrations [54, 55]. Peak **A** (HOMO) has main contributions from the C_α and the C_γ atoms. Peak **B** (HOMO-1) at 8.9 eV has main contributions from the C_α and the C_β peaks. However, the correct intensity of the peak, almost twice as high in comparison to the HOMO peak, could not be reproduced in the calculations. HOMO-2 at 9.7 eV has main contributions from the C_α and the C_β atoms, while HOMO-3 at 10.0 eV has mainly contributions from the C_α and the C_γ atoms.

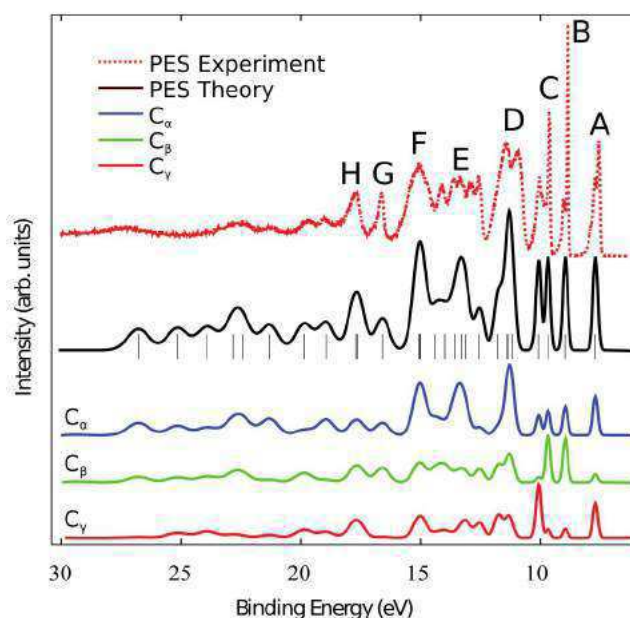


Figure 3.9: Comparison between the experimental PES, dotted red curve, and the computed DOS and pDOS's. The total DOS is given as solid black curve together with the eigenvalue spectrum indicated as bars below the DOS while the blue, the green, and the red curves represent the pDOSs from the C_α , the C_β , and the C_γ , respectively. The experimental binding energies are compared to the negative of the computed eigenvalues.

At binding energies higher than 10.5 eV, vibrational effects increase the differences between theory and experiment. The group of peaks labeled with **E** are reproduced to some extent and has mostly C_α character. The peaks **F** to **H** are well matched with the experiment even though peak **F** is slightly overestimated. Interestingly, the electronic states of the peaks **D** to **F** are mostly represented by

electrons from the C_α atoms, which form the square ring in biphenylene. In contrast, the states between HOMO and HOMO-3 consist of mixed contributions from at least two non equivalent C atoms, but always including the C_α atoms.

The experimental and the theoretical XAS spectra are shown in Fig. 3.10. Excellent agreement is achieved from the first excitation energy at 286.5 eV to the beginning of the continuum region at about 293 eV. The first experimental excitation peak at 286.5 eV has a broad shoulder towards higher energies and it is composed of contributions from all carbon atoms as shown by the calculations. However, the C_α and the C_γ contribute at about the same resonance energy of 286.5 eV and 286.6 eV, respectively, whereas the main contributions from the C_β is at a slightly higher energy (286.9 eV) resulting in a broadened feature in the total spectrum.

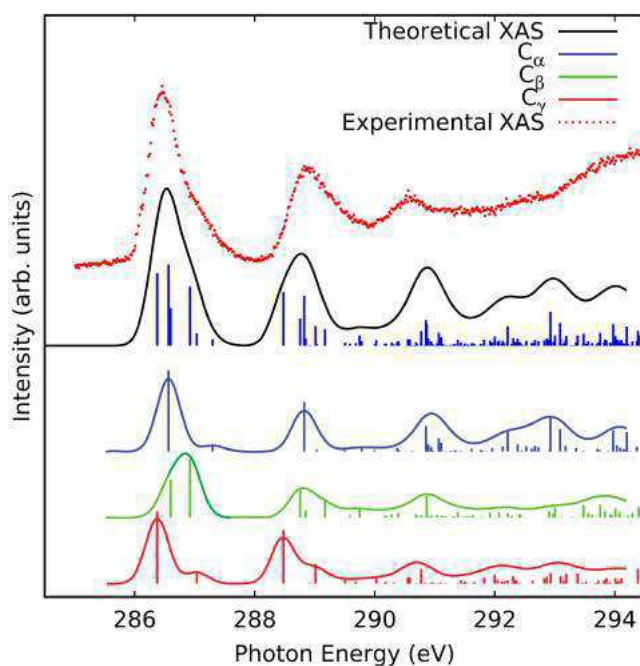


Figure 3.10: The experimental XAS spectrum, dotted red curve, is compared to the results of the TPA approach (see Sec. 2.0.5). The total theoretical XAS spectrum is the solid black curve and the C atom contributions are the blue, the green, and the red curve for the C_α , the C_β , and the C_γ , respectively. The black bars below the total theoretical spectrum represent the absolute values of the dipole transition associated oscillator strengths.

The first resonance energies of the C_α and the C_γ are very similar to each other and their small variation in the energy position of 0.1 eV can be induced through symmetry breaking by the core-hole.

The LUMO and LUMO+1 have an energy difference of 0.4 eV in the GS calculations and the same energy difference can be found on the transition to LUMO and LUMO+1 in the TPA calculation. Moreover, the C_α and the C_γ have additional resonances between 286.9 eV and 287.4 eV which also contribute to the shoulder of the first experimental peak.

Similarly, the second peak at about 288.9 eV is also composed from contributions of all non-equivalent carbon atoms. In contrast to the first peak, the broadened feature is here composed of contributions from all C species, but the C_α and the C_γ atoms are the main contributors. Excellent agreement between theory and experiment was obtained for the energy difference of 2.4 eV between the first and the second peak. The third experimental peak, consisting mainly of contributions from the C_α , is at an energy position of 290.6 eV which is slightly overestimated by 0.3 eV.

The observed discrepancies among theoretical and experimental data could be due to the various effects. For example, the possibility of vibrational contributions could affect the spectra to spread various electronic contributions, minimizing the overlap between $1s$ and π^* orbitals [50] as well as deformations of the molecular structure as they can occur during excitation processes. We have shown that the XAS peaks are composed from contributions of all non-equivalent carbons.

The asymmetry of the first transitions could be explained as the overlapping of resonances shifted in energy (C_β with respect to C_α and C_γ) that corresponds to the computed XPS shift of the non-equivalent carbon atoms. These observations are expected also for similar molecules like biphenyl and naphthalene. The relative shift, together with the observed omnipresence of the C_α electronic states and the C_γ contributions to HOMO in the total DOS illustrate significant characteristics which may provide a promising starting point for studies aiming at modifying its properties through substitution of ligands or adsorption on (see next Section).

3.2.3 Band structure and molecular orientation of biphenylene films

In order to investigate the behavior of biphenylene as precursor of 2D structures like biphenylene carbon, we have accomplished a preliminary characterization of biphenylene films deposited on a Cu(111) substrate, through Photoelectron Spectroscopy (PES) and Near-edge x-ray absorption spectroscopy (NEXAFS) at the C $1s$ edge. In the previous Section we studied the electronic structure of bipheny-

lene in gas phase, disentangling the contributions of each carbon sites, C_α , C_β and C_γ , to the molecular electronic structure.

In the present Section, the occupied core and valence levels as well as the non-occupied valence states of biphenylene in films of different thicknesses are examined, to elucidate the molecule-substrate interactions (low coverage film) and the molecule-molecule interactions (high coverage film). For a deeper understanding of the intermolecular interactions, the results of the thicker films have been also compared to the previous gas phase measurements and to DFT calculations simulating the total and the partial density of states (tDOS and pDOS, respectively) considering π and σ orbitals for a single biphenylene molecule. Moreover, the molecular orientation in the overlayer, of importance for implementing these kinds of film in molecular electronics, has been characterized performing, for all the obtained film coverages, NEXAFS at different geometries of the sample with respect to the impinging light.

In Fig. 3.11 we show the C 1s spectra of biphenylene films at high, intermediate and low coverage. Only one very intense peak characterizes the photoemission spectra for the three coverages, despite the three non-equivalent atoms in the molecule (Fig 1). However, the main peak line shapes and positions exhibit an evolution as a function of biphenylene thickness. At low coverage (Figure 2c) the peak is asymmetric and is centered at 284.5 eV. Upon further biphenylene depositions, the peak becomes symmetric and shifts to higher BE, being centered at 284.9 eV for intermediate coverage (Figure 2b) and 286 eV for high coverage (Figure 2a).

The low coverage C1s photoemission line shows the typical asymmetric shape, also observed for other low coverage films of carbon-based molecules on metallic substrates [58, 59]. The asymmetry originates from photoelectron inelastic scattering with the electron-hole pairs in correspondence of the Cu Fermi level (E_F), i.e. the high density of state at E_F allows for shake-up transitions from states just below E_F to empty state just above E_F . At higher film thicknesses the substrate is more covered by adlayers, the inelastic scattering is less favorable and the line shape may become more symmetric, as observed in Fig. 3.11 .

The C 1s BE shifts of the different biphenylene coverages is also attributed to the more effective core hole screening in the low coverage by the electronic cloud of the metal crystal, resulting in a lower BE for the emitted photoelectron. For thicker films, the electrons screening of the core hole is instead less effective and the BE of the core level peak increases, giving a $\Delta(\text{BE})$ of 1.6 eV for the high coverage sample, with respect to the low coverage sample. By the

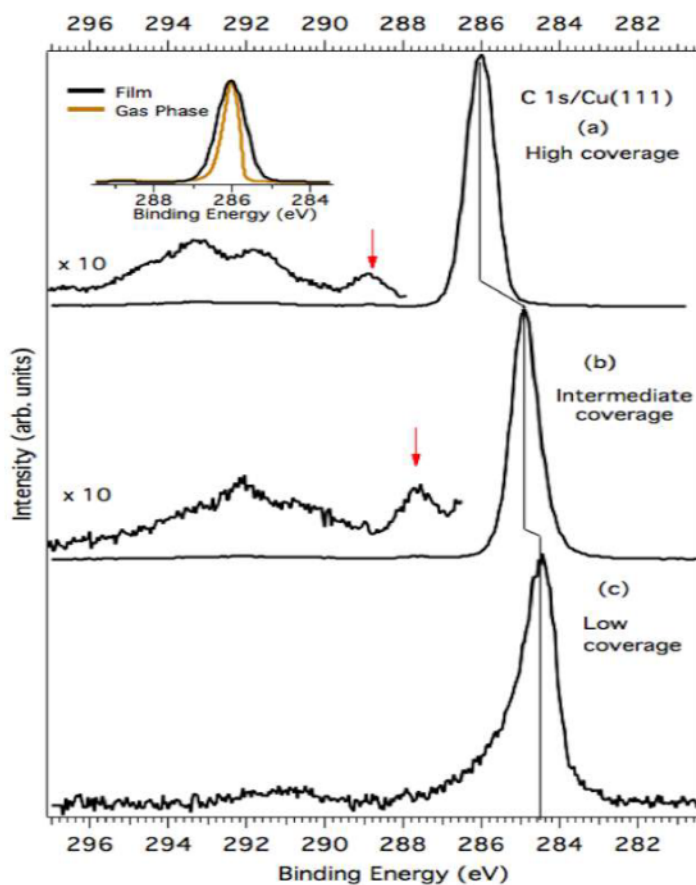


Figure 3.11: C 1s photoemission spectra of a biphenylene film of (a) high (100 Å), (b) intermediate (30 Å) and (c) low (7 Å) coverage, acquired with $h\nu=400$ eV and an overall resolution of about 90 meV. In figure (a) and (b) the biphenylene shake-up region has been enlarged for sake of clarity. Red arrows indicate the position of the shake-up peak at 2 eV from the main line. Inset: comparison between the C 1s spectra of the high coverage film and of biphenylene gas phase.

comparison of the shake up regions (i.e. above 287 eV), important information on the interactions between the adsorbed molecules and the substrate can be deduced. In Figure 2(a) and 2(b), the shake-up regions have been enlarged for sake of clarity. While in the low coverage spectrum the shake-up region is made of a broad peak, centered at about 291 eV, in the intermediate and high coverage situation, shake-ups show rather complex and structured features. Another notable difference is the lack in the low coverage C 1s PES spectrum of the shake-up feature at about 2 eV from the main line, instead clearly seen for the film of higher biphenylene coverages (indicated by red arrows in the figure).

The shake up spectra in aromatic molecules of increasing com-

plexity, from benzene to C60, were investigated both experimentally and theoretically in several studies[60, 61, 62]. According to these studies, ionizations at different sites in aromatic molecules result in different contributions to shake up spectra, that can be disentangled by theoretical calculations[61]. The shake up intensities at higher BE (about 6 eV from the main line) would correspond to intraring (local) excitation accompanying the photoelectron process, i.e. charge moving within the ring of the core hole. Instead, the shake up intensity closer to the main line would be ascribed to excitations which move charges from atoms far away in the molecule to the core hole site and its neighboring sites. In case of biphenylene, we could then conclude that the first shake up features at about 2 eV from the main line would be due to interring excitations, i.e. it would be a non-local shake up which gets charge coming from the other rings. Thus, the lack of the low binding energy shake up and the asymmetric line shape of the C1s spectrum for the low coverage biphenylene show a significant modification of the molecular electronic structure, due to the interaction with Cu(111) surface.

The high coverage C1s spectrum Fig. 3.11 is compared with the gas phase spectrum, since at this coverage the substrate contribution is minimized and the film would retain most of its molecular character. As seen in the insert of Fig. 3.11, the gas phase C1s peak is much narrower (FWHM = 0.5 eV) than the film line (0.9 eV), partly due to the better resolution of the gas phase (75 meV) results, with respect to the film (90 meV) results. However, the two peaks have a clearly different line profile, symmetric for the film, asymmetric for the gas phase. As already shown in the gas phase and similarly to biphenyl [55] and naphthalene [54], the asymmetry of the gas phase line is ascribed to intramolecular vibrations, which give rise to an asymmetric tail. In the film the situation is different, since many of the intramolecular vibration modes can be frustrated. Furthermore, the low temperature of the Cu substrate during the measurements, can also contribute to quench the effect of the vibrations resulting in a more symmetric line shape.

Valence spectra acquired on low coverage and intermediate coverage samples are dominated by the strong Cu valence band features, which completely hide the biphenylene valence photoemission peaks in the low BE region. A general shift towards higher binding energies, when biphenylene thickness increases, characterizes the remaining valence peaks. This is also ascribable to the screening of the underlying Cu substrate, as already seen in C 1s spectra. However, since no other information could be extracted from these data, they are not shown.

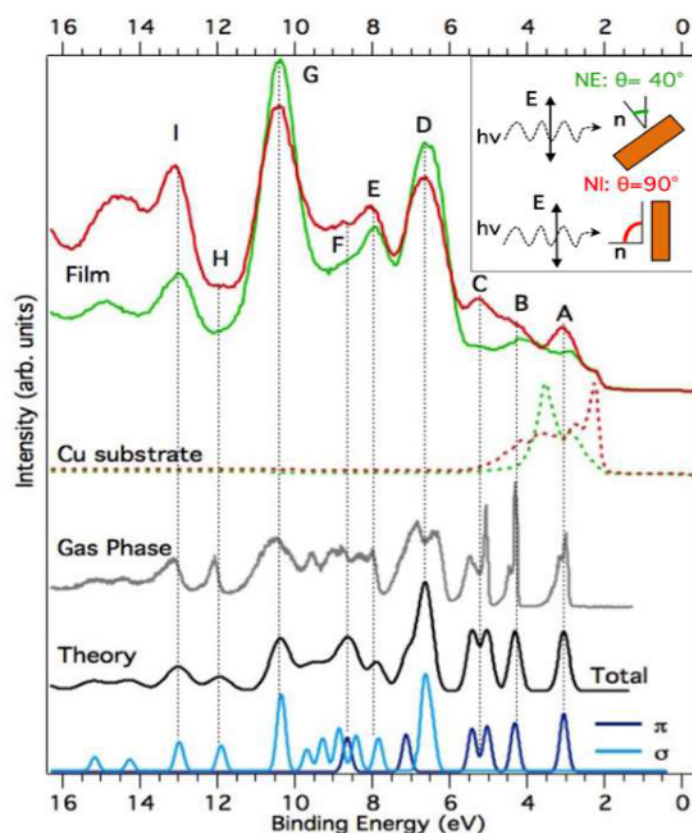


Figure 3.12: VB spectra of the high coverage biphenylene film in the two acquisition geometries of normal emission NE (green) and in-plane-polarization IPL (red). The spectra of the clean Cu(111) acquired with the same geometries are shown as dashed lines. The gas phase, the tDOS and the pDOS of π and σ molecular orbitals are also displayed. Film and gas phase spectra were acquired with $h\nu = 130$ eV and 50 eV, respectively. Insert: schematic representation of the acquisition geometries indicating the angle θ between the surface normal \vec{n} and the direction of the polarization vector \vec{E} of the incident light.

In Fig. 3.12 we show, instead, the VB spectra of a high coverage film, acquired in normal emission NE and normal incidence NI¹, with θ (angle between the polarization vector \vec{E} of the incident radiation and the surface normal \vec{n} of 40° and 90° , respectively (see insert in Fig. 3.12). The photon energy of 130 eV used for the acquisition allowed to measure almost at the maximum surface sensitivity condition, with an electron inelastic mean free path of about 10\AA [63]. In the same figure we report gas phase and DFT tDOS and pDOS for the isolated molecule, taking into account the contributions of π

¹NE (Normal Emission) is a geometry used in photoemission with the sample normal parallel to the analyzer direction (in our case, $\theta = 40^\circ$). Although NI and in-plane-polarization IPL (see Section 2.0.4) are equivalent, in photoemission the former expression is mostly used

and σ molecular orbitals.

A general good agreement between film, gas phase and calculated spectra is observed, even though the film lines, like for C 1s core level, are affected by a significant broadening. The relative positions in BE of the structures from **D** to **I** recall those of the theory and gas phase spectra, whereas there is not a perfect correspondence among the peak intensities, probably also due to different photoemission cross sections at the two photon energies used, 130 eV for film and 50 eV for gas phase.

The HOMO, HOMO-1 and HOMO-2 peaks (**A**, **B**, **C** in the figure) are less distinguishable in the film with respect to the gas phase. Contributions from the Cu substrate are visible in correspondence of the most intense Cu valence peaks, at 3.5 eV in NE and at 2.2 eV in IPL. The photoemission contributions from the Cu(111) substrate can also explain why the spectral features of the film at low BE are less resolved and less intensive than in the gas spectrum, even at such coverage that would correspond to a film of molecular character. Moreover, considering the high coverage of the film, the intensity of the still observable substrate valence band features suggests that the film is not uniform.

We can exploit the different intensities of the VB peaks for the two different geometries to obtain information about the orientation of the molecules on the surface. In fact, as it is well known, in planar organic molecules like biphenylene, π and σ orbitals have well defined directions in space: in plane and perpendicular to the molecular plane, respectively. Then, the synchrotron linearly polarized light can be used to probe the direction of molecular orbitals, i.e. the orientation of the molecules in the film. This is generally done with NEXAFS spectra[26], since the observed resonances naturally represent the excited non-occupied π and σ orbitals. However, it is also possible to determine the orientation of the molecules by enhancing the different contributions from π and σ orbitals to the valence PES structures varying the orientation of the sample with respect to the incident light, like done, for example, by Åhlund et al. [64].

The comparison with the DFT simulations (Fig. 3.12, at the bottom) reveal that the peaks due to π orbital contributions (**A**, **B**, **C**), are more intense in IPL with respect to NE, while peaks due to σ orbitals contributions (**D**, **E**, **G**) show the opposite behavior. Considering that the polarization vector \vec{E} is perpendicular to the light direction (and changes with respect to the surface depending on the incidence angle of the light), in the high coverage situation the

molecules appear to stand on the surface. High BE peaks (**H**, **I**) deviate from this behavior, probably because of the stronger contribution from the background. The estimated molecular orientation in the film, is also confirmed by our NEXAFS measurement, as it will be shown in the following.

NEXAFS results of the thicker biphenylene film, taken at NE geometry, presented in Fig. 3.13, are compared to the gas phase spectrum and theoretical NEXAFS simulations for the single molecule, showing the tDOS and the pDOS from π^* and σ^* resonances. The film spectrum shows very distinctive features: those around 285, 287.5 and 289 eV are originated from the electron transition from the C $1s \rightarrow \pi^*$ orbitals while from 293.5 eV and higher photon energies, all features are due to σ^* resonances. Apart from a general difference in peak intensities, the peaks of the film spectrum coincide well with those of the gas-phase and of the theoretical spectra. The features at 285 and 289 eV and the high photon energy region are in very good agreement, but the peak at 287.5 eV is more intense in the gas phase. The asymmetric tail on the higher photon energy side of the main peak, due to the contribution of the C_β atoms is also present in the film, though it is less resolved. The other peaks are, in general, less intense in the film with respect to the gas phase and to the calculations for the isolated molecule. This can be ascribed to the overall broadening already observed for PES results considering also the significant lower resolution of the NEXAFS spectra of the film with respect to the gas phase results. The resemblance of gas phase, theoretical and film NEXAFS spectra, as already seen for the VB results, confirms the molecular character of the adsorbed thick film as already observed for other molecular films[65].

In order to have an estimation of the molecular arrangement we performed NEXAFS measurements at different orientations of the sample with respect to the incident light, for all the obtained coverages (high, intermediate and low). In Fig. 3.14a) we display the NEXAFS data for the high coverage film of Fig. 3.13 in the two geometries of NE and IPL. These spectra show that in the thicker film the molecules arrange themselves according to a preferential direction. In fact, the first two π^* resonances at about 285.0 eV and 287.0 eV are enhanced in IPL, indicating, as already anticipated by the Val results, molecules preferentially standing on the surface of the substrate. Subsequently, we studied the molecular arrangement as a function of the film thickness on a low coverage film (7 Å thick) and on an intermediate coverage film (30 Å thick), at normal (IPL)

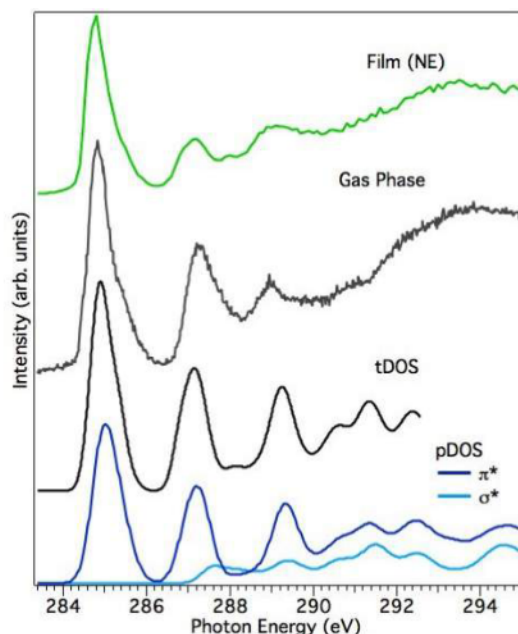


Figure 3.13: Biphenylene thick film NEXAFS spectrum in the NE geometry (see text). The film spectrum is compared to gas phase and DFT calculations showing the tDOS and pDOS for π^* and σ^* contributions.

and grazing incidence (OPL) ($\theta=20^\circ$) geometries².

For low coverage (Fig. 3.14b)) a strong polarization dependence is observed, with an opposite trend with respect to the high coverage, indicating a tendency for the molecules to adsorb lying on the surface. In order to estimate the molecular orientations more precisely, we used the formula:

$$I_{\pi^*} = A(\cos^2\theta\cos^2\alpha + \frac{1}{2}\sin^2\theta\sin^2\alpha) \quad (3.1)$$

describing the intensity of the first π^* resonance as a function of the angle θ for a substrate with a threefold symmetry, such as Cu(111). For this kind of symmetry, there is no dependence from the surface azimuthal direction, thus the only unknown parameters are the angle α that the π orbitals form with the normal to the surface \vec{n} and the multiplying constant A. Solving the system with the values of I_{π^*} and θ obtained from the high coverage and low coverage experiments, we determine $\alpha = 66^\circ \pm 5^\circ$ and $20^\circ \pm 5^\circ$, respectively (see the schematic representations of the molecular arrangement in Fig. 3.14). The errors reported take into account also the uncertainties introduced by the angle reading and the background nor-

²For an explanation of the experimental geometry we refer to Section 2.0.4

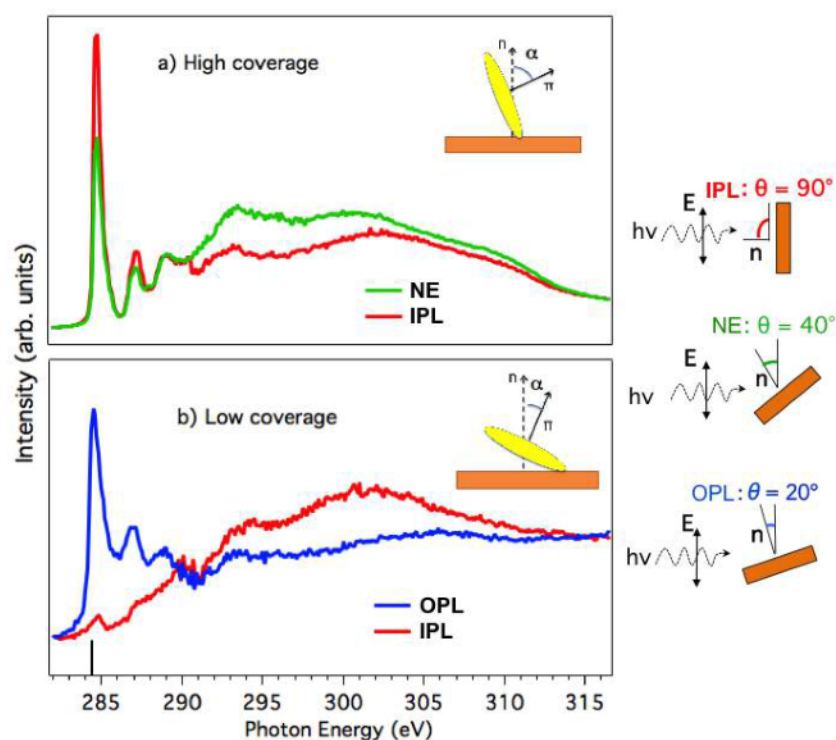


Figure 3.14: Polarization dependent NEXAFS for two film thicknesses. a) High coverage film b) low coverage film. Each film was measured for different values of θ , the angle between the polarization vector \vec{E} of the incident radiation and the surface normal of the Cu(111) sample. Three geometries are shown here: $\theta = 90^\circ$ (IPL) and 40° (NE) for high coverage and $\theta = 90^\circ$ (IPL) and 20° (OPL) for low coverage. The vertical bar at 284.5 eV in Fig. 3.14b) indicate the position of the biphenylene C 1s core level peak at low coverage.

malization. Since the angles obtained by NEXAFS might be due to the superposition of two or more orientations, we rather refer to the molecular orientation α as the “average angles” of the molecule.

As we can see from Fig. 3.15a), a lack of a preferential molecular orientation seems to characterize the intermediate coverage film since there is no remarkable dependence of the π^* and σ^* resonances on \vec{E} direction, in the two geometries of IPL and OPL. We performed an annealing on this film, heating the substrate from the LN2 temperature to 223 K for about 5 minutes and then cooling it down again to 90 K. We estimated that this treatment leaves only a monolayer of biphenylene on the surface. From the NEXAFS spectra acquired thereafter (Fig. 3.15b), we can observe great similarity with the low coverage spectra (Fig. 3.14b). Applying equation 3.1 to this system, we obtain $\alpha = 26^\circ \pm 5^\circ$, which is very similar to the

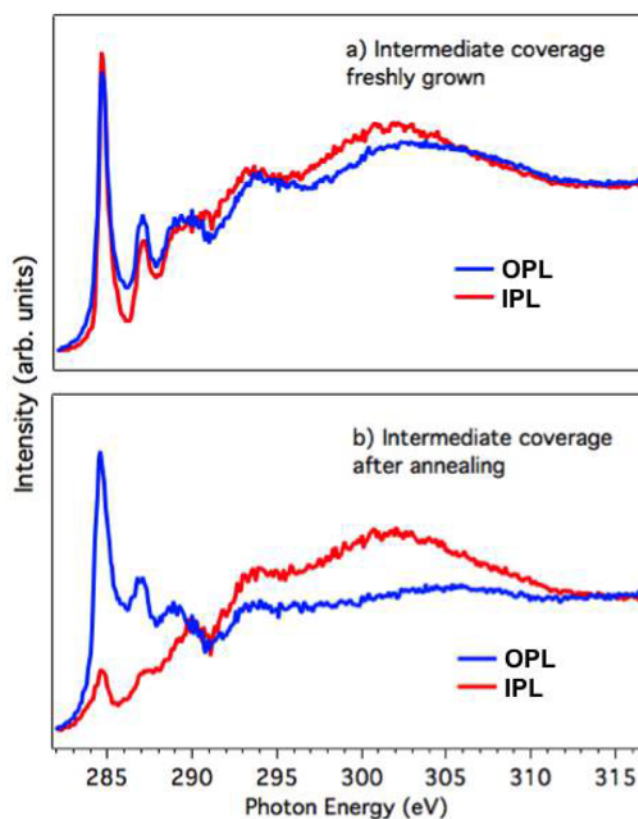


Figure 3.15: NEXAFS spectrum on a freshly grown film of biphenylene for an intermediate coverage; b) NEXAFS spectrum after the annealing. The acquisition geometries are OPL and IPL, already used for the low coverage film. The line shapes are very similar to the spectrum at low coverage and the polarization dependence is the same.

average angle measured for the low coverage.

Thus, from our analysis we find out that depending on the thickness of the biphenylene film, the molecules are ordered or randomly oriented, i.e. the molecules show a preferential orientation for low and high coverage, but not for intermediate coverage. Moreover, for low coverage, the molecules mostly lie flat on the surface while, for very high coverage, the molecules mainly stand on the surface. From these considerations we can say that, for low coverage, molecule-substrate interactions play a sufficiently important role to determine an ordered arrangement of the molecules on the surface. For high coverage, instead, the molecule-molecule interactions get more importance.

To the best of our knowledge, this is the first characterization of biphenylene deposited on a surface. The analysis of core and valence

occupied and unoccupied levels revealed that the adsorbed biphenylene film is characterized by important intermolecular interactions, as can be deduced from the overall broadening of the spectral features when compared with the results of the gas phase measurements and of the single molecule DFT calculations. However, the overall agreement among thick film, gas phase and theoretical spectra indicates that biphenylene preserve, in films, a molecular character. NEXAFS measurements performed on biphenylene adsorbed at different coverage, show that the molecules choose an ordered arrangement for very thin and for very thick films. The molecules vary their orientation from lying to standing on the surface for increasing coverage. We can conclude that the interaction between biphenylene and Cu(111) substrate is sufficiently important to determine an asymmetric line shape in C 1s peak and a flat molecular arrangement in the thinnest biphenylene film. However, supported both by the low temperature needed for adsorption and also for the similarity between the NEXAFS spectra for low coverage and gas phase, (a part the dichroism due to the ordering of the molecules in the monolayer) the molecules-surface interaction is estimated to be rather weak.

3.3 Vibronic contribution in pyridines

3.3.1 Theoretical aspects

Reference [66] starts as: “*The near edge x-ray absorption fine structure (NEXAFS) spectrum of pyridine (C_5H_5N) is not yet fully understood*”. In that work Kolczewski and coworkers could explain the splitting of the first π^* resonance in the carbon 1s ionization threshold and stressed the importance of the vibrational structure by including them in the calculations. This is the problem that we already faced in this thesis work. In the previous paragraphs we did observe, in fact, some discrepancies between experimental data and their theoretical simulations which can be attributed to vibrational effects: see Sections 3.1.3 and 3.2.2.

Vibrational fine structures in NEXAFS were identified long time ago, with the first studies of ethylene by NEXAFS in TEY mode [67] and EELS [68]. In all more common approaches to simulate NEXAFS (static-exchange [69] Density Functional Theory (DFT) [29] and Time Dependent DFT (TD-DFT) [70] the most direct way to obtain the spectral intensities is to consider only the electronic contribution, by calculating the electric transition dipole moments between the initial and the final bound state. However, with the

concomitant continuous improvement in energy resolution of synchrotron sources and analyzers, now it is possible to study the vibrational features present in NEXAFS spectra even in more detail.

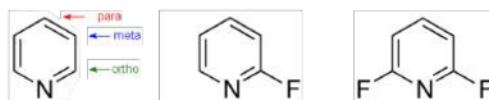


Figure 3.16: Molecules of pyridine, 2-fluoropyridine and 2,6-difluoropyridine. The ortho, meta and para carbons are also marked.

Here we present the results of a combined experimental and theoretical analysis of the N1s and C *K*-edge NEXAFS spectra of pyridine, 2-fluoropyridine and 2,6-difluoropyridine (shown in Fig. 3.16). The electronic spectra have been considered at various levels of theory, namely, by the Transition Potential DFT (DFT-TP) scheme, where the relaxation of the core orbitals is obtained by reducing their occupation by half of an electron, and by the Time Dependent DFT approach with a restricted excitation window. For these systems, vibrational effects have been found crucial for a correct description of the C *K* spectra involving strong intensity redistribution, at variance with the N *K*-edge, where vertical electronic transitions broadened by simple Gaussian distributions are usually sufficient.

Structures of all systems are first optimized at the DFT level. Secondly, the NEXAFS spectra are calculated at the spin-restricted DFT level. The core hole at each non-equivalent center is modeled by the Transition Potential (DFT-TP, Sec. 2.0.5) approximation, reducing the occupation number of the core orbital by half an electron. The Time Dependent TD-DFT spectra have been simulated using the so-called restricted excitation window formulation (REW-TD-DFT, a description of the method can be found in Ref. [70]), which is well suited for the calculation of the excited states involved in NEXAFS spectroscopy. Finally, the vibrationally resolved spectra have been computed within the general theoretical framework (more details can be found in Refs. [71, 72]) based on a time-independent (TI) formulation.

3.3.2 Experimental and theoretical results

The experimental spectra of 2-fluoropyridine and 2,6-difluoropyridine at both C and N *K*-edges are reported in Fig. 3.17. The NEXAFS spectra at C and N *K*-edges were acquired by measuring the ion yield with a channel electron multiplier placed close to the ioniza-

tion region. Photon resolution was better than 70 meV at C and N K-edges.

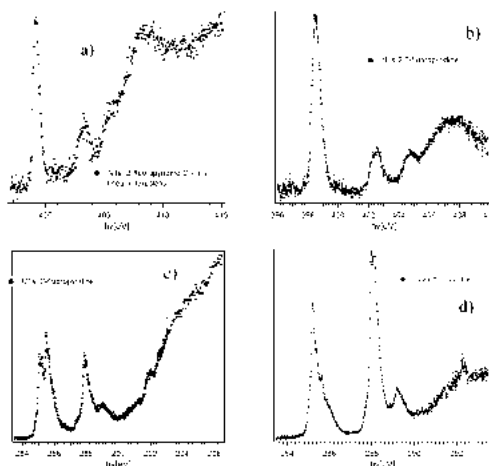


Figure 3.17: Experimental NEXAFS: a) N 1s 2- fluoropyridine, b) N 1s 2,6-difluoropyridine, c) C 1s 2-fluoropyridine, d) C 1s 2,6-difluoropyridine.

Pyridine is an important system, since it is the simplest aromatic heterocyclic compound; moreover, its fluorinated derivatives are interesting because they include at the same time strong electronic effects related to the aromatic stabilization as well as inductive effects generated by both electronegative N and F atoms. For this reason, this series represents a challenge for theory, since it is required that all these effects are properly described in a balanced way by the adopted formalism. For pyridine in the gas phase, also previous calculations on the vibrational fine structure have been reported. Since previous vibrational fine structure calculations have been reported for pyridine in the gas phase, it was elected by us as case study to test the simulation procedure developed by our collaborators at the University of Trieste and at the University of Pisa.

Finally it is worth noting that the NEXAFS has been also employed to study not only free pyridine in the gas phase [66, 73] but also when adsorbed over the silicon (110) surface, both experimentally [16] and theoretically [74].

A. N1s electronic spectra

In Fig. 3.18, the experimental N1s NEXAFS spectra of pyridine [66] and of its two F-derivatives (this thesis) measured in the gas phase are compared with the spectra computed by the DFT-TP method. The experimental profiles have been shifted on the

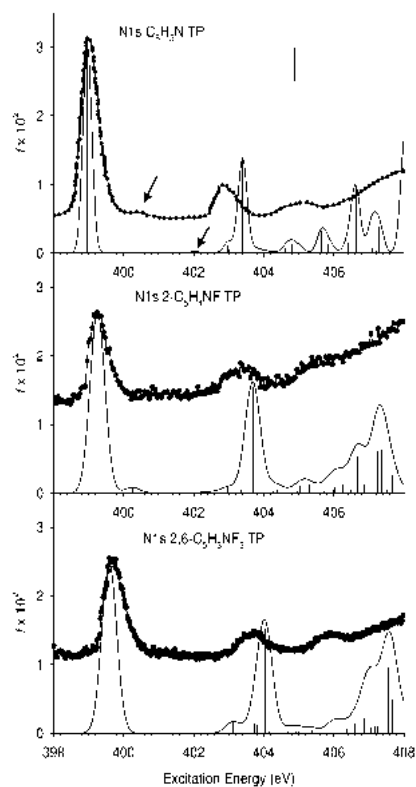


Figure 3.18: N 1s NEXAFS spectra of pyridine (upper panel), 2-fluoropyridine (central panel) and 2,6-difluoropyridine (lower panel) : experimental data (circles) and calculated DFT-TP results (solid line and vertical bars). Experimental energy scale has been shifted in order to match the first calculated N1s \rightarrow 1 π^* peak.

energy scale in order to match the first intense peak ascribed to the N1s \rightarrow π^* transition. The theoretical electronic spectra correctly describe the main features of the experiment and the energy separation among the peaks. The reproduction of both the intensity pattern and the band-shape indicates negligible vibronic effects for these transitions, as confirmed by the calculated vibronic spectra of the N1s excitations of pyridine discussed further in this Section. We can first interpret the N1s spectra on the basis of the electronic DFT-TP results.

The first and strongest peak of the pyridine spectrum (upper panel of Fig. 3.18) is assigned to the N1s \rightarrow $\pi^*(3b_1)$ transition (at 399.0 eV). The asymmetric line shape of this peak in the experiment is due to an unresolved vibrational fine structure, and in fact this asymmetry is recovered by including vibronic effects in the calculation, as discussed in the next paragraph and shown in Fig. 3.19). A

very weak bump (marked with a red arrow) appears in the experiment at the higher energy side of the main peak, with an energy separation of about 1.4 eV, which is missing in the calculated spectrum. This small structure has been attributed to the N1s transition to the $2\pi^*$ orbital ($1a_2$), which is dipole-forbidden in C_{2v} symmetry but could obtain intensity in the experiment through vibronic coupling effects [66]. We will comment on this hypothesis in the next paragraph, where the N1s vibrational structure is discussed.

A very weak transition is calculated at 402.1 eV (blue arrow) and assigned to an antibonding $\sigma^*(\text{C-H})$ orbital with a strong admixture of Rydberg character, in agreement with previous calculations [66, 73]. It corresponds to a weak peak observed in the experiment just before the second well-defined experimental peak (around 402.6 eV on the energy scale of Fig. 3.18). In this energy region the calculations predict a structure which is contributed by weak transitions (around 403.0 eV) of essentially Rydberg character, followed by the more intense N1s $\rightarrow 3\pi^*$ transition (at 403.4 eV) characterized by an admixture of valence and Rydberg character. The region around the ionization threshold contains several weak transitions of mixed Rydberg and valence excitations.

The N1s spectra of the 2-fluoropyridine and 2,6-difluoropyridine reproduce the pattern of the pyridine spectrum. We observe a slight increase of the calculated excitation energies on going from pyridine to 2,6-difluoropyridine, due to the withdrawal of the valence electron charge induced by the fluorine atoms; the energy separation among the spectral features remains however constant in the three spectra. This energy shift is confirmed by the experimental observation.

The main peak is assigned to the N1s $\rightarrow \pi^*$ transition in both molecules. In the case of 2-fluoropyridine (C_s symmetry), the N1s $\rightarrow 2\pi^*$ transition is dipole-allowed and appears in the calculated spectrum at 400.2 eV. It becomes again forbidden in 2,6-difluoropyridine and is therefore not present in the spectrum. The peaks around 404 eV are mainly contributed by the N1s $\rightarrow 3\pi^*$ transition in both 2-fluoropyridine and 2,6-difluoropyridine spectra while the lower energy shoulder (at 403.0 eV in 2-fluoropyridine and 403.1 in 2,6-difluoropyridine) is assigned to a transition into an antibonding $\sigma^*(\text{C-H})$ orbital with a strong admixture of Rydberg character.

B. N1s vibrational structure

In Fig. 3.19, the experimental spectrum for the N1s excitation of pyridine is reported together with the calculations including the vibronic spectrum. Only the five excited states, corresponding to

the highest oscillator strength in the energy range between 386 and 394 eV, have been included in the computation. By comparing the computed bandshape with the results obtained at the TD-DFT level using the best functional-basis set [75] it turns out that the inclusion of vibronic effects does not change significantly the computed spectrum. In fact, both the shape and the relative intensity of the two most intense bands of the spectrum, located at about 386 and 392 eV, are nearly unchanged with respect to the results.

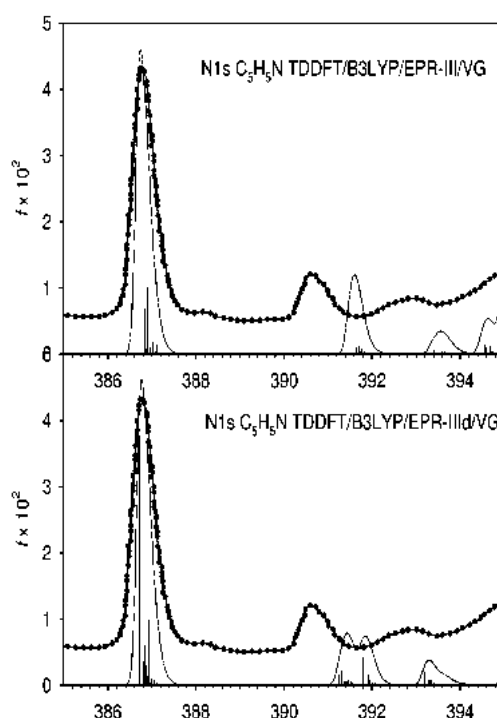


Figure 3.19: N 1s NEXAFS spectra of pyridine: experimental and calculated results including vibronic effects (solid line and vertical bars). Theoretical method/basis are indicated in the inset (from Ref [75]).

The calculated intensities for the vibronic transitions of $N1s \rightarrow 2\pi^*$ are much weaker (about three orders of magnitude) with respect to those of the $N1s \rightarrow 1\pi^*$ transition and are not able to change the shape of the main band when they are summed up to the vibronic transitions of the first peak. Therefore, we are led to conclude that the vibronic coupling is not able to increase appreciably the intensity of the dipole forbidden $N1s \rightarrow 2\pi^*$ transition in pyridine, which we expect not to be detectable. As a consequence, the weak structure reported in the experiment of Ref. [66] assigned to $N1s \rightarrow 2\pi^*$ is probably an artifact of the noisy background. This observation is

further supported by a more recent experiment [73] which does not show any feature related to the $N1s \rightarrow 2\pi^*$ transition. Moreover, the energy resolution for $N1s$ NEXAFS is 90 meV in Ref. [73], which is better than 150 meV reported in Ref. [66].

C. C K electronic spectra

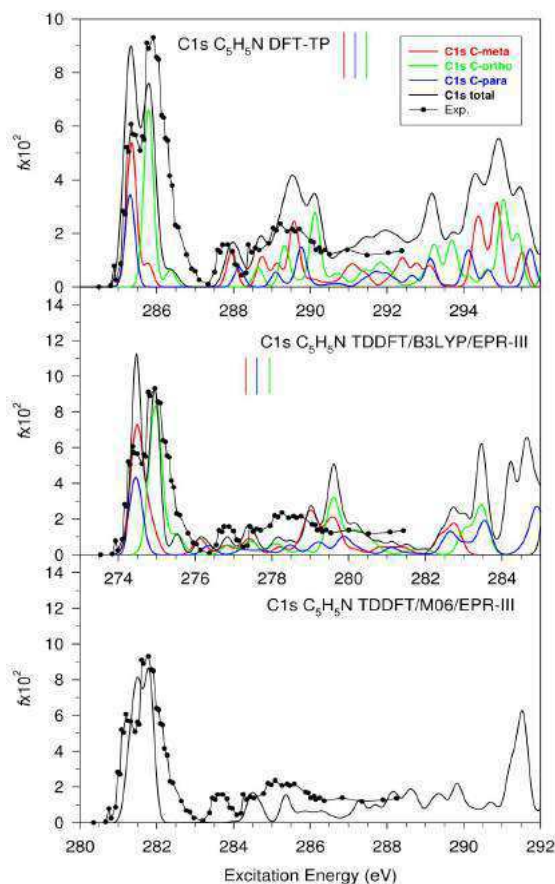


Figure 3.20: C K NEXAFS spectra of pyridine: experimental data (circles) and calculated results (solid line). Theoretical method/basis are indicated in the inset and partial contributions in the legend. Experimental energy scale has been shifted in order to match the first calculated $C1s \rightarrow 1\pi^*$ peak.

In Fig. 3.20 the C K excitation spectrum of pyridine calculated with different methods is compared with the experiment, the latter having been shifted on the energy scale in order to match the first $C1s \rightarrow 1\pi^*$ transition of the calculation [75].

Starting with the DFT-TP scheme (upper panel), the calculated total C K spectrum is characterized by a sharp double-peak band around 286 eV followed by weaker features starting around 288 eV

and reaching a maximum around 290 eV. The theory reproduces only qualitatively the experiment, in fact the relative intensity of the double-peak feature at 286 eV (in the experiment the first peak is less intense than the second one) is reversed in the calculation. The double peak-structure of the first band can be rationalized taking into account the different contributions to the total absorption. In fact, the band is ascribed to the three different $C1s \rightarrow LUMO$ ($1\pi^*$) transitions; therefore the relative excitation energies reflect the relative energy of the core orbitals: the ortho $C1s$ feels the proximity of the electronegative N atom, which depletes electron density, then the ortho $C1s$ orbital is less shielded and concomitantly more bounded to the nucleus and therefore a larger excitation energy is predicted for the ortho $C1s$. Such an effect, which corresponds to an energy difference of 0.5 eV, is in remarkable agreement with the experiment.

It is worth noting that in the ortho and meta partial profiles a weak secondary maximum is observed, at 286.3 eV and 285.8 eV, respectively, those transitions being ascribable to excitations to the $2\pi^*$ orbital. Such a feature is absent in the para partial profile because $2\pi^*$ has a nodal plane orthogonal to the molecular plane passing through the N and para C atoms; therefore its dipole transition moment vanishes due to symmetry constraints. The $1\pi^*$ and $2\pi^*$ orbitals are derived from the $1\pi^*$ degenerate orbital of benzene (e_{2u} in D_{6h}), which, due to symmetry lowering (to C_{2v}) split to b_1 ($1\pi^*$) and a_2 ($2\pi^*$) orbitals in pyridine.

The highest valence virtual $3\pi^*$ orbital (corresponding to the b_{2g} one of benzene) lies much higher in energy and contributes to the transitions around 290 eV. This high-energy region, however, is rather complicated, since it encompasses transitions to many final virtual orbitals, including $\sigma^*(C-H)$ antibonding orbitals as well as diffuse Rydberg states. Although this spectral region is extremely congested, preventing a detailed assignment of all the calculated spectral features, the calculation is in good agreement with the experiment. In summary, a comparison between the DFT-TP electronic calculations and experiment is fully satisfactory as far as the relative excitation energies are concerned, but if the intensity distribution is considered, an inversion is found for the first band at 286 eV. This disagreement is very intriguing, since it might be ascribed to different causes, like a problem in the description of the spectrum caused by a deficiency in the electronic structure or, more likely, the neglect of vibrational effects in this computational model.

D. C K vibrational structure

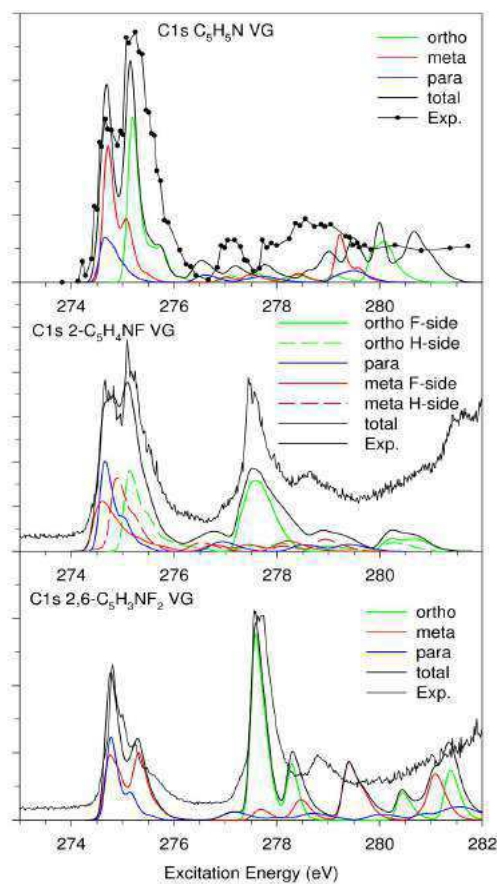


Figure 3.21: C 1s NEXAFS spectra of pyridine (upper panel), 2-fluoropyridine (central panel) and 2,6-difluoropyridine (lower panel): experimental data (circles) and calculated results (solid line) including vibronic coupling at the VG level. Theoretical method/basis are indicated in inset and partial contributions in the legend. Experimental energy scale has been shifted in order to match the first calculated $C1s \rightarrow 1\pi^*$ peak.

In the upper panel of Fig. 3.21 the vibronic spectrum calculated at the VG-FC level for C K excitations in pyridine in the range between 274 and 281 eV is shown together with the experimental results. The 28 excited states corresponding to the largest oscillator strength (11 associated with excitations from the 1s C ortho orbitals, 11 from the 1s C meta and 7 from the 1s C para) have been included in the computation. In this case, remarkable differences are present with respect to the theoretical results both at the DFT-TP level and at the TD-DFT level, reported in Fig. 3.20. Let us consider, for example, the double-peak structure present in the low energy range of the spectrum (see the upper panel of Fig. 3.20 at about 286 eV). As already remarked, this pattern is poorly reproduced at the

vertical energy level, since the intensity of the first peak is expected to be larger than that of the second one. However, the inclusion of vibronic effects modifies the relative intensities of the two peaks, and a better match with the experimental results is reached.

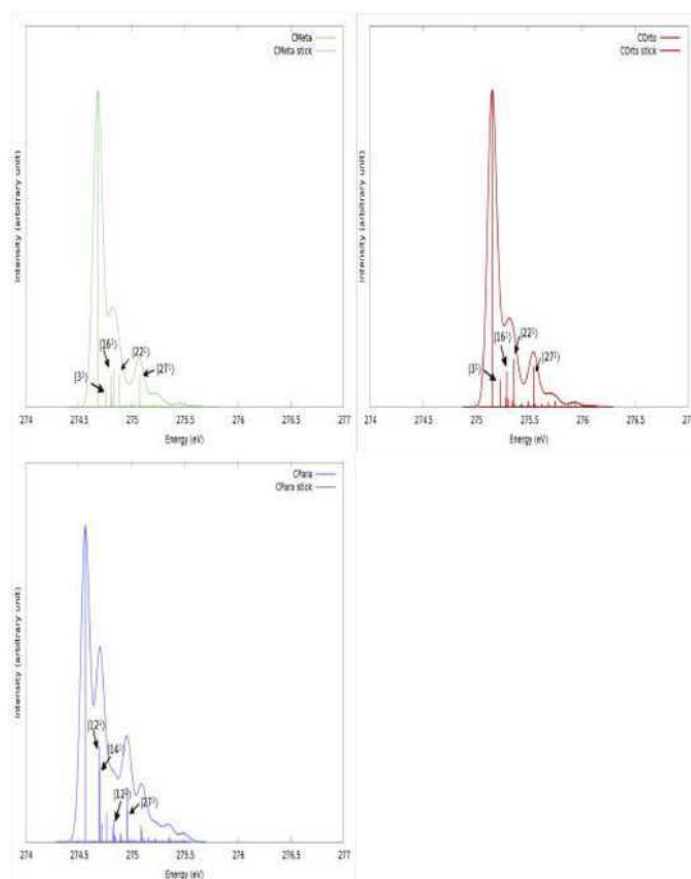


Figure 3.22: Vibronic C 1s NEXAFS spectra of pyridine for excitations from the meta (green), orto (red) and para (blue) carbon atoms. The VG—FC model has been used to simulate vibronic effects. Gaussian distribution functions with HWHM of 0.05 eV has been used to simulate broadening effects. The assignment of the most intense transition is also reported in the figure.

In order to analyze this effect in deeper detail, the vibronic NEXAFS spectra for excitations from the C1s orbital of each non-equivalent C atom to the $1\pi^*$ virtual orbital are shown separately in Fig. 3.22. Even if the vibronic band-shapes are nearly equivalent for the excitations starting from the C1s orbitals of the ortho and meta atoms, a larger number of intense vibronic transitions are present for the spectrum associated with the para C1s $\rightarrow 1\pi^*$ excitation. For the para the transition between the vibrational ground states is less in-

tense with respect to the other ones and the vibronic broadening is significantly larger. Due to polarization effects, the band associated with the para $C1s \rightarrow 1\pi^*$ transition lies in the low-energy region of the double peak signal, and therefore the relative intensity of the first sub-peak decreases, giving a better match with the experimental results.

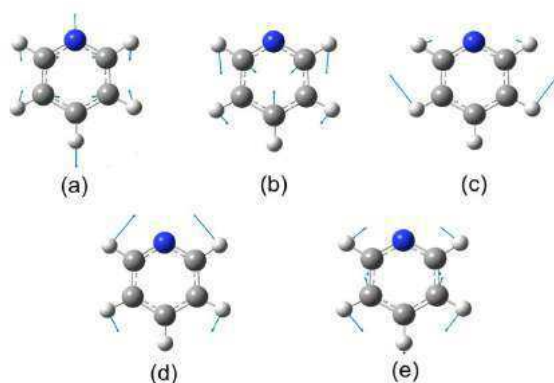


Figure 3.23: Graphical representation of the normal modes of pyridine, giving the most intense vibronic transitions in the calculated C 1s NEXAFS spectrum.

In Fig. 3.23 a graphical representation of the normal modes giving intense vibronic transitions is reported. It is noteworthy that the active normal modes are associated with in-plane deformations of the ring, since the extrapolated equilibrium geometry of the excited states associated with bright transitions is, in every case, planar, and therefore vibronic transitions involving out- of-plane deformations are inactive.

For the sake of completeness, we have investigated also temperature effects. In fact, even if all the previous computations have been performed at 0 K, therefore by assuming that the starting level is the vibrational ground state of the initial state PES, the experimental spectra have been recorded at 298 K. Temperature effects have been included in the vibronic simulations within the time-independent formalism (TI) following the procedure outlined in Ref. [76] and extending the Franck-Condon (FC) approximation with the more general case of the Herzberg-Teller (HT) model³. In the computation all the vibrational levels of the ground electronic state were included with a Boltzmann population larger than 0.1. The results sketched in the upper panel of Fig. 3.24 show that, as

³In the scenario of combined electronic and vibrational transitions, Herzberg and Teller model introduces for the electronic transitions a dependence on the nuclear coordinate associated with the vibration. In the Franck-Condon approximation one assumes that there is no such dependence.

expected for such rigid systems, the spectra calculated at 0 K and 298 K are nearly superimposable, and therefore temperature effects do not affect significantly the computed band-shape.

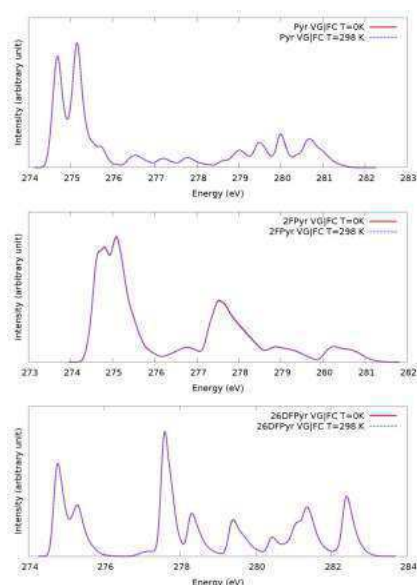


Figure 3.24: Vibronic NEXAFS spectra of pyridine (upper panel), 2-fluoropyridine (middle panel) and 2,6-difluoropyridine (lower panel) for excitations from the C 1s orbitals. Broadening effects have been simulated using Gaussian functions with HWHM of 0.1 eV

The vibronic spectra, calculated at the VG-FC level, for the C1s NEXAFS spectrum of 2-fluoropyridine are reported in the middle panel of Fig. 3.21, together with the shifted experimental spectrum. In this case, the 27 excited states associated with the largest value of the oscillator strength have been included in the simulation. As for pyridine, also in this case the low-energy region of the experimental spectrum is characterized by a double-peak structure, where the first peak is less intense than the second one. As shown in Fig. 3.21, this spectral pattern is well reproduced by including vibronic effects.

As already done previously for pyridine, in Fig. 3.25 the vibronic spectra for the C1s \rightarrow $1\pi^*$ excitations for each non-equivalent C atom are reported separately. Let us recall that the carbon directly bonded to the fluorine atom gives a signal at significantly higher energy due to polarization effects, and therefore it is not included in the Figure. Comparison of those spectra shows that the vibronic band-shape is similar for three of them, except for the excitation from the C meta atom on the same side of the F, giving a significantly broader spectrum. More in detail, for the first three spectra,

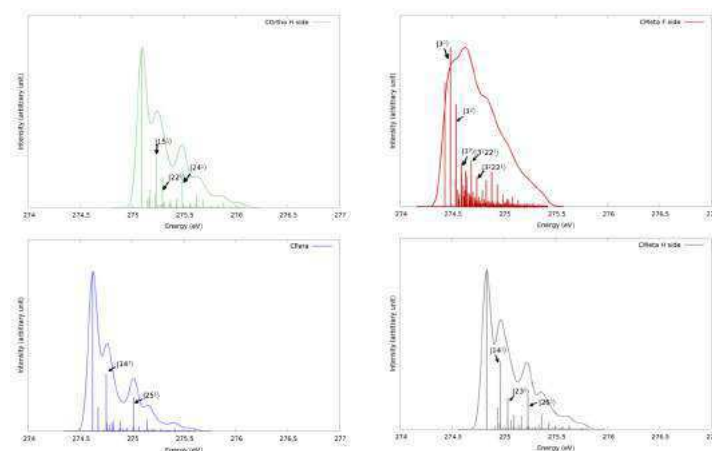


Figure 3.25: Vibronic C 1s NEXAFS spectra of 2-fluoropyridine for excitations from the C orto H side (green), para (blue) meta F side (red) and meta H side (grey) carbon atoms. Gaussian distribution functions with HWHM of 0.05 eV have been used to simulate broadening effects. The assignment of the most intense transition is also reported in the figure.

only few vibronic transitions (whose assignment is reported in the spectrum) have a noticeable intensity, and therefore the broadening of the spectrum is limited. On the other hand, for the fourth excitation, a larger number of intense vibronic peaks can be identified, and also several overtones and combination bands are active and therefore the spectrum is significantly broader. The spectrum associated with the excitation from the 1s orbital of the C meta on the F side to the $1\pi^*$ orbital contributes to the low energy sub-peak of the double-peak structure present in the experimental spectrum; the inclusion of vibronic effects decreases the relative intensity of this peak, therefore giving a better reproduction of the experimental results.

Also for 2-fluoropyridinepyridine, a graphical representation of the normal modes, giving the largest vibronic transitions, is reported in Fig. 3.26. In analogy with pyridine, also in this case the extrapolated equilibrium geometries of all excited electronic states are planar, and therefore only in-plane normal modes are active. Also in this case temperature effects have been investigated and, as shown in the middle panel of Fig. 3.24, their inclusion does not modify the overall band-shape.

The NEXAFS vibronic spectrum for 2,6- difluoropyridine simulated at the VG-FC level is reported in the lower panel of Fig. 3.21. The 34 excited states associated with the largest oscillator strength have been included in the simulation (10 for excitations from the C

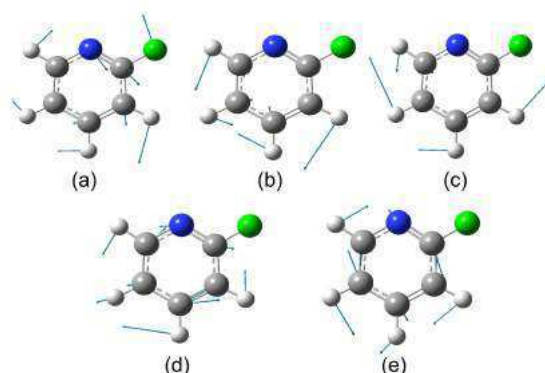


Figure 3.26: Graphical representation of the normal modes of 2-fluoropyridine giving the most intense vibronic transitions in the calculated C 1s NEXAFS spectrum.

ortho atom, 14 from the C meta one and 10 from the C para). The inclusion of vibronic effects does not affect significantly the simulated band-shape. In fact, the shapes of the two most intense peaks of the experimental spectrum (at about 275 and 278 eV) are nearly unchanged with respect to their VE counterparts, even if the intensity of the first band decreases slightly. A more relevant difference is present in the energy region above 279 eV, where the inclusion of vibronic effects leads to an overall intensity decrease for all the bands, thus giving a better matching with the experimental results. As shown in the lower panel of Fig. 3.24, also for this system temperature effects are negligible.

Chapter 4

Transition metal macrocyclic compounds

In this chapter the investigation of phthalocyanines, a widely studied class of macrocyclic compound, will be exposed. Macrocyclic compounds are systems at a higher complexity than the ones studied in the previous chapter, which typically contain rings of 5 or 6 carbon atoms, eventually substituted by nitrogen or sulphur atoms, while in the case of phthalocyanines we have 32 carbon and 8 nitrogen atoms.

More into detail, phthalocyanine (Pc or H_2Pc , see Fig. 4.1 (a)) is a planar molecule formed of four isoindole units linked in a circular arrangement through nitrogen atoms with two hydrogen atoms and has chemical formula $H_2C_{32}N_8H_{16}$. H_2Pc structure represents a very interesting macrocyclic ligand, that is a macrocycle that has an internal cavity with at least three donor atoms, that act as binding sites. This type of molecules are excellent receptors for both anionic species that for cationic species, and are the subject of research for molecular design.

To the cavity of this larger - but more symmetric - organic structure, one can substitute the two central hydrogens with a transition metal atom, like a $3d$ or a lanthanide (MePc, Fig. 4.1 (b)). These metals are characterized by a rather high number of orbitals with quantic number and symmetry quite different from C and N, that determine very different and varied properties.

Among the several macrocyclic ligands that are present in nature, the molecular structure of phthalocyanine is similar to that of (metal-free or non-metal-free) porphyrin, which is a core skeleton for hemoglobin and chlorophyll molecules. For this reason the compounds of phthalocyanine and metals have attracted a lot of attention as models of important biologically systems. Moreover ph-

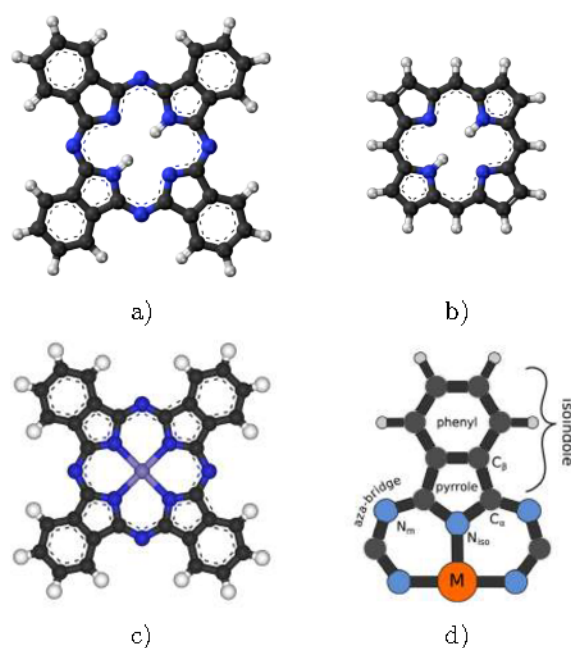


Figure 4.1: Sketch of H₂Pc (a) and porphyrin (b). MePc is sketched in (c) together with a fragment of its molecular structure (d) displaying the notations used.

thalocyanines have good characteristics, such as high thermal and chemical stability, making them suitable for implementation into different hybrid systems. Phthalocyanine compounds are therefore expected to be applied in many fields, such as medicine (for example, as photosensitizers in photodynamic therapy of cancer), optical communication (in nonlinear optics), and displays (as liquid crystals).

There have been several studies carried out on different monophthalocyanines, whereas much less studies have been performed on double-decker phthalocyanines.

Our focus is on the very outermost part of the valence band which determines the electric and magnetic properties of functional materials. Although widely studied, the electronic structure, and in particular the localization of the metallic orbitals in the VB of 3d metal Pcs is still under debate since both experimental and theoretical investigations have provided ambiguous outcomes so far, see for example Refs. [77, 78, 79, 80]. This is a crucial issue for electronic devices, since the character of the outermost molecular orbitals plays a key role in transport related phenomena [81]: for example a localized 3d metallic HOMO or a less localized molecular orbital distributed over the whole molecule would in principle

be expected to behave differently. DFT can successfully be used to identify the metallic 3d states in the low binding energy region of the valence band of Pc's, in comparison to PES measurements exploiting the photoionization cross sections [79, 80].

In Section 4.1 we report an investigation of the low-energy region of the valence band of H_2Pc compared with those of iron phthalocyanine (FePc) and manganese phthalocyanine (MnPc). We show how the atomic character of the Highest Occupied Molecular Orbital (HOMO) is reflected on the outermost valence band binding energy region. and identify how the central metal atom interacts with the C and N atoms of the molecule, giving rise to different partial and total density of states for these three different Pc molecules. The results of this investigation have been published in **PAPER VIII** and **PAPER IV** [80, 82]. In Sect. 4.2 we study another group of Pcs, called multi-decker phthalocyanines or $MePc_2$, that has two phthalocyanine rings linked together through the metal atom and is a much less studied system than mono-Pcs. In this section we report the study of the competition between molecule-molecule and molecule-substrate interactions in a film deposited on silicon [83, 84].

4.1 The role of the central atom in transition metal phthalocyanines

In this Section we present theoretical and experimental valence band (VB) photoelectron spectroscopy (PES) results of metal-free phthalocyanine (H_2Pc), iron phthalocyanine (FePc) and manganese phthalocyanine (MnPc) films as well as gas phase data. We concentrate on the comparison of the occupied valence density of states of these three phthalocyanines and we relate the observed differences to the different metal atom in the molecular central ring. By selecting proper photon energies in the experiment, we can exploit the photoionization cross sections for the photoemission of electrons from different atomic orbitals. In this way, we can disentangle in the experimental spectra the contributions given by the metallic 3d electrons from the contributions coming from the organic rings.

The comparison of the metal free H_2Pc with FePc and MnPc highlights the different interactions of the divalent central ion with the organic molecular ring. As shown by Grobosch et al.[78], the electronic structure of MnPc differs from the one of other metal Pcs because the HOMO peak in its valence band spectrum is of metallic character. Moreover the 3d electronic states contributing to this VB

Table 4.1: Calculated properties of the S_A , S_B and S_C electronic $3d$ configurations (from Ref. [80]).

Structure	Occupation	HOMO symm.	Orbital type	HOMO-LUMO gap
S_A	$b_{2g}^1 e_g^3 a_{1g}^1 b_{1g}^0$	e_g	d_{zz}, d_{yz}	1.35 eV
S_B	$b_{2g}^2 e_g^2 a_{1g}^1 b_{1g}^0$	b_{2g}	d_{xy}	1.65 eV
S_C	$b_{2g}^1 e_g^2 a_{1g}^2 b_{1g}^0$	a_{1g}	d_{x^2}	1.32 eV

feature are not highly localized but hybridize with the orbitals of the organic rings, giving to this molecule potentially different electronic transport properties [78].

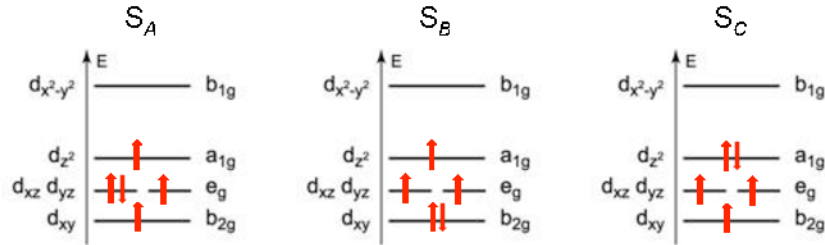


Figure 4.2: Schematic representation of three electronic configurations for Mn $3d$ in MnPc for an intermediate spin state ($S=3/2$).

In general, as recently reported [80] (**PAPER VIII**), the picture of the electronic structure of metal phthalocyanines can be further complicated. MnPc, for example can have different electronic configurations in different types of samples, for example in the gas phase with respect to a thick film. In Fig. 4.2 the three possible electronic configurations (S_A , S_B and S_C) for Mn $3d$ orbitals are schematically shown, and their energies are reported in Table 4.1. While for the thick film a single electronic configuration (S_A) can reproduce the energy distribution of the MnPc metallic states, in the gas phase, at least two (S_A and S_B) are needed. This discrepancy is most likely due to the evaporation conditions, as it will be discussed in the next subsection 4.1.1, and deserves to be investigated more in detail. In this context, not only would a precise knowledge of the exact metal $3d$ electronic configuration of MnPc shed light on the above mentioned effects, but it would also prove crucial in view of spintronics applications by opening the possibility of controlling the orientation of the magnetic anisotropy of the molecule.

In this Section we investigate further these results by studying

the symmetry and the hybridization of the outer molecular orbitals comparing H₂Pc, MnPc and FePc molecular films. We provide a detailed determination of the orbital composition of the HOMO and HOMO-1 of H₂Pc, FePc and MnPc by comparing hybrid DFT calculations to PE spectra for thick molecular films. This gives in addition insight into the different hybridization of the metal states with the organic rings for the two metal phthalocyanines.

4.1.1 Experimental and computational details

This subsection reports details about the measurements of films and gas phase of phthalocyanines and their simulation. The H₂Pc (98% dye content), FePc molecules (90% dye content) and MnPc (95% dye content) molecules were purchased from Sigma-Aldrich. The molecules have been carefully outgassed before all depositions and gas phase measurements. For thick film investigations either a Au(111) single crystal, purchased from Surface Preparation Laboratory (SPL), was used (in case of H₂Pc and FePc) or a gold on mica (in case of MnPc) substrate was used. In case of single crystal substrate, a clean Au(111) surface was obtained by cycles of Ar⁺ ion beam sputtering (900 eV) for 20 minutes, followed by annealing at 550°C for about 2 hours. For the gold/mica (purchased from George Albert Physical Vapor Disposition) substrate, the 300 nm thick layer of gold epitaxially grown on mica, was cleaned by cycles of sputtering and annealing (at 445°) in order to get a clean and reconstructed Au(111) surface. The cleanliness of all the surfaces was checked by the XPS spectra.

The VB photoemission measurements of H₂Pc films on Au(111) ($h\nu=130\text{eV}$) has been performed at beamline I511 at MAX-lab, the national synchrotron radiation facility in Lund, Sweden. The surface endstation of the beamline (at the time of our experiments) consisted of an analysis chamber and a preparation chamber, with base pressures of 8×10^{-11} and 5×10^{-10} mbar, respectively. The analysis chamber was equipped with a Scienta SES200 hemispherical electron analyzer, which could be rotated around the photon beam axis. The molecules have been deposited, in situ, onto the samples in an evaporation chamber under UHV conditions, using a home-built evaporator positioned a few centimeters away from the substrate. The evaporator consisted of a quartz glass tube with a diameter of about 5 mm with a heating tungsten wire twisted around. All measurements were performed with the sample at room temperature (RT), with photon energy of 130 eV and an overall resolution of about 20 meV. The binding energy (BE) scale of the H₂Pc VB spec-

tra was calibrated by measuring the Fermi edge of the Au substrate and/or Au 4f PE spectrum (at 84 eV BE) keeping the experimental settings. FePc and H₂Pc films deposited by thermal evaporation on the Au(111) crystal and film of MnPc on a Au/mica substrate have also been investigated by X-ray photoelectron spectroscopy (XPS) using a monochromatized Al *K*α source (1486.7 eV) and Ultraviolet photoelectron spectroscopy (UPS) with a He discharge lamp (21.2 eV) and a hemispherical analyzer at home laboratory at University of L'Aquila, Italy. For the film thicknesses studied in this work, no signal from the Au 4f peaks was detected by XPS. The binding energy (BE) scale was calibrated considering the Au Fermi edge and the Au 4f core level peaks position. The resolution of the presented valence photoemission spectra (1486.7 eV) is 300 meV.

The PES measurements on vapors have been performed at the Gas Phase beamline at Elettra synchrotron, in Trieste, Italy. The substances were obtained commercially from Sigma Aldrich in the form of crystalline powders with minimum purity of 80%, and were thoroughly purified in vacuum. They were evaporated from a home-built furnace with an effusive nozzle and were checked during purification procedure, comparing them to spectra for thick layers obtained by Kraus et al. [85] for MnPc and by Berkowitz [86] for FePc during the molecular outgassing procedure. Calibration of the energy scale was done introducing He (vertical ionization energy, VIE=24.59 eV) into the ionization chamber and by traces of vaporized water (H₂O, VIE=12.26 eV) found in the system. The photon energies used for valence band measurements were 110 eV for H₂Pc and FePc spectra and 100 eV for MnPc valence band spectrum, all with spectral resolution of about 150 meV. The measurements were started only when the vapor could be safely considered free from impurities (mainly water and phthalonitrile).

The working evaporation temperature for FePc was around 460°C, while for MnPc it was 314°C, avoiding the dissociation observed at higher temperatures. During the whole experiments, the pressure at the ionization region remained constant (ca. 8×10^{-8} mbar). PE spectra have been normalized to the photon flux and to the analyzer transmission function, taking into account the acquisition time. It was not possible to normalize to the sample density, being it not possible to measure its partial pressure. Moreover, the high temperature of vaporization for FePc and its long drifting periods did not allow us to assume an almost constant density of the sample. For MnPc the temperature of evaporation is much lower but it was sufficiently high to condition the measurements mentioned in the previous Section, because it corresponds to an energy of the same

order of magnitude as the energy difference between the different electronic configurations (S_A , S_B and S_C , see 4.1). Therefore great care had to be taken for the gas phase measurement.

Theoretical DFT calculations were performed in the group of Dr. Barbara Brena, at Uppsala University. The geometry for the three molecules was first optimized, then used to determine the electronic structure alongside the contribution of each particular type of atomic orbital (AO) to the valence band molecular orbitals. The bar graphs, corresponding to the discrete molecular energy levels, were broadened using Gaussian functions with a constant full width at half maximum (FWHM) of 0.4 eV (unless stated otherwise) in order to facilitate the comparison with experiment. The atomic origins of particular peaks were obtained by comparing the total DOS to the C $2p$, N $2p$, C $2s$, N $2s$ and metal $3d$ partial contributions. The spectra corresponding to different photon energies (21.2 eV, 130 eV and 1486.7 eV) were obtained by multiplying each partial DOS with its atomic photoionization cross-section at the specific energy [24]. The total spectrum was obtained by summing up the atomic contributions and by adding a Gaussian broadening of variable FWHM. The initial FWHM of 0.2 eV was linearly increased to 2.0 eV in the interval -5.0 eV -15.0 eV and then kept constant.

4.1.2 Experimental results

Density functional theory (DFT) calculations of total and partial DOS of a single H_2Pc molecule together with an experimental valence-band spectrum taken with a photon energy of 130 eV of a thick film of $H_2Pc/Au(111)$ are shown in Fig.4.3. The energy scale of the theoretical calculations has been aligned to the experimental spectrum by a shift of -3.5 eV and conveniently broadened¹ The PE valence spectrum contains several features associated to contributions of different molecular orbitals as disentangled by the partial DOS calculations presented in the figure. The peaks in the experimental spectrum have been labeled from A to H. Peak A is related to the HOMO and is located at 1.5 eV on the binding energy (BE) scale. It has been found, from the previous theoretical studies of a thick film of H_2Pc on conductive glass[87], that the HOMO peak is a π orbital formed by C $2p$ orbitals and the computed HOMO has

¹The simulated spectra corresponding to different photon energies (21.2 eV, 130 eV and 1486.6 eV) were obtained by multiplying each partial DOS with its atomic photoionization cross-section at the specific energy. The total spectrum was obtained by summing up the atomic contributions and by adding a Gaussian broadening of variable FWHM. The initial FWHM of 0.2 eV was linearly increased to 2.0 eV in the interval -5.0 eV -15.0 eV and then kept constant.

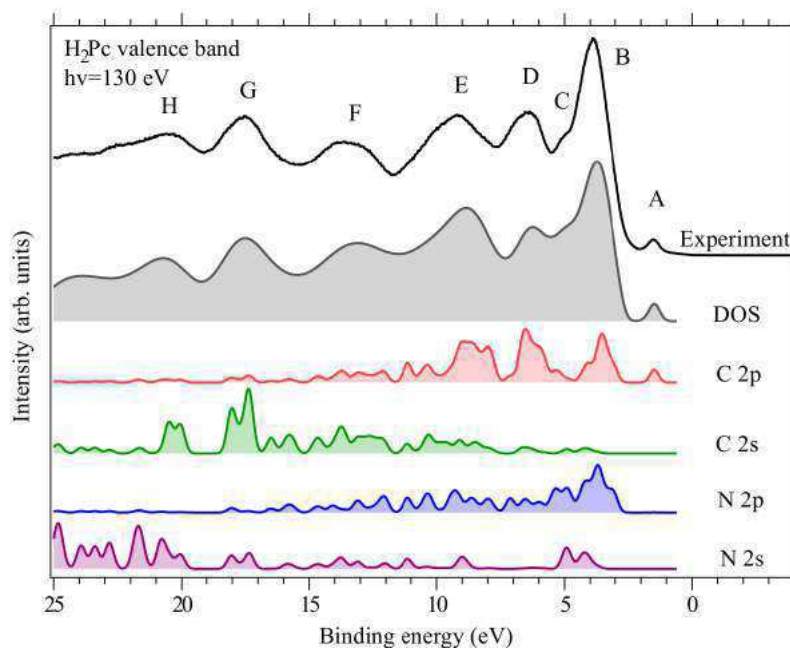


Figure 4.3: Experimental valence-band spectrum taken with a photon energy of 130 eV of a thick film of H₂Pc/Au(111) (black line). The DFT calculations of total and partial DOS of a single H₂ Pc molecule are shown as filled lines.

a_u symmetry. The most pronounced peak B, located at 3.9 eV BE, is due to contribution of p -type orbitals of both carbon and nitrogen atoms and a small contribution of s -type orbitals of nitrogen atoms. Peak C is a low intensity peak mainly formed by contributions of both s and p orbitals of nitrogen atoms together with a small contribution of C $2p$ orbitals. Peak D is mainly related to C $2p$ orbitals, whereas peak E is related to C $2p$ orbitals with minor contributions of C $2s$, N $2s$ and N $2p$ orbitals. Peaks F and G instead are mainly formed out of contributions of C and N s -type orbitals.

In Fig. 4.4 we report a comparison of the valence band spectra of H₂Pc, MnPc and FePc molecular films, taken with photon energies of 1486.7 eV (a) and 21.2 eV (b) shown together with the DFT simulated total DOS (dotted lines). The DFT calculated spectra have been shifted in energy to match the HOMO level of the respective experimental spectrum, giving a shift of -3.2 eV for H₂Pc and -3.6 for both metal Pcs in case of experiments performed with photon energy 1486.7 eV and -3.4 eV for H₂Pc and -3.5 for both metal Pcs in case of experiments performed with photon energy 21.2 eV. In part (c) the molecular orbitals of both HOMO and HOMO-1 features are shown for the three molecules. Due to different cross-section sensitivity,

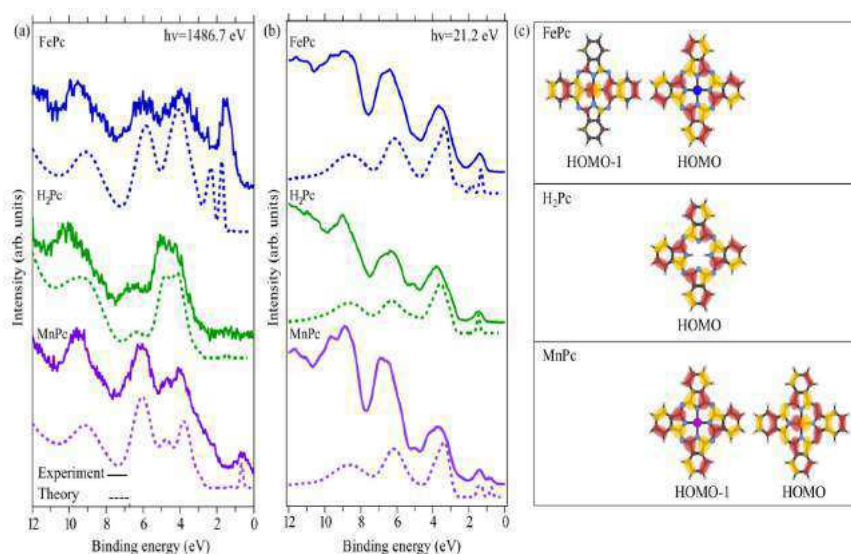


Figure 4.4: Experimental PES results of valence band region for H₂Pc, FePc and MnPc films on Au(111) together with single molecule DFT simulations. Photon energies used are: 1486.7 eV (a, dotted lines) and 21.2 eV (b, dotted lines).

the spectra taken with He I (21.2 eV) photon energy, show mostly contribution of C $2p$ states, whereas the spectra taken with Al $K\alpha$ (1486.7 eV) photon energy enhances the metal atom contributions. The agreement between the experimental and the theoretical results is satisfying in both cases. The better agreement for intensity match between theory and experiment, obtained in case of higher photon energy (part a), can be explained as resulting from less secondary electrons contributing to background signal for experimental spectra, which is quite noticeable in case of experimental results obtained with He I light source.

In a) and b) it is evident that the HOMO and HOMO-1 spectral features are formed from a mix of metal and organic states of the molecule. This is already visible in c) which shows the molecular orbitals (MO) responsible for the peaks in the outermost VB region. The highest occupied molecular orbital (HOMO) of FePc and H₂Pc alongside the HOMO-1 of MnPc, all situated at approximately 1.5 eV BE, have exclusively C $2p$ character. The atoms contributing the most to this orbital are the pyrrole carbons, which are directly bonded to the isoindole nitrogen atoms. The carbons from the benzene rings contribute to some extent, whereas the pyrrole atoms not directly connected to nitrogen atoms, give almost no contribution.

The HOMO of MnPc is situated at lower binding energy (0.5 eV)

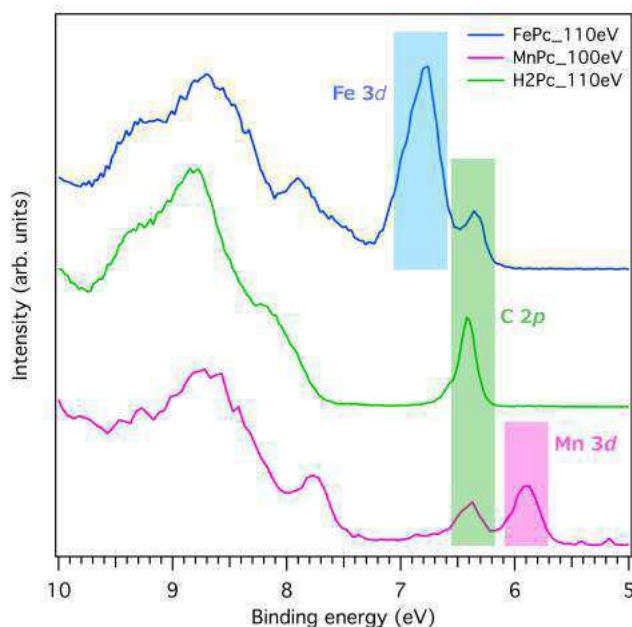


Figure 4.5: Valence band experimental spectrum of gas phase H₂Pc (110 eV), FePc (hv=110 eV) and MnPc (hv=100 eV)

and contains both C $2p$ and Mn $3d$ contributions. In more detail, the HOMO peak of the MnPc VB spectrum is formed from the $2p$ levels of pyrrole carbon atoms (which are directly bound to Mn atom) in combination with the Mn (d_{xz} , d_{yz}) orbitals. Similarly, the FePc HOMO-1 is related to the metal (d_{xz} , d_{yz}) orbitals with a small contribution from C $2p$ levels. The $2p$ character of this MO is much reduced as compared to the MnPc HOMO. The calculated electronic structures of the two metal phthalocyanines are 4E_g (MnPc) and 3E_g (FePc).

The difference between MnPc and FePc implies essentially the presence of one additional electron in FePc alongside an increase by one of the Z number of the central metal. This additional electron occupies in FePc a $3d$ orbital of mainly d_{xy} character, that instead remains empty in MnPc. The Fe d_{xy} orbital has a higher BE with respect to the HOMO-1 of FePc which has a (d_{xz} , d_{yz}) character. Moreover, the first peak with metal $3d$ contributions in FePc (the HOMO-1 peak) is located at higher BE when compared to the same peak in MnPc (HOMO). This is explained by the higher effective charge of the Fe atom as compared to the Mn.

Fig. 4.5 shows a comparison of the HOMO valence energy region of the three phthalocyanines in gas phase. Spectra are taken with photon energy of 110 eV for H₂Pc and FePc and 100 eV for MnPc.

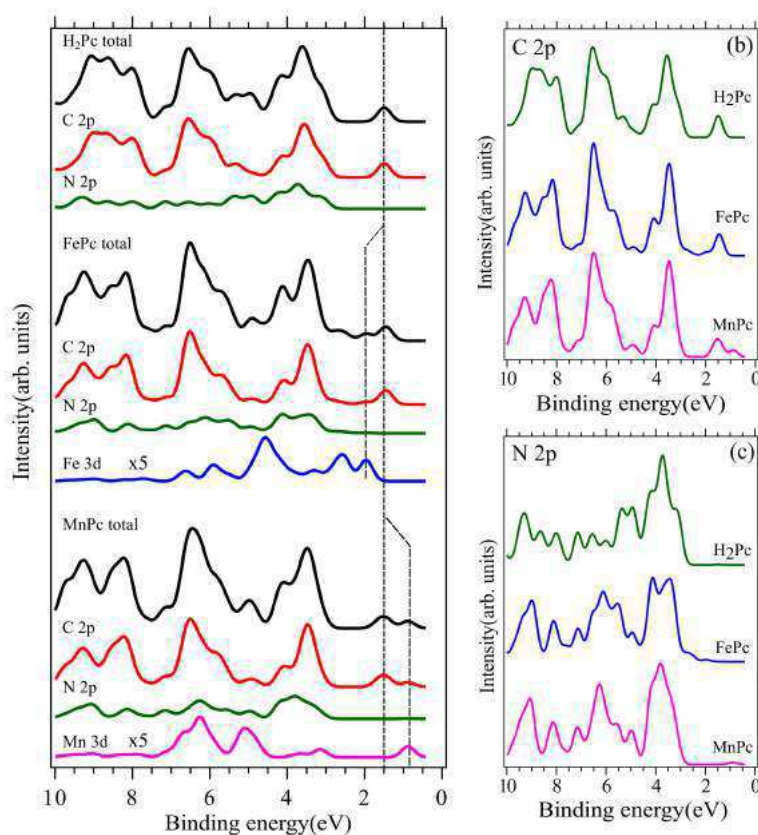


Figure 4.6: DFT calculated atomic partial DOS of H₂Pc, FePc and MnPc (a). The comparison between the C 2*p* and N 2*p* contributions are shown in (b) and (c), respectively. The dashed lines in (a) show the change of HOMO and HOMO-1 peaks for the metal Pcs.

In these spectra the peaks with mostly C 2*p* character, HOMO of FePc and HOMO-1 for MnPc, are at the same BE (6.4 eV). This result is also confirmed by our theoretical calculations showing that the C 2*p* derived peak in the outermost valence is expected at the same BE for all three phthalocyanines. The energy position of the HOMO with Mn 3*d* character⁴ is instead expected at lower BE[77], in very good agreement with what is observed experimentally (at 5.9 eV, $\Delta E_b = 0.5$ eV).

The DFT calculations shown in Fig. 4.6 clarify further the effects of the metallic center on the valence states. The DFT simulations allow disentangling the different atomic orbital contributions to the valence spectrum for the three Pcs. By comparing the simulations of the valence data we can see how the metal atom affects the C 2*p* and N 2*p* contributions to the total DOS of each molecule. We show that

the molecular structure of a metal phthalocyanine originates from the hybridization (orbital combination) between the N (mostly N $2p$) and C (mostly C $2p$) atoms with the central metal atom. Fig. 4.6 (b) and (c) shows the same calculations showing separately the results for C $2p$ and N $2p$ for all Pcs, respectively. The C $2p$ partial DOS for the metal Pcs show a slight change in the spectral shape at the energies of the metal atom contributions, indicating a hybridization of C $2p$ orbitals with the metal atom.

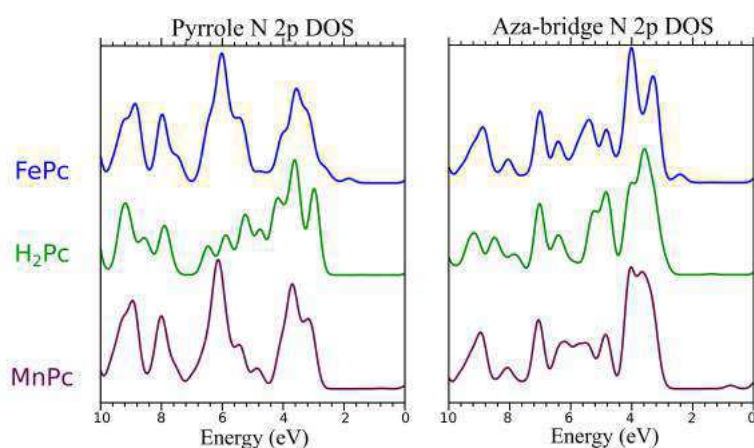


Figure 4.7: DFT calculated atomic partial DOS of H₂Pc, FePc and MnPc (a). The comparison between the C $2p$ and N $2p$ contributions are shown in (b) and (c), respectively. The dashed lines in (a) show the change of HOMO and HOMO-1 peaks for the metal Pcs.

It is mostly seen at lower BE, where the respective metal contribution is stronger - at around 2 eV for FePc and at around 0.8 eV for MnPc. As expected, the orbitals most sensitive to the central metal in the phthalocyanine are the N $2p$ states, more precisely, the pyrrole-type N atoms, which are directly bonded to the metal atom. In fact, a separate analysis of the pyrrole N $2p$ states in comparison to the bridging N $2p$ states shows that the pyrrole nitrogen atoms of the two metal phthalocyanines give rise to a significantly different partial DOS when compared to H₂Pc. For example, in Fig 4.7 the bridging aza-nitrogens in MPcs display $2p$ partial densities of states which are relatively similar to the H₂Pc case. This shows the strong hybridization of the pyrrole N $2p$ with the metallic orbitals and the smaller influence of the metal on the other four nitrogen atoms.

4.2 Grafting of double decker phthalocyanines on Si(100)-2×1

If the center metal has a large radius, as in the case of lanthanide metals, it becomes difficult to incorporate it inside of the Pc ring. Pc ligands are then placed so as to “sandwich” the metal atom, where the metal atom is placed out of the Pc plane. The molecule in this configuration is called as a double-decker Pc molecule. Rare-earth double-decker phthalocyanine molecules have attracted a great attention for their application in organic-based field effect transistors [88, 89] due to their tunable electronic properties. In this study, we focus on double-decker lutetium phthalocyanine (LuPc_2), which is composed of two identical phthalocyanines, rotated by $\theta = 45^\circ$ against each other and bridged via a Lu(III) ion as depicted in Fig. 4.8. The electronic structure of LuPc_2 is characterized by a single semi-occupied molecular orbital (SOMO) between the highest occupied molecular orbital (HOMO) and the lowest unoccupied molecular orbital (LUMO), i.e., in the HOMO-LUMO gap. Therefore, the SOMO electronic state can accommodate or donate its electron, making LuPc_2 a tunable donor or acceptor carrier transporter.

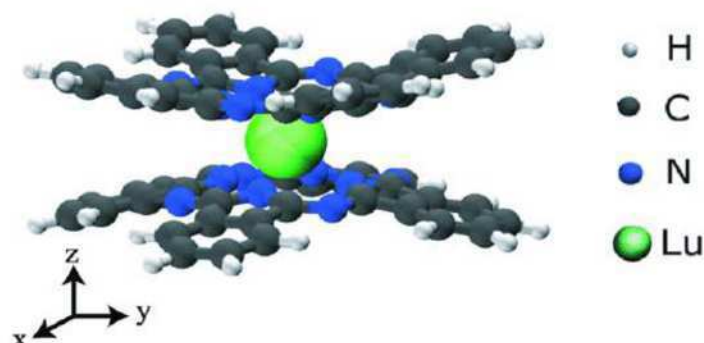


Figure 4.8: LuPc_2 structure optimized by DFT calculations.

Despite a very large amount of work devoted to the elucidation of molecular interaction of Pc molecules on metal surfaces,[90, 91] only few studies have focused on the semiconducting surfaces[92, 93] and even less on double-decker Pc's on these technologically relevant surfaces [94, 95] . On most metallic surfaces, Pc molecules are known to lie flat, whereas the molecular architectures are various on semiconducting substrates. Pc molecules are found lying flat on InSb(001) surface,[92] whereas they are inclined on Si(001) [94, 64]. Furthermore, a transition from lying-down to standing-up configura-

tion occurs in less than one monolayer of CuPc on Si(111) [96]. The different orientations are also observed on passivated surfaces. PbPc molecules are found to be flat on passivated Ge,[97] whereas CuPc molecules are standing up on Si(001) passivated with H or NH₃ [98]. In this context, the deposition of LuPc₂ adsorbed on Si(100)-2×1 is here investigated by means of synchrotron based techniques, such as XPS and NEXAFS, in combination with DFT calculations. The present experiments were performed on a Si(100)2 × 1 reconstructed surface with dangling bonds and a Si(100)2 × 1:H monohydride surface in which the dangling bond is terminated by a hydrogen atom (H passivated).

Experiments were carried out at the Swedish national synchrotron MAX-Lab. The Si(001)2 × 1 surface, when prepared under UHV, is formed by rows of Si dimers. Because of the crystalline anisotropy extends, only on small regions with respect to the light beam, and the surface is actually composed of 2 × 1 and 1 × 2 domains rotated by 90° with respect to each other, yielding an overall isotropic surface. In order to obtain a single-domain surface, we have been using a well known and controlled method, namely the use of vicinal Si(001) surfaces with a miscut of 4° along the [110] direction. This miscut gives terraces of 3-4nm width, which is roughly the size of the phthalocyanine molecule.

The samples were prepared by direct current heating for several seconds at 1050°C. The pressure was maintained below 3 × 10¹⁰ Torr during heating. The steps at the surface gather two by two to form dimers are all parallel to the steps, as can be seen in the scanning tunneling microscopy image of Fig. 4.9. The dimer rows can be distinguished and are perpendicular to the steps. This procedure yields to the pristine 2 × 1 single-domain, highly reactive surface. The adsorption of atomic hydrogen on the surface can “passivate” the dangling bonds, leading to a much less reactive surface. Atomic hydrogen is obtained by dissociating molecules of hydrogen by using a hot tungsten wire located in front of the sample. This results in a unreconstructed and poorly ordered Si(001)1 × 1:H surface where the Si dimers are broken and the Si atoms are bound to two H atoms.

4.2.1 LuPc₂ on passivated Si(100)-2×1:H

Si2*p* XPS spectra recorded for an excitation energy of 160 eV are displayed in Fig. 4.10; all spectra have been normalized to unity at the main peak. Si 2*p* on clean silicon (red line), identical to previously published spectra on stepped surface,[100] presents a pronounced surface state at lower binding energy that characterizes

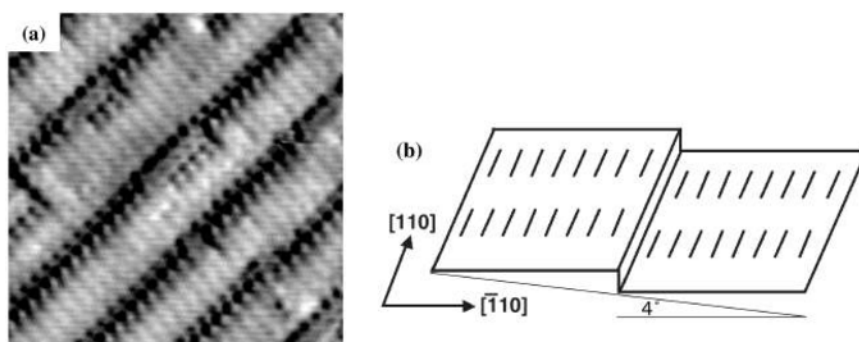


Figure 4.9: (a) STM image of a clean Si(001) 2×1 vicinal surface, from Ref[99]; (b) schematic drawing.

a clean and well reconstructed (100)- 2×1 vicinal surface. After hydrogenation, the Si dangling bonds have been terminated with hydrogen and therefore no surface states are visible in the spectrum (orange dashed line Fig. 4.10). The general spectral shape is also modified and is similar to the one already published.[101] Moreover, the spectrum presents an energy shift of 0.3 eV to higher binding energy, commonly attributed to a band bending due to the charge transfer between adsorbed hydrogen atoms and silicon.[100] The small feature at around 101.4 eV is characteristic of a Si^{2+} oxidation state[102] and is attributed to a slight water contamination during the hydrogenation process. The green line corresponds to 0.2 nm of LuPc_2 deposited on the hydrogenated surface. The overall shape of the spectrum is identical to the hydrogenated one and no additional features, which could be an indication of a bonding between the molecules and the silicon, are visible. This supports the fact that the passivated Si surface does not interact significantly with the LuPc_2 molecules.

Fig. 4.11 displays the C 1s spectra recorded for a thin film of 1 nm (a) and for a thick film deposition (b) on the H-terminated Si surface. The binding energy of the main structure is found at the same position as in previously published XPS on LuPc_2 thick film on silver[103] and no energy shift is observed for the different thicknesses, indicating equivalent interaction for the thin and thick layers, a consequence of the Si surface passivation.

The C 1s XPS spectra provide further evidence of the negligible interaction between the adsorbed molecules and the silicon atoms. The spectra can be decomposed using Voigt functions into a series of six peaks. The three larger peaks at lower binding energies corresponding to inequivalent carbons (illustrated in the sketch of

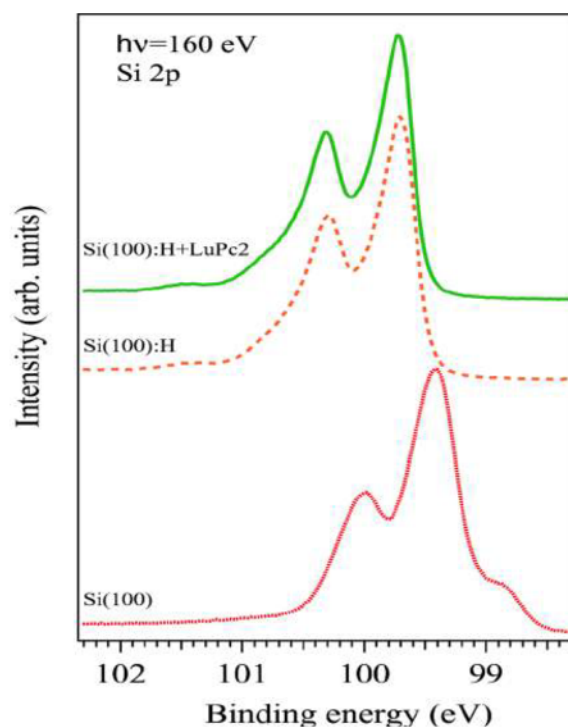


Figure 4.10: Silicon 2p XPS spectra recorded for a photon energy of 160 eV: clean silicon (100)- 2×1 vicinal surface (red line); hydrogenated silicon (100)- 2×1 vicinal surface (orange dashed line); 0.2 nm of LuPc₂ on hydrogenated silicon (100)- 2×1 vicinal surface (green line on top).

Fig. 4.11) are found, respectively, at 284.29 eV for the C-H contribution, 284.66 eV for the C1 contribution, and 285.48 eV for the C2 contribution. The three smaller additional features at higher binding energies correspond to the shake-up transitions associated with the three main transitions C-H, C1, and C2. Shake-up satellites are identified at higher binding energies (i.e., lower kinetic energy) due to a kinetic-energy loss of photoelectrons via simultaneously excited $\pi - \pi^*$ transitions. Fitting parameters are found in Table 4.2.

The intensity ratio [C1+shake-up : C2+shake-up : CH+shake-up] is found to be [1.9 : 1.9 : 4] for the 1 nm layer and [2.1 : 1.76 : 4] for the bulk layer. The C2 intensity ratio is smaller than 2 due to a slight beam damage of the layer. The overall ratios are in very good agreement with the numerical ratio of distinct types of carbon atoms identified within the molecular ligand [2 : 2 : 4].

The fitting procedure reveals also the energy difference between the main feature and its associated shake-up. For each feature, both in the 1 nm thick film or in the bulk-like overlayer, the shake-up is found to be at 1.9 ± 0.2 eV higher binding energy than the corre-

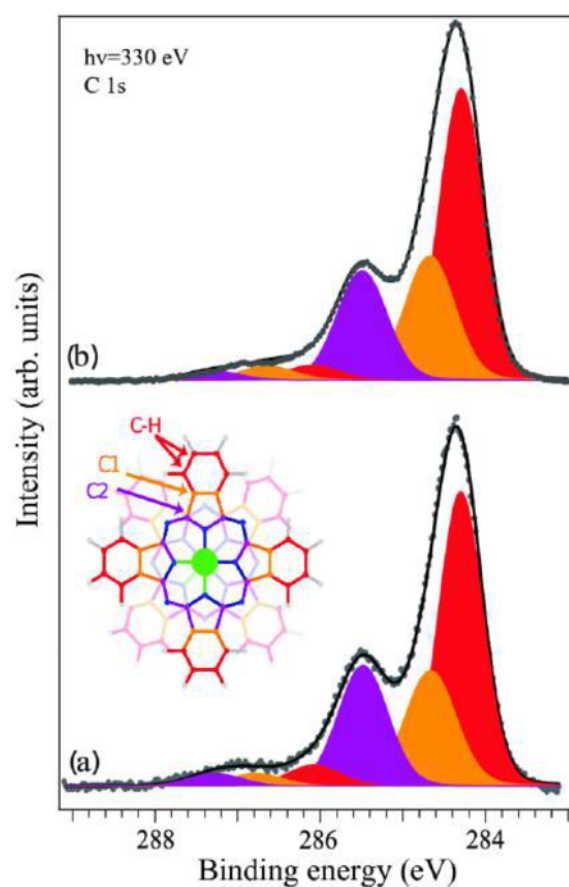


Figure 4.11: C 1s XPS spectra recorded for photon energy of 330 eV on LuPc₂ deposited on hydrogenated silicon (100)-2 × 1 vicinal surface: (a) 1 nm; (b) bulk LuPc₂; decomposition with Gaussian function is displayed for each spectra.

sponding main feature. This shake-up retains informations on the molecular band gap and agrees with already published results.[104, 105] Considering the results obtained on Si2*p* and C1*s* spectra, we can conclude that, as expected, there is no significant interaction between the molecules and Si atoms. However, more insights into the electronic structure of this double decker Pc come from the absorption spectra and from the DFT simulations presented further.

Fig. 4.12 displays the NEXAFS spectra of nitrogen, recorded in Auger electron yield mode in an energy window of 30 eV around the nitrogen KLL transition at 370 eV. Electrons were detected in a 45° angle with respect to the polarization vector. The spectra were first normalized to the intensity of the incoming light measured on a gold mesh, then normalized to unity at 425 eV. Two polarizations were investigated: in-plane polarization (IPL, red line) for which

Table 4.2: Fitting parameters for 1 nm thick and bulk films, FWHM corresponds to the full width at half maximum of the Voigt curve.

Peak label	Position (eV)		FWHM (eV)		Height (Arb. Un.)	
	1 nm	bulk	1 nm	bulk	1 nm	bulk
C-H	284.29	284.29	0.62	0.62	0.82	0.82
C-1	284.66	284.66	0.72	0.71	0.32	0.35
C-2	285.48	285.48	0.71	0.71	0.34	0.31 ^a
Shake-up C-H	286.08	286.08	0.76	0.76	0.06	0.04
Shake-up C-1	286.78	286.78	0.76	0.76	0.04	0.04
Shake-up C-2	287.28	287.28	0.76	0.76	0.04	0.03

^aBeam damaged sample.

the polarization E vector of the radiation is parallel to the surface and out-of-plane polarization (OPL, blue dashed line) for which the polarization was about 83° from the surface plane². The photon energy calibration was done by measuring the first and second order light from the Si 2p core level for thin layers, and C1s core level spectra for thick layers. The overall resolution of NEXAFS spectra is about 100 meV. Due to poor statistics for thin layer measurements obtained on I511, data from another experiment performed on D1011 (Max-Lab) on the same system were used, taking care that the overall line shape of both spectra was identical.

Four different thicknesses are presented, i.e., from thin layer to bulk-like film (0.3 nm in (a), 1.5 nm in (b), 2.4 nm in (c), bulk in (d) being less than 10 nm). The features in the NEXAFS spectra of phthalocyanine molecular films at the N 1s edge are generated by electronic transitions from a core level to an unoccupied electronic level either with π or σ character. In the following part, we will use the convention that the aza-bridge nitrogen atoms are those connecting the pyrrole rings of the LuPc₂, while the pyrrole nitrogen atoms are those directly bonded to the lutetium atom in the central part of the rings. In the NEXAFS spectra of Pc films, the region where the π^* transitions are observed presents four main features that are labeled from A to D (peak A at around 398 eV, peak B at about 400 eV, peak C at about 403 eV and peak D at about 404 eV) as shown in spectrum (d) of Fig. 4.12. The broad absorption features at higher photon energies correspond to σ^* transitions (peaks E at around 407 eV and peak F at 409 eV, shown in spectrum (d) of Fig. 4.12). As for XPS results, no shifts in energy are observed with increasing thicknesses.

Information about the orientation of the molecules can be de-

²For an explanation of the experimental geometry we refer to Section 2.0.4

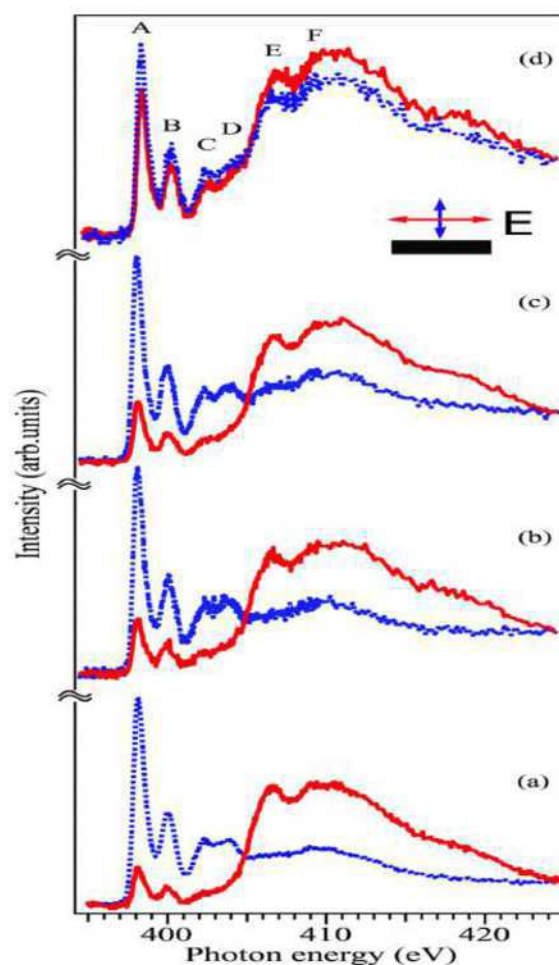


Figure 4.12: NEXAFS spectra at the nitrogen 1s edge for incoming photons with in-plane polarization (IPL, red line) and out-of-plane polarization (OPL, blue dashed line); increasing thicknesses are displayed (a) 0.3 nm, (b) 1.5 nm, (c) 2.4 nm, and (d) bulk.

duced from the relative intensities of the π^* and σ^* peaks in spectra taken at different orientations of the polarization vector \mathbf{E} of the incident radiation with respect to the sample surface. Since π^* transitions dominate with OPL polarization, whereas σ^* transitions are dominant with IPL polarization, the molecules in films are found to lie rather flat on the surface at low coverages (spectra (a)-(c) in Fig. 4.12). The bulk spectra (Fig. 4.12(d)) show instead similar intensities for both π^* and σ^* resonances for the two incident polarizations (IPL and OPL). This can be ascribed either to a more tilted adsorption orientation of the molecules or to a less ordered overlayer, as will be further discussed.

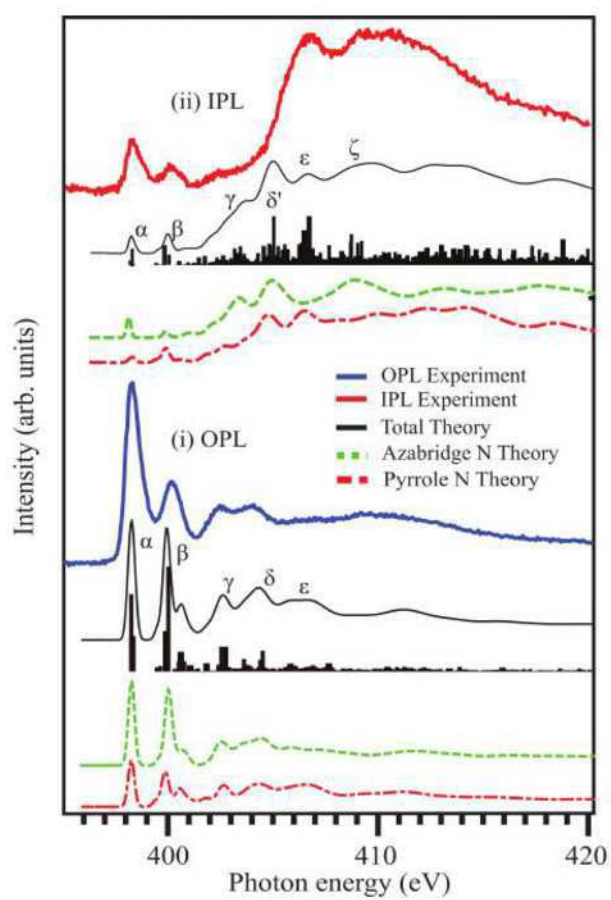


Figure 4.13: Experimental and theoretical NEXAFS: (i) π^* resolved calculation and measurement for OPL polarization of a 0.3 nm thick film, (ii) σ^* resolved calculation and measurement of IPL polarization of a 0.3 nm thick film.

The simulated absorption results, together with the experimental spectra for the 0.3 nm film are presented in Fig. 4.13 and for the bulk layer in Fig. 4.15. The ground state calculation and geometry optimization of LuPc₂ were performed by means of DFT calculations using the GAUSSIAN 09 program with the hybrid UB3LYP exchange-correlation functional. The DFT optimized structure is shown in Fig. 4.8. It belongs formally to the C_{4v} point group. Both, the experimental molecular structure by De Cian et al. [106] and the DFT optimized, structures have the rings rotated by 45° with respect to each other, sandwiching a lutetium atom. To simulate the N1s NEXAFS spectra, we have applied the transition-potential approach (TPA) [107] where, the electronic relaxation effects induced by the transition of an electron from an initial to a final state are simulated by the introduction of a half core hole at a particular core level. In the case of LuPc₂, two spin polarized TPA calculations, one for each non-equivalent nitrogen atom, were performed. To simulate the polarization resolved X-ray absorption spectra, the partial density of states (pDOS) of unoccupied *p*-orbitals was considered (i.e. the orbitals with energies above the HOMO) for each of the two non-equivalent nitrogen atoms. The projections of the pDOS along the three spatial coordinates *x*, *y*, and *z* correspond to the intensities of the spectra along the same directions: *I_x*, *I_y*, and *I_z*. When LuPc₂ is adsorbed parallel to the surface, the in-plane components *I_x* and *I_y* represent the electron excitations into the unoccupied σ^* states, collectively indicated as *I_σ*, whereas the out-of-plane component *I_z*, orthogonal to the molecular plane, represents the excitations into the unoccupied π^* states, indicated as *I_π*. In the comparison with the experimental NEXAFS, we need to consider additionally the possible tilting of the adsorbed molecules with respect to the surface plane. When the molecule is tilted, the results of the measurements cannot be compared with pure theoretical *I_σ* and *I_π*.

The tilt angle can, however, be simulated in the calculations by assuming an angle θ between the C₄-fold axis of the molecule and the *z* axis of our reference system. Due to the orthogonality of the components *I_x*, *I_y*, and *I_z*, the pDOS of a tilted molecule is obtained as a combination of *I_σ* and *I_π* with the angle θ as a parameter. The total spectrum of a molecule tilted by θ can thus be expressed as the sum of $I_{\pi} \cos(2\theta)$ and $I_{\sigma} \sin(2\theta)$ where $I_{\pi} = I_z$ and $I_{\sigma} = 0.5(I_x + I_y)$. The *I_π* and *I_σ* intensities correspond to tilt angles θ equal to 0° and 90°, respectively. The total N1s spectrum was aligned to the experimental energy scale. To facilitate the comparison with the experiment, the pDOS was convoluted with a Gaussian curve.

We used a Gaussian with a full width at half maximum (FWHM) of 0.35 eV below 399 eV, a linearly increasing FWHM from 0.35 to 1.7 eV up to 413.9 eV, and a constant FWHM of 1.7 eV above 413.9 eV.

In part (i), we show a π^* resolved (I_π) calculation in comparison with the measured OPL spectrum of the 0.3 nm film. In part (ii), we show a σ^* resolved (I_σ) calculation in comparison with a measured IPL spectrum of the 0.3 nm film. The black curves are the total theoretical spectra, obtained by summing the pyrrole (red curve) and aza-bridge (green curve) nitrogen contributions. The bar graphs show the pDOS eigenvalues above HOMO obtained for both non equivalent nitrogen species. In the total theoretical spectra of Fig. 4.13, the peaks labeled with greek letters from α to χ with increasing energy have a good agreement with the experimental peaks A-F indicated in Fig. 4.12.

The OPL calculation is characterized by a number of resonances below 406 eV. The features α to δ of π^* character at about 398 eV, 400 eV, 403 eV, and 404 eV reproduce well the experimental peaks in the same energy region. The peaks C and D of the experiment, corresponding to Rydberg states, match well the γ and δ in the calculation.

The IPL calculations present very intense features above the photon energy of 406 eV, in the σ^* region which starts with a pronounced edge at about 407 eV. The theoretical σ^* resonances labeled ϵ and χ are at 407 eV and at 409 eV. The peaks α and β are both clearly present in the IPL calculations and in the measured spectrum, and are very likely due to the non-planar geometry of the molecule. According to our computations, however, the different N species contribute with different intensities to these features. The intensity of the α peak is mainly due to the contribution of the aza-bridge nitrogen (green dashed curve), while the intensity of the β peak is mainly due to the contribution of the pyrrole nitrogen.

It is worth analyzing in more detail the origin of the α and β intensities in the spectra presented in Fig. 4.13, part (ii). Earlier NEXAFS studies on metal-phthalocyanines (MePc) have determined similar threshold peaks in IPL polarization measurements.[64] These peaks result from the interaction of the pyrrole N atoms with the metal center. In metal-free phthalocyanines, no such peaks were observed in the IPL polarization [108]. However, the structure of LuPc₂ is more complex than that of M-Pcs with a single Pc ring, due to the conjugation of two rings. One has to consider both the interaction between the metal and the Pc rings, and also the interaction of the two Pc rings with each other. For the OPL calculation,

the intensities for each N species are similar, while for IPL α has mainly contributions from the aza-bridge N and β from the pyrrole N.

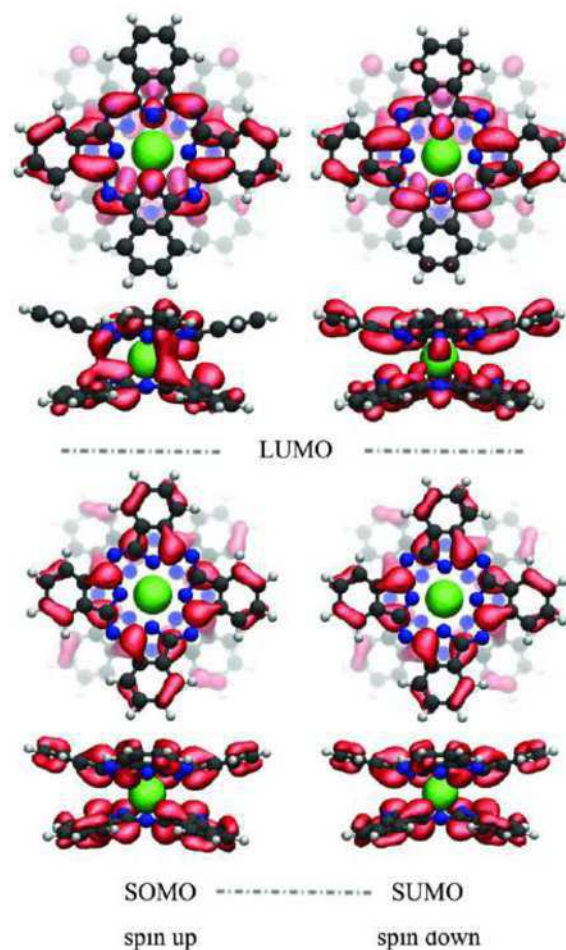


Figure 4.14: Spin-up and spin-down charge densities obtained from the ground state calculations for SOMO/SUMO and LUMO, respectively. The same coloring of atoms was used as in Fig. 4.14.

The spin resolved charge densities of the ground state displayed in Fig. 4.14 can give further information on the character of the first unoccupied molecular orbitals. We show the semi-unoccupied molecular orbital (SUMO) and SOMO and the LUMO for both spin states. The orbitals are delocalized over the whole molecule. The N atoms give only a small contribution to the HOMO (not shown here) and to the SUMO, while they contribute significantly to the LUMO and LUMO+1 (not shown here). Spin-up and spin-down LUMO have contributions from both the aza-bridge and pyrrole

nitrogens, and from their neighboring carbon atoms. π^* like orbitals connect the two molecular rings in the spin-up LUMO and spin-down SUMO. In spin-up LUMO, there appears also some charge density originating from the interaction of the pyrrole N with the Lu atom. Our theoretical results indicate, therefore, that the Lu atom has influence on the low energy unoccupied levels: the interaction of the pyrrole atoms with the Lu leads to a partial occupation of the LUMO resulting in a lower intensity in the simulated NEXAFS spectra (red line in part (i) in Fig. 4.13). The low energy peaks also originate from the π^* like orbitals which extend between the two molecular rings.

Looking at the features at higher photon energies, one can observe that the theoretical features γ and δ are not in agreement with the IPL measurement (Fig. 5, part (ii)). The differences in intensity of the peaks δ in part (i) and δ' in part (ii), which are also slightly shifted in energy with respect to each other, can be ascribed to the limitation of the computational methods. In addition, effects like lifetime broadening and vibrations could also contribute to aberrations leading to the observed differences.

In spite of these differences, the overall agreement between theory and experiment is very satisfactory. As mentioned previously, the NEXAFS spectra shown in Fig. 4.12 display a change of the molecular orientation between the thinner films (a)-(c) and the bulk (d). For the 0.3 nm film (a), we can assume adsorption parallel to the surface. This is also supported by the excellent agreement between theoretical and experimental results shown in Fig. 4.13. Moreover, the minor differences of the π^* and σ^* relative intensities observed in Figs. 4.12 lead us to conclude that the molecules maintain about the same orientation for presented coverages.

For the highest coverage, on the contrary, we note that the NEXAFS spectra in Fig. 4(d) show little difference in the relative π^* vs. σ^* intensity ratio for the two polarizations. The little variation in intensities as a function of the polarization can be ascribed to a molecular adsorption with an average tilt angle θ of approximately 45° . In Fig. 4.15 the spectra relative to the thick film are simulated considering an E-vector of the incident radiation forming an angle θ equal to 45° . The total intensity I_{tot} at θ can be approximated then by

$$I_{tot}(45^\circ) = \cos^2(45^\circ)I_\pi + \sin^2(45^\circ)I_\sigma \quad (4.1)$$

In this way, a 45° tilted molecule is simulated. The very good agreement between the calculations and the polarization dependent

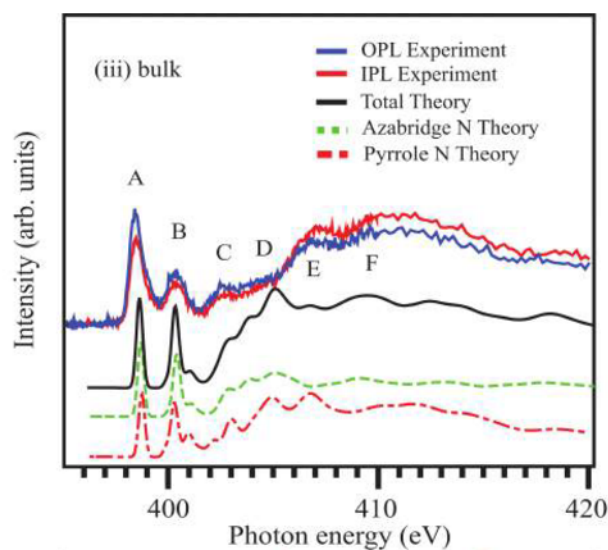


Figure 4.15: Experimental and theoretical NEXAFS: calculation for $\theta = 45^\circ$ composed of π^* and σ^* calculation compared to bulk measurements; black curve shows total orientation resolved calculation; dashed red and green lines show pyrrole and aza-bridge N contributions, respectively; red and blue curves show measurements of the IPL and OPL polarizations.

measurements up to 407 eV leads to suggest a staggering of the molecules close to 45° . However, it is important to mention that similar results regarding the relative π^* vs σ^* intensities at different acquisition geometries can be due to a disordered film. To answer this question, additional studies need to be carried out.

4.2.2 LuPc₂ on pristine Si(100)-2×1

The measurements shown here were performed on clean Si(100)-2×1 vicinal and nominal surfaces. Comparisons with passivated Si(100)-2×1 surfaces of the previous Section are also discussed.

LuPc₂ molecules were synthesized following literature methods [109]. A Knudsen cell type evaporator from Ferrovac was used to evaporate LuPc₂ molecules, which were outgassed for a few hours at 250°C until recovering the base pressure (low 10^{-10} mbar range). During the molecular deposition, the crucible was heated resistively to around 300°C, while keeping the vapor pressure in the 10^{-9} mbar range.

The thicknesses of the organic films were estimated from Photoelectron Spectroscopy data using a so-called overlayer method [20], monitoring the change in intensity of the Si2p peak upon absorption of LuPc₂.

Density Functional Theory (DFT) calculations were performed in the group of Dr. Barbara Brena at the University of Uppsala with the plane wave based code VASP[110, 111, 112, 113]. In all calculations, the Brillouin zone was sampled at the Γ -point and the electronic states were described in the projector augmented wave (PAW) method [114, 115] with a kinetic energy cutoff of 400 eV. The many-body effects between the electrons manifesting in correlation and exchange energy, were accounted with the semi-local generalized gradient approximation in the flavor of PBE [116] in the single particle picture drawn by DFT. This set up was used to compute adsorption energies and structures, as well as PES spectra of the C and N atoms in LuPc₂.

The optimized gas-phase LuPc₂ molecule was deposited at a minimal distance of 3.3 Å perpendicular to the substrate. The reconstructed Si(100)-2×1 was built with the experimental lattice constant (a_0) of 5.431 Å in three layers where the lowest layer was passivated with hydrogen atoms being optimized in a separate calculation. The structural optimizations, performed until all Hellman-Feynman forces were less than 0.02 eV/Å, included van der Waals (vdW) forces described by the Tkatchenko-Scheffler (TS) method[117]. The adsorption energies were calculated as total energy difference between the adsorbed system, e.g. LuPc₂/Si(100), the energy of the single molecule and the bare surface.

The binding energies of the core-level electrons of the N and the C atoms were the focus of our investigations. For each of the 16 N atoms and the 64 C atoms in the LuPc₂ molecule, the relative binding energies were obtained by comparing the energy difference between the core ionized system with a 1s¹ configuration and the system in its ground state for each of the N and C atoms separately. Relaxation effects of the electronic density are included in the final state approach via the relaxation of the remaining electrons in the presence of the core-hole.

Here we distinguish between two types of core-level shifts. The first one labeled as Δ_{BE} is the shift due to the different chemical environment within the molecule, e.g. binding energy of atom C_{*i*} is compared to the one of C_{*j*}. The other shift is δ_{BE} , which compares the binding energy of the same atom before and after adsorption. The Δ_{BE} and δ_{BE} are averaged over the same kind of atoms (pyrrole and benzene like carbon atoms for C 1s and pyrrole and aza-bridge like nitrogen atoms for N 1s). They provide information about the strength of the chemical change induced via adsorption in an averaged way (Δ_{BE} and δ_{BE}). Also the distribution width, computed as standard deviation σ_{BE} , helps to reveal convolution effect in the ex-

perimental spectra and the BE range R_{BE} gives information about the largest BE changes.

DFT calculations were performed to gain a detailed understanding of the physical mechanisms occurring during the adsorption. The computed adsorption energies are found between 2.99 eV and 4.63 eV and the corresponding geometries of the adsorbed molecules become deformed through the strong chemical interaction with the substrate. The lowest energy structure with an adsorption energy of 4.63 eV, which was used to calculate the binding energies for all non-equivalent carbon and nitrogen atoms, is shown in Figure 4.16a. In this structure, the molecule has three of the isoindole rings, belonging to the lower Pc ring, bent towards the substrate, while the remaining one is lifted away from it. In the upper part of figure 4.16b, the non-equivalent nitrogen atoms are indicated in the top ring while in the lower part, the C atoms that are chemically bond to the surface, are highlighted. Figure 4.16c shows the changes in the charge density due to the adsorption of the molecule on the substrate. The DFT calculation demonstrates that a charge accumulation, shown in dark red color, is observed between the C and Si atoms, indicating the formation of bonds between the molecule and the substrate. Meanwhile, charge depletion regions, shown in light blue color, are observed around the π orbitals of the molecule, resulting in the conservation of charge. The observed changes are mostly dominant at the interface, while the upper Pc ring does not undergo major changes of the charge density.

The total charge redistribution between the Si surface and the LuPc₂ molecule, resulted in $0.28e$ /molecule being transferred from the Si surface to the LuPc₂ molecule according to the integrated charge transfer curve. This is illustrated in Fig. 4.16d, which shows the charge transfer curve along adsorption direction. Three different transfer regions exist in the chosen system. In the upper part of the LuPc₂ molecule, additional 0.19 electrons accumulate while in the lower part 0.33 electrons are depleted. In total, 0.42 electrons are between the molecule and the surface. The formation of dipoles within the molecule, between upper and lower Pc ring, and between the lower Pc ring and the Si surface can be noticed. A further indication for the chemical interaction of the six C atoms (C_{ben}^{Si}) of the lower ring with the surface are their computed short distances of less than 2.1 Å with Si atoms of the surface, which is similar to the distance of 1.8 Å already calculated for C₂H₄ on Si(100) surfaces [118].

Figure 4.17 shows a comparison between the experimentally obtained N 1s (a) and C 1s (b) core level spectra for a thick layer (2.7

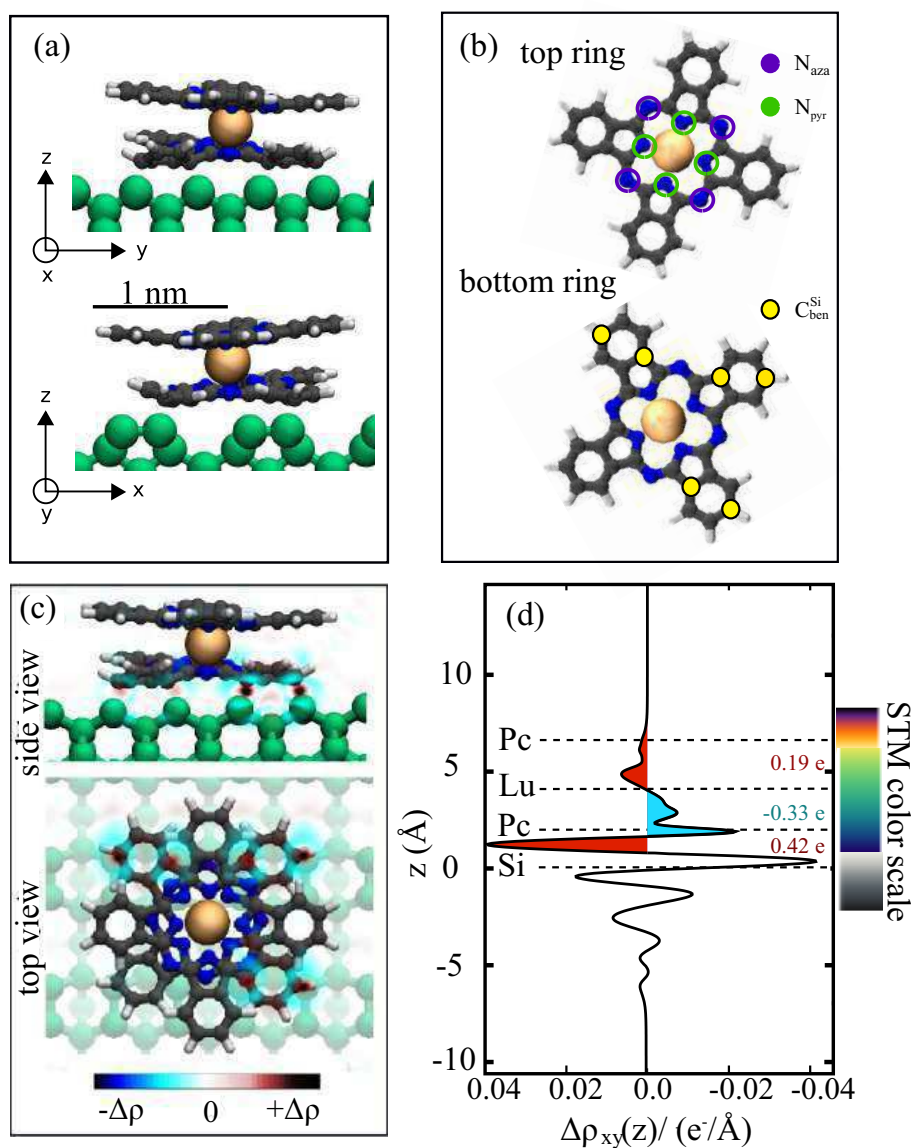


Figure 4.16: Results of the DFT calculations. The obtained structure of the adsorbed molecule is shown in (a). In (b) the upper and lower Pc rings are shown separately, indicating the different N species on the top ring and the chemically bonded C atoms ($C_{\text{ben}}^{\text{Si}}$) on the bottom ring. In part (c) the charge density difference due to the formation of chemical bonds is shown in red indicating the gain in charge density and in blue indicating the loss in charge density. This difference is mainly located at the lower Pc ring at the $C_{\text{ben}}^{\text{Si}}$ atoms. The charge transfer curve $\Delta\rho_{xy}(z)$ is plotted in (d) related to the distance z above the Si surface. The average heights of the surface Si atoms, the Lu ion, the lower Pc and the upper Pc ring are indicated. The relative charge transfers between different *neutral charge* planes are given for the indicated filled areas under the curve.

nm) of LuPc₂ on a hydrogenated Si surface [83] and a thin layer (0.5 nm) of LuPc₂ on a pristine Si substrate together with the calculated Δ_{BE} for the respective core level atoms. The Δ_{BE} s have been calculated for a C_{4v} symmetric molecule (gas phase) and for an adsorbed molecule on the pristine Si surface, and their relative positions have been aligned to the maximum intensity of the experimental results for easier comparison. The C 1s spectrum of the thick film is formed by an intense peak at 284.1 eV, attributed to the electrons coming from the benzene-like atoms (C_{ben}), a lower peak at 285.2 eV, attributed to pyrrole carbon atoms (C_{pyr}) and a broad and a low intensity feature observed around 286.8 eV due to a shake-up structure. The N 1s spectra on the thick layer is formed by one main peak at 398 eV coming from two non-equivalent N atoms - one in the pyrrole ring that is directly bound to the lutetium atom (N_{pyr}) and one in the aza-bridge, which is connecting the isoindole groups (N_{aza}). The shoulder on the higher binding energy side at 398.9 eV is ascribed to shake-up features from both N species.

In the case of a metal-phthalocyanine like FePc[64], the XPS energies have a typical splitting of 0.18 eV due to the chemically different nitrogen species (N_{pyr} and N_{aza}) in the molecule. This can also be found in the case of LuPc₂ in (Fig. 4.17a). For the adsorbed LuPc₂, the core-level calculations reveal that the additional spread of the experimental XP spectra arise from the deformation and adsorption of the molecule on the Si surface. When disentangling the BE positions for each of the Pc rings, we observe that the binding energies of the N 1s core levels are perturbed for both Pc rings. We note that the BEs of the N atoms of both Pc rings being directly bound to the metal center are more affected than the aza-bridge N atoms. Due to the complex electronic interaction between surface and molecule as well as the distortion of the Pc molecule, the BE range is much larger for the lower Pc ring, having a BE range of 0.58 and 0.53 eV for pyrrole and aza-bridge N atoms, respectively. The Δ_{BE} and δ_{BE} can be found in Tab. 4.3 together with the BE range (R_{BE}) is given.

Similarly, Fig. 4.17b shows a comparison between the experimental C 1s spectra and the calculated Δ_{BE} for all C atoms. In order to compare the calculated Δ_{BE} with the experimental results, we align the average BE of C_{ben} to the maximum peak position of the experimental data. The interaction with the pristine Si substrate, as in the case of N 1s, leads to a wider spread of the BE of the C atoms with chemically different surroundings. The analysis of the computed Δ_{BE} reveals that even though only six C_{ben}^{Si} form chemical bonds with the Si substrate, the BE positions of the rest of the

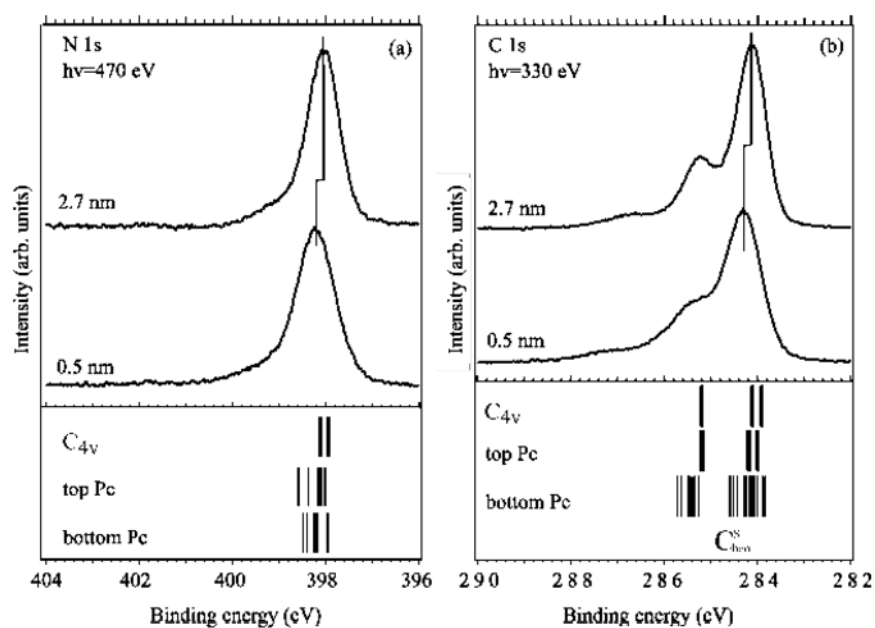


Figure 4.17: Comparison between the experimental XP spectra of the N 1s (a) and C 1s (b) and BEs for thin layers of LuPc₂ (0.5 nm) on pristine Si and thick layers of LuPc₂ (2.7 nm) on a hydrogenated Si substrate. The thicknesses of the adlayers are indicated in the figures. The calculated BEs for the “gas phase” single molecule (C_{4v}) and the adsorbed molecule are summarized at the bottom of the N 1s and C 1s spectra, respectively. The calculated BE shifts are aligned to the intensity maxima of the experimental results. The adsorbed case distinguishes between the top and the bottom Pc ring. Also the BEs of the C_{ben}^{Si} atoms are indicated in (b).

Table 4.3: Computed C 1s and N 1s BE data. Provided are the Δ_{BE} , δ_{BE} , the BE range (R_{BE}) and the standard deviation (σ_{BE}) for the “gas phase” single molecule (C_{4v}) in the upper table and for an adsorbed molecule on the pristine Si surfaces in the lower table. In the latter case, the values are resolved for the top and the bottom Pc ring separately. Δ_{BE} is the shift due to the different chemical environment within the molecule. δ_{BE} is the BE shift observed in the same atom due to adsorption. Resolved are the different atomic species, e.g. N_{pyr} , N_{aza} , the pyrrolic C atom C_{pyr} and the three different C atomic species in the benzene ring $C_{ben,i}$, $C_{ben,m}$ and $C_{ben,o}$ which can be found in the inner-, middle- and outer-part of the benzene ring, respectively. Also, the values for the C atoms bond to Si atoms, e.g. C_{ben}^{Si} , are provided. All values are given in eV.

LuPc ₂ (C _{4v})		Δ_{BE}	R_{BE}		
	C_{pyr}	0	0.00		
	C_{ben}	-1.15	0.20 ³		
	N_{pyr}	0.0	0.00		
	N_{aza}	-0.18	0.00		

LuPc ₂ /Si		Δ_{BE}	R_{BE}	δ_{BE}	σ_{BE}
top Pc	C_{pyr}	-0.03	0.09	0.03	0.03
	C_{ben}	-1.11	0.25	0.04	0.09
	$C_{ben,i}$		0.05		0.07
	$C_{ben,m}$		0.08		0.02
	$C_{ben,o}$		0.06		0.02
	N_{pyr}	-0.46	0.07	0.46	0.03
	N_{aza}	-0.37	0.06	0.20	0.03
bottom Pc	C_{pyr}	0.24	0.47	0.3	0.15
	C_{ben}	-1.13	0.78	0.04	0.22
	$C_{ben,i}$		0.61		0.28
	$C_{ben,m}$		0.46		0.20
	$C_{ben,o}$		0.43		0.17
	C_{ben}^{Si}	-0.71	0.18		0.07
	N_{pyr}	-0.34	0.58	0.34	0.28
	N_{aza}	-0.31	0.53	0.23	0.23

carbon atoms, notably the non-bonded carbon atoms of the bottom Pc, are also strongly affected. The average Δ_{BE} between benzene type carbon atoms (C_{ben}) and pyrrole type carbon atoms (C_{pyr}) is 1.2 eV for a single molecule and 1.1 eV for C atoms of the top Pc ring of the adsorbed molecule, which is consistent with previous studies of similar systems[108]. For the bottom Pc of the adsorbed molecule, the BE positions are rather different, having a BE range of 0.48 eV for the C_{pyr} and 0.78 eV for the C_{ben} atoms. This indicates that individual C atoms experience strong changes in the chemical environment. Even though the Δ_{BE} between the C_{ben} and C_{pyr} is 1.4 eV in the case of non-bonded C atoms and 0.95 eV for chemically bonded C atoms, the average Δ_{BE} remains similar to the “gas phase” single molecule calculations with Δ_{BE} of 1.2 eV between the C_{ben} and C_{pyr} contributions. This provides an explanation of why no major changes upon adsorption, except the broadening of the peak width, can be observed. Interestingly, the C_{ben}^{Si} atoms have very small σ_{BE} and Δ_{BE} , which points towards chemical equivalence and indicating as well the formation of bonds.

Two major changes affect the nitrogen and carbon XP spectra in the case of the thin layer adsorbed on the pristine silicon: a general shift to higher binding energy and a broadening of the overall spectra. The systematic shift to higher BE for both carbon and nitrogen core levels is in apparent contradiction with the prediction of 0.28e/molecule being transferred from the substrate to the molecule, that should result in a decrease of the BE for the thin layer as evidenced on metal systems [119].

Furthermore, two phenomena contribute to the energy shifts: the change in the valence cloud (i.e. charge redistribution and transfer between substrate and molecule as calculated in DFT), known as initial state effects, and the core-hole screening from the surrounding atoms, molecules and silicon substrate. Both effects typically differ in sign and can result in a small core-level shift to either higher or lower binding energy. Moreover, no BE shift is observed on the Si 2p core level that could also be an indication of the charge transfer suggesting that in the case of Pc adsorbed on silicon, screening effects are dominant due to the strong interaction between the molecule and the substrate. The latter fact is reflected in the large adsorption energies found in DFT.

From the comparison between experimental XPS core level spectra and DFT calculations, we have evidenced that the adsorption process mainly affects the lower ring of the molecule for the C atoms, whereas both rings are affected for the N contribution although to a smaller extent.

This investigation reveals that in the more stable configurations, the molecules adsorb rather flat on the Si(100)-2×1 surface, as confirmed also by STM studies [84]. Indeed, a bonding through the carbon atoms in the lower ring leads to a distorted geometry of the molecules for which a calculated charge transfer of 0.28e/molecule is found. The large adsorption energies between 3 eV and 4.6 eV indicate a strong molecule-substrate interaction entering in competition with the large molecule-molecule interaction of 2.7 eV computed for the first time on double decker phthalocyanines. This competition leads to the formation of clusters even at very low initial coverage as evidenced by STM [84]. A more important finding concerns the redistribution of the electronic cloud due to the adsorption onto silicon. The nitrogen atoms from both plateaus are weakly affected by the bonding with silicon, whereas for carbon atoms the electronic contribution in the lower plateau of the double decker is much more modified, leaving the upper plateau unaffected by the bonding. This particular result can be of great interest for possible future implementations in electronic devices, where the molecule's electronic characteristics would be preserved even on highly reactive substrate like pristine Si.

Chapter 5

Mapping out the future: the new generation sources

Time-resolved spectroscopy of electron dynamics and charge transfer has a high experimental and theoretical interest in modern atomic, molecular and condensed matter physics and chemistry. The objective of this research is to get a detailed picture of a sequence of events triggered by an ultrafast excitation, i.e. the absorption of a laser pulse. Time resolved experiments are capable to reveal, for example, the dynamics of charge or vibrational energy transfer between molecules during a reaction, or the rapid thermalization of a distribution of non-equilibrium electrons. The focus is on experiments in the femtosecond (10^{-15} seconds) time range. In this period of time, which is less than the vibrational period of a molecule, a reaction can exhibit transient excited molecular states previously identified as intermediate steps of the process.

Thanks to the advances in laser science of the last decades, it is now possible to produce soft X-ray pulses in the femtosecond range, using different approaches: laser-induced high-order harmonic generation in gas (HHG), free-electron LASERs (FEL), and laser slicing at synchrotron beamlines [120]. These approaches provide the possibility to characterize precisely and hopefully also to control, events in the picosecond and sub-picosecond time range.

In HHG, noble-gas atoms interact with an intense laser field and emit light at the harmonics of the latter. The intensity is small for low-order harmonics, increases monotonically with the harmonic order up to wavelengths extending into the soft X-ray regime, and drops quickly at some cutoff energy [121, 122, 123]. CITIUS is a state-of-the-art light source generating ultra short optical pulses in the VUV and soft X-ray spectral range, installed at the Laboratory of Quantum Optics of University of Nova Gorica. The light source

Table 5.1: FEL-1 and FEL-2 parameters. See also [126, 127]

Parameter	Value		Units
	FEL-1	FEL-2	
Wavelength ^d	100–20	20–4	nm
Pulse Length (FWHM) ^c	30–100	< 100	fs
Bandwidth (FWHM) ^a	1×10^{-3}		
Polarization	variable		
Repetition Rate	10^a ; 50^d		Hz
Energy/pulse ^a	> 50	> 10	μJ
Divergence (rms)*	1.25λ	1.5λ	μrad

^aachieved; ^ccalculated; ^ddesign; * λ in nm.

for different kind of experiments in several domains of both fundamental and applied research (e.g. pharmacology, clean energies, photocatalysis). The CITIUS source is presented in Sec. 5.1, together with a pump-probe experiment performed to characterize the pulse duration.

In a “free electron LASER” (FEL)’ relativistic electrons interact with their own electric field to generate very energetic, high power, coherent radiation. FEL radiation has much better characteristics than ordinary lab lasers, even HHG sources; in fact it is far more intense ($> 10^6$), the energy is tunable (from infrared to X-rays), has higher brilliance, and has a temporal structure characterized by rapid pulses.

FERMI at Elettra is the first FEL facility operated for user experiments in seeded mode. It is able to provide high power ultra short VUV and soft X-ray pulses up to multi GW peak power with pulse duration of the order of 100 fs, with a high level of stability for power and for wavelengths. The 100–4 nm wavelength range is covered by two distinct light sources: the long wavelength FEL-1 (100–20 nm) and the short wavelength FEL-2 (20–4 nm). The tuning of the wavelength of the seed laser by means of an optical parametric amplifier (OPA) combined with the use of undulators with variable gap allows the generation of FEL pulses over a range of continuous wavelengths. The main properties of the light delivered by FERMI (high brilliance, short pulse length, variable polarization, coherence) have been described in Ref. [124, 125] and are summarized in Table 5.1.

In Sec. 5.2 the Low Density Matter (LDM) beamline of FERMI is described. LDM was built to serve the atomic, molecular and cluster community and provides time-resolved experiments with different combinations of femtosecond pulses. The combined capabilities of the photon source discussed before, the photon transport and

the endstation allow the investigation of many targets, such as very dilute systems, matter under extreme irradiation conditions (multiple electronic excitation, multiple ionization, Coulomb explosion, non-linear optics) and dichroism. We describe the photon transport and a text experiment performed during the commissioning of the beamline.

5.1 CITIUS: an IR-XUV light source for ultrafast science

The light generation in a HHG source can be described by means of a semiclassical “three step model” [128] depicted in Fig. 5.1: In the first step, a bound electron is extracted from a gas atom under the action of the laser field (a); in the second step, the electron undergoes an oscillating motion imposed by the laser field (b); in the third step, the electron collides back with the parent ion (c) and, as a result, laser harmonics are emitted (d). The intensity is small for low-order harmonics, increases monotonically with the harmonic order up to wavelengths extending into the soft X-ray regime, and drops quickly at some cutoff energy [121, 122, 123].

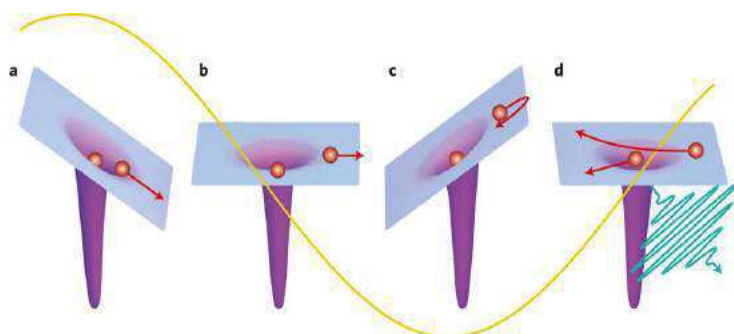


Figure 5.1: The three-step model of HHG. a) an intense femtosecond pulse extracts the electron; b) the electron is pulled away from the atom near the peak of optical field and accelerated; c) the optical field reverses, the electron is driven back where it can recollide with the parent ion; d) the parent atom emits a femto- or attosecond pulse. Figure from Ref. [129]

Since the electron dynamics in atomic, molecular or more complex systems occurs at timescales ranging from hundreds of femtoseconds down to tens of attoseconds, HHG sources provide an ideal tool to study, and possibly control, the interactions between charge, lattice, orbital, and spin dynamics in a chemical reaction.

In 2008, a new project has been funded in the framework of the Cross-border cooperation program between Italy and Slovenia 2007-

2013 [130]. Project's main objective is to set up a state-of-the-art light source at University of Nova Gorica (Slovenia). The source, named CITIUS, has been assembled and commissioned at Elettra-Sincrotrone Trieste (Italy) and is going to be moved to Slovenia. The mission of the new Slovenian laboratory is to carry out cutting-edge experiments in a wide range of both applied and fundamental fields, including materials science, catalysis, biochemistry and magnetism. Part of the envisaged scientific program will be connected to that developed at the Low-Density Matter beamline at the FERMI free-electron laser [131].

In this paper, we first provide a technical description of CITIUS, and then report the results of two proof-of-principle pump-probe experiments, namely the characterization of the temporal structure of HHG pulses, and the selective investigation of the ultra-fast dynamics of different elements in a magnetic compounds.

5.1.1 The laser system and the beamline

The CITIUS laser system and the beamline are schematically shown in Fig.5.2. The laser system comprises a commercial amplifier Legend Elite Duo and an optical parametric amplifier OPerA (OPA), both produced by Coherent Inc. The amplifier is seeded by a Mira oscillator (wavelength: 800 nm, spectral bandwidth about 100 nm, power about 380 mW) and includes two amplification stages: a regenerative amplifier (EVO 30), pumped by an Evolution 30 laser (frequency-doubled Q-Switched Nd:YLF laser), and a single-pass amplifier (EVO HE), pumped by an Evolution HE laser (frequency-doubled Q-Switched Nd:YLF laser). The system can be operated at four different repetition rates: 100 Hz, 1 kHz, 5 kHz and 10 kHz. At 5 kHz, which is the currently adopted repetition rate, it generates pulses carrying about 3.1 mJ, with a duration of about 35 fs, centered at 805 nm. Two thirds of the energy is used for generating XUV pulses through HHG, one third as a pump for the OPA, or directly in combination with the HHG beam for pump-probe experiments. The OPA produces tunable radiation in the range between 0.4 eV and 5.6 eV, with variable energy per pulse (from few to hundreds of microjoules).

The beamline includes a high-vacuum section, through which the XUV beam propagates, and a section in air, used to transport the IR-UV light generated by the OPA. The XUV part comprises a HHG generation chamber and a monochromator. The laser is focused in the generation chamber (using the lens L1, see Fig. 5.2), where it interacts with a noble gas of choice (Ar or Ne, for the reported ex-

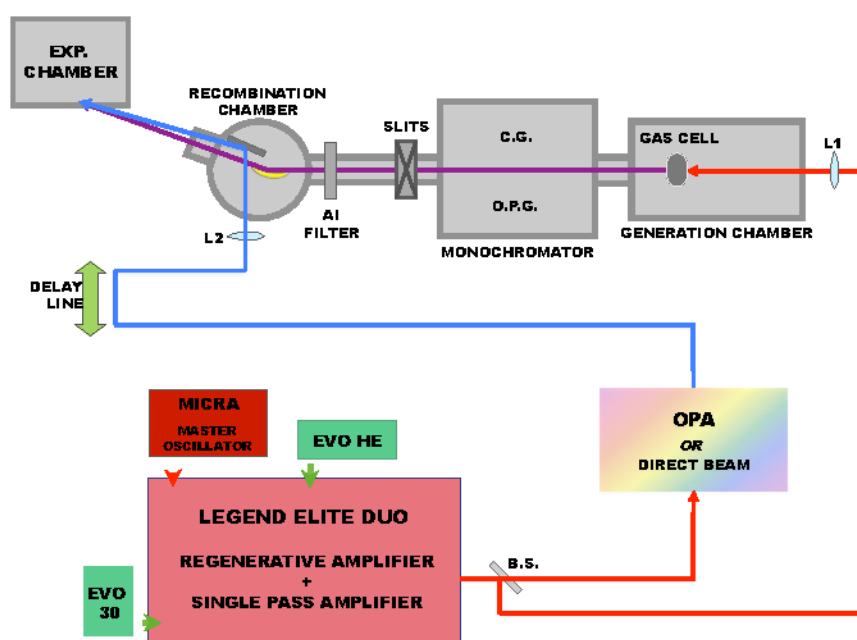


Figure 5.2: Layout of the CITIUS source including the laser system, the harmonic generation chamber, the monochromator, the recombination chamber, the delay line, and the experimental chamber. The light generated by the Legend amplifier is separated in two parts by the beam splitter BS. The reflected part (about two thirds of the incoming beam) is focused (lens L1) into the generation chamber, where it is used for HHG. The HHG beam is monochromatized, filtered (in order to eliminate the residual IR beam) and sent into the refocusing chamber. From there, it is finally focused into the experimental chamber, using a toroidal mirror. The part of laser beam transmitted by BS is either sent to the OPA, or transmitted directly. The OPA/direct beam is then sent through a delay line, focused (lens L2) and reflected (by a planar mirror located in the refocusing chamber) into the experimental chamber. In the monochromator, the classical geometry configuration is used for high-energy resolution measurements, while the off-plane geometry is used for high-temporal resolution measurements. In the monochromator, CG and OPG stands for “classical geometry” configuration and “off-plane geometry” configuration, respectively (see Fig. 5.3 for details about the two configurations).

periments) contained in a cell, generating the high-order harmonics. The harmonic generation efficiency can be optimized by varying the pulse energy, the gas pressure (typically, of the order of 10^{-3} mbar) and the relative position of the laser focus within the cell.

The monochromator, whose scheme is shown in Fig. 5.3, was developed by the C.N.R.-I.F.N. Padova (Italy) and will be described in detail in a different paper [132]. It was designed to select one single harmonic, or a sub-band of it, in the spectral range between 250 and 25 nm (5-50 eV). However, the transmitted energy range could be further extended at the expense of efficiency, up to 100 eV. The CITIUS monochromator is superior to similar systems [133, 134], in that it adopts a single-grating design with a double configuration [135, 134, 136]: an off-plane geometry (OPG) for ultrafast response (few tens of femtoseconds) at the expense of energy resolution, and a classical geometry (CG) for high-energy resolution, albeit with long temporal response (several hundreds of femtoseconds). A first toroidal mirror collimates the light coming from the generation chamber and deflects it onto a planar (OPG or CG) diffraction grating. The diffracted light is then refocused by a second toroidal mirror onto the exit slit. The characteristics of the OPG and CG gratings are reported in Table 5.2.

Table 5.2: Characteristics of the monochromator gratings. The energy resolution has been calculated on a 100- μ m-wide exit slit.

Off-plane geometry	
Grating 1 (groove density: 200gr/mm)	
Spectral region	100-250 nm (12-5 eV)
Energy resolution	0.1 eV @ 10 eV
Grating 2 (groove density: 400gr/mm)	
Spectral region	27-100 nm (45-12 eV)
Energy resolution	0.2 eV @ 20 eV
Grating 3 (groove density: 600gr/mm)	
Spectral region	12-40 nm (100-30 eV)
Energy resolution	0.5 eV @ 40 eV
Classical geometry	
Grating 1 (groove density: 300gr/mm)	
Spectral region	80-250 nm (12-5 eV)
Energy resolution	10 meV @ 10 eV
Grating 2 (groove density: 600gr/mm)	
Spectral region	50-100 nm (25-12 eV)
Energy resolution	20 meV @ 20 eV
Grating 3 (groove density: 1200gr/mm)	
Spectral region	30-60 nm (41-21 eV)
Energy resolution	40 meV @ 40 eV

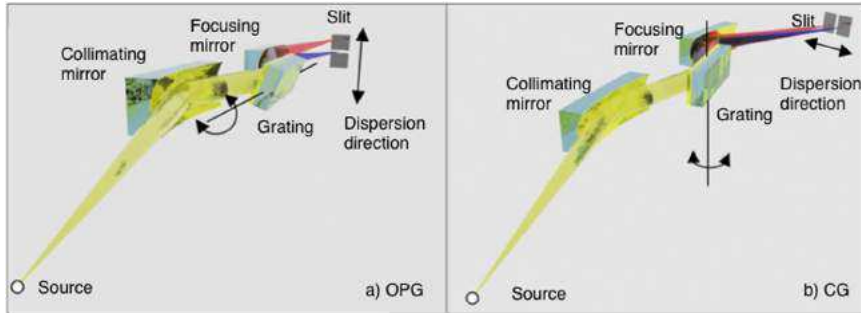


Figure 5.3: Light paths inside the monochromator: a) off plane geometry (OPG); b) classical geometry (CG).

The branch transporting the OPA/IR beam includes a delay line, allowing one to control the optical path difference between the pump and probe beams with sub-micron precision. The OPA/IR beam is refocused by a lens (L2 in Fig. 5.2) and intercepted by a flat mirror (BK7, high-reflectivity, replaceable according to the specific wavelength in use) hosted in the recombination chamber. At the exit of the monochromator, the XUV beam passes through a 200 nm thick Al filter (to stop the residual seed laser light) and enters the recombination chamber. The chamber hosts a toroidal mirror (Si:Au coated, with 1200 mm focal length) to refocus the monochromatized XUV light at the sample position. The mirror sits in a two-axes motorized mount, to guarantee (with micrometric precision) a perfect spatial overlap between the pump and probe beams onto the sample. The pump and probe beams impinge onto the sample in an almost collinear geometry in order to minimize the temporal resolution spread due to the lateral spots dimensions. The HHG spot has been measured to be about $150 \mu\text{m}$ (FWHM) at the sample position, while the OPA beam focusing is adjusted in order to obtain a spot approximately twice as big. This ensures a homogeneous excitation of the probed area. The energy density of the IR-UV at the interaction point has been estimated to be of the order of $10 \text{ mJ}/\text{cm}^2$.

5.1.2 HHG performance

We measured the quality and sizes of the XUV spots after the refocalization chamber at 1200 mm from the center of the refocalizing mirror, where the XUV spot is focused. In Fig.3 left, we present the XUV spot of the 23^{rd} harmonic generated in Ar. The OPG G400 grating was used, with a slit aperture of $200 \mu\text{m}$. The measured

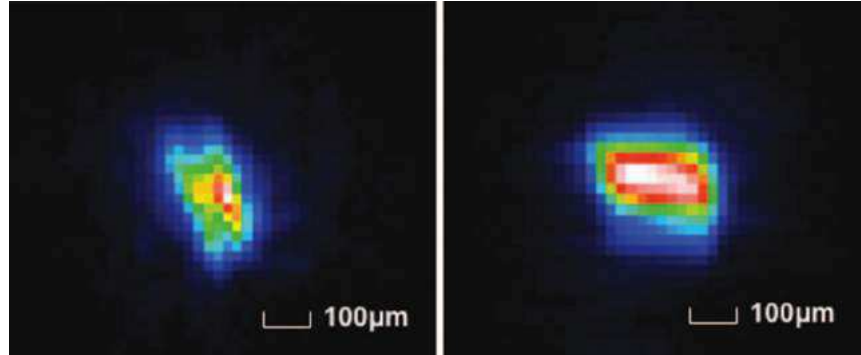


Figure 5.4: XUV spots generated in Ar, with a slit aperture of 200 μm . (left) XUV spot of the 23rd harmonic with OPG G400 grating, and size 140 μm x 220 μm .; (right) XUV spot of the 25th harmonic with CG G1200 grating and size 220 μm x 120 μm . All spots have been acquired using a CCD camera (PIXIS-XO: 400B by Princeton Instruments, with resolution 20 μm)

spot size is 140 μm x 220 μm (FWHM). In Fig.3 right, we present the XUV spot of the 25th harmonic generated in Ar. In this case, the CG G1200 grating was used, with a slit aperture of 200 μm . The obtained spot size is 220 μm x 120 μm (FWHM). The OPA beam focusing can be adjusted in order to obtain a spot approximately twice as big. This ensures a homogeneous excitation of the probed area. The energy density of the IR-UV at the interaction point has been estimated to be of the order of 10 mJ/cm^2 .

Two typical spectra, obtained using Ar and Ne for harmonic generation, are shown in Fig. 5.5.

In agreement with existing literature, use of Ar produced harmonics in the photon energy range 20-54 eV, with a peak of about $1 \cdot 10^8$ photons/pulse at about 40 eV (25th harmonic). Using Ne, the plateau region moves towards higher energies, but with significantly reduced efficiency. In table 2 the generation efficiencies for the two gases at different harmonic orders are reported.

Table 5.3: Generation efficiency after the monochromator with Ar and Ne. Selected harmonic orders are reported. In particular, the 35th (54,25 eV) and 41st (63,55 eV) harmonics generated with Ne, which correspond to the $M_{2,3}$ edges of Fe and Ni, respectively.

	15 th	23 rd	35 th	41 th	51 th
	ph/pulse	ph/pulse	ph/pulse	ph/pulse	ph/pulse
Ar	$3.4 \cdot 10^7$	$1.1 \cdot 10^8$	$2.2 \cdot 10^6$	negligible	negligible
Ne	$7.1 \cdot 10^5$	$2.2 \cdot 10^6$	$1.5 \cdot 10^6$	$1.1 \cdot 10^6$	$5.6 \cdot 10^5$

In the following two sections, we report the results of two pump-

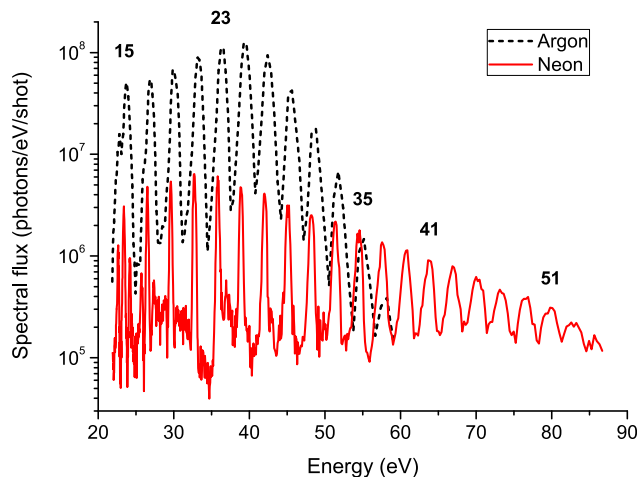


Figure 5.5: Harmonic spectra generated in Ar and Ne using laser pulses with energy $\simeq 2$ mJ, duration 40 ± 2 fs (after transport to the generation chamber), wavelength = 805 nm and repetition rate = 5 kHz. Some of the harmonics have been highlighted (see also Table 5.3). The spectra have been acquired with a NIST-calibrated Al photodiode, placed at the exit of the monochromator. The monochromator slits aperture was set to $100 \mu\text{m}$, in order to get a spectral resolution of about 0.05 nm.

probe experiments carried out to characterize the source performance. The experiment described in Section 5.1.3 aimed at measuring the duration of harmonic pulses transmitted by the monochromator. The experiment described in Section 5.1.4 aimed at demonstrating the possibility of using CITIUS for studies of ultra-fast dynamics.

5.1.3 Characterization of harmonic pulse duration

The pulse duration of HHG XUV pulses has been measured by means of an experiment based on LAPE (Laser Assisted Photoelectric Effect). This technique, described in detail in [137, 138], is based on the cross correlation of XUV and IR photons. In essence, the primary photo-electron spectrum resulting from XUV ionization of a target gas (Kr, in the case under scrutiny) is modified if the ionization takes place in the presence of a high-intensity laser pulse: the absorption and emission of laser photons gives rise to so-called sidebands in the photoelectron spectrum. The amplitude of the sidebands as a function of the delay between the XUV and IR pulses provides a cross-correlation signal from which one can extract the

duration of XUV pulses.

Our detection set-up was based on a hemispherical electron energy spectrometer (VG Scienta, SES-200) [38]. The choice of Kr for the LAPE experiment was mainly dictated by instrumental reasons. The 15th harmonic (23.2 eV) has sufficient energy to ionize the Kr 4p levels and is efficiently transmitted by all monochromator gratings in OPG configuration, with high-enough resolving power to fully resolve the $4p_{3/2}$ and $4p_{1/2}$ photo-electron lines. Additionally, the high photoionization cross section of Kr 4p electrons grants fast acquisition times. The laser pulse duration was carefully measured using a commercial autocorrelator and set at its minimum value, i.e., about 40 ± 2 fs after transport in the experimental chamber. The IR pulse was attenuated down to 80-100 mW in order to avoid saturation effects. Figure 5.6 shows a series of Kr 4p photo-electron spectra (horizontal axis), as a function of the delay between XUV and IR pulses (vertical axis). The measurements have been performed using the G200 grating (see Table 5.2). The two main photoelectron peaks, generated by the $4p_{3/2}$ and $4p_{1/2}$ states, have kinetic energies of 8.6 and 9.3 eV respectively. The presence of these peaks is due to a single-photon photoionization process and does not depend on the presence of the IR pulse. When the two pulses are temporally overlapped, two sidebands appear, corresponding to absorption and emission of one IR photon: these sidebands are at 7.8 and 10.8 eV for the $4p_{3/2}$ state, and at 7.1 and 10.1 eV for the $4p_{1/2}$ state. The intensity of each sideband as a function of the delay is the convolution of the XUV and IR pulses. The duration of the XUV pulse is obtained by deconvolving the IR signal from the Gaussian fit of the measured intensity. The black dots represent the temporal profile of the sideband at 10.8 eV; the solid line is a Gaussian fit.

The extracted pulse durations are reported in Table 5.4. Results clearly demonstrate the possibility to maintain a temporal resolution of few tens of femtoseconds after monochromatization using the OPG configuration.

Table 5.4: Measured pulse durations of the 15th harmonic (23.2 eV), transmitted by OPG gratings.

Grating	Pulse duration (fs)
G420	23 ± 1.2
G400	35 ± 1.7
G600	35 ± 1.9

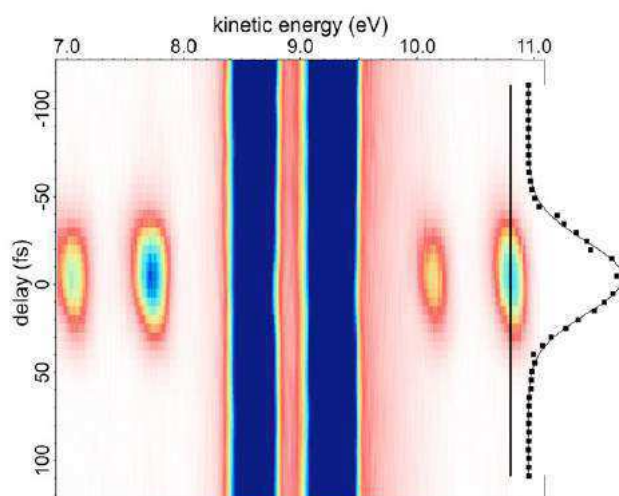


Figure 5.6: Kr 4p photo-electron spectra obtained by overlapping the XUV (pump) and IR (probe) beams. In this case, the XUV beam (15th harmonic of the fundamental) was monochromatized by the G200 grating (OPG geometry, see Table 1). The black dots represent the integrated intensity of the sideband at 10.8 eV, as a function of the pump-probe delay; the solid line is a Gaussian fit. The pulse duration is obtained by deconvolving the contribution of the IR pulse from the measured profile.

5.1.4 Ultrafast demagnetization of permalloy

In this section, we report the results of a pump-probe experiment demonstrating the possibility of using CITIUS to study the ultrafast dynamics of selected chemical species, with a temporal resolution of few tens of femtoseconds.

The spectral range covered by CITIUS includes the $M_{2,3}$ thresholds of transition metals (54.25 eV, i.e., the 35th harmonic of the fundamental, see Table 5.3), making CITIUS an appealing source for the study of magnetic materials. As a proof-of-principle application, we measured the demagnetization of a 100 nm thick permalloy film (Fe₂₀Ni₈₀), using X-ray resonant magnetic scattering [139, 140] in pump-probe configuration.

The experiment was performed using the IRMA reflectometer [141]. The instrument permits to precisely adjust the angles between the sample surface and the incoming/reflected XUV beam. Three photodiodes and one channel electron multiplier are mounted on the detector arm. By means of a horseshoe electromagnet, it is possible to apply a variable magnetic field up to ± 1500 Oe, parallel to the sample surface. The scattering experiment was conducted in

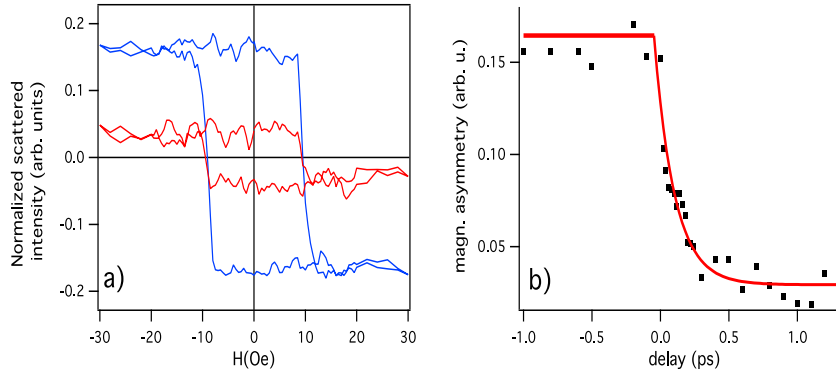


Figure 5.7: a) Hysteresis loops measured at the 35th harmonic of the fundamental ($M_{2,3}$ thresholds of transition metals) for HHG pulse arriving 1 ps before (blue line) and 10 ps after (red line) the IR pump pulse. b) Pump-probe delay dependency of the magnetic asymmetry ratio at saturation (dots) and exponential decay fit. The magnetization quenching is about 80 % after 0.5 ps and the characteristic decay time is 0.21 ± 0.02 ps.

a transverse MOKE-like configuration [142]. In this configuration, using p-polarized XUV light, one is sensitive to the magnetization component perpendicular to the scattering plane. Moreover, choosing the incoming/scattering angle close to the Brewster condition (about 45° at 54 eV), the magnetization contrast is maximized with respect to the (strongly suppressed) non-magnetic scattered background, thus improving the signal-to-noise ratio of the measurement.

We have measured the magnetic hysteresis loop at the Fe $M_{2,3}$ edge, as a function of the delay between the transmitted IR beam (pump) and the XUV pulse (probe). Figure 5.7a) shows the hysteresis loop when the XUV pulse arrives on the sample 1 ps before (blue curve) and 1 ps after (red curve) the IR pulse. The plots are normalized to the average scattered intensity. The magnetic asymmetry ratio is defined as $(I_+ - I_-)/(I_+ + I_-)$, where I_+ and I_- denote the intensities of the reflected light as the externally applied magnetic field is reversed in direction. In Figure 5.6b), the asymmetry ratio at saturation is plotted as a function of the pump-probe delay. Data show the ultrafast demagnetization of the Fe atoms of the sample. Almost 80 % of the magnetization is dissipated 0.5 ps after the sample has been illuminated with the IR pulse. The data have been fitted with an exponential decay curve, indicating a characteristic demagnetization time of 0.21 ± 0.02 ps. Despite the modest scientific interest of this particular sample, which has been already investigated in detail by other groups [143], these re-

sults demonstrate that our apparatus is capable of measuring the ultrafast magnetization dynamics of selected chemical species, with a resolution of few tens of femtoseconds.

5.2 Low Density Matter beamline at FERMI

5.2.1 Introduction

The Low Density Matter beamline (LDM) is an instrument for experiments involving molecular beams in combination with XUV/soft-X-ray radiation produced by the FERMI FEL; the layout of FERMI and the beamlines is reported in Fig. 5.8. The photon beam paths of the two sources merge in the safety hutch and are transported to the experimental section via a common set of optics. The beamline was commissioned in 2012 and is undergoing rapid development. A modular end-station [144] for the production of supersonic beams of atoms, molecules or clusters has been installed.

5.2.2 Photon transport system

The photon analysis, delivery, and reduction system (PADReS) consists of the section of the machine from the exit of the undulators to the endstations. A set of plane mirrors (PM1a and PM1b serving FEL-1; PM2a serving FEL-2) is installed in the so-called safety hutch. Each FEL source has its own beam diagnostics and beam conditioning instruments, such as the intensity and beam position monitors, beam defining apertures, and gas absorber [145]. At the end of the safety hutch the two photon beam paths enter the PM1b chamber (see Fig. 5.8), where one or the other can be selected.

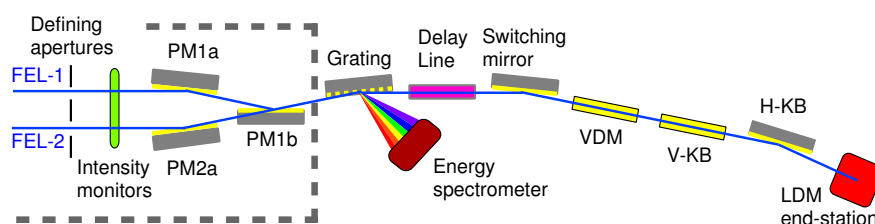


Figure 5.8: The photon beam transport and diagnostics system of FERMI. The two FEL undulator lines are visible on the left, inside the safety hutch (dashed line). The LDM endstation is in the bottom-right corner. The parameters of the optics are reported in Table 5.5.

Outside the safety hutch, the energy spectrometer PRESTO [146] records the spectrum of each pulse by diffracting and detecting

Table 5.5: Parameters of the optics; d : distance from the nominal source points (FEL-1/FEL-2); w : width; ℓ : length; θ : grazing incidence angle. PM2a and SW have two coatings, each covering half the width of the mirror, and their position can be adjusted sidewise to use one or the other coating. Orientation (H, V) refers to the deflection plane.

Mirror	d (m)	$w \times \ell$ (mm \times mm)	θ ($^\circ$)	Coating	Shape (orientation)
PM1a	48.1/-	20 \times 400	2.5	Graphite	plane (H)
PM1b	54.3/-	20 \times 250	5	Graphite	plane (H)
PM2a	-/41.4	20 \times 300	2.5	Graphite/Ni	plane (H)
PRESTO-LE	57.5/49.8	20 \times 250	2.5	Graphite	VLS plane grating (H)
PRESTO-HE	57.5/49.8	20 \times 250	2.5	Au	VLS plane grating (H)
SW	77.5/69.9	25 \times 480	2	Graphite/Ir	plane (H)
VD	90.0/82.3	20 \times 390	2	Au	plane (V)
H-KB	95.6/87.9	40 \times 400	2	Au	active (V)
V-KB	96.1/88.5	40 \times 400	2	Au	active (H)

1–2% of the total intensity, while delivering the essentially unperturbed beam downstream. It employs two plane substrates, ruled as gratings only in their central parts (60 mm over a total length of 250 mm). The rulings have a variable line spacing along the longitudinal direction (along the photon beam propagation direction) in order to focus the diffracted radiation onto a movable two-dimensional detector that tracks the focal curve. A computer calculates the one dimensional spectrum from the image, as well as the central wavelength, bandwidth, horizontal and vertical projection on a shot-by-shot basis, and this information can be stored with the experimental data. The two gratings cover the whole wavelength range of FERMI as provided by FEL-1 (low energy grating, LE) and FEL-2 (high energy grating, HE).

A split-and-delay line (AC/DC: AutoCorrelator/Delay Creator) is installed after the spectrometer, for pump and probe experiments. It is based on the splitting and subsequent recombination of the incoming wavefront after passing through two different branches (one of variable length, the other of fixed length), by means of eight Au-coated plane mirrors, four for each path. In the variable length branch, two mirrors move on 900 mm-long linear guides with an accuracy of 10 μ m, as measured by an optical encoder. Changing the positions of these two mirrors produces a difference of the two path lengths and introduces a time delay variable between -1.5 ps and 30 ps in steps of 0.3 fs.

The mirrors of the two branches operate with two different grazing incidence angles: 2° in the fixed branch, 3° in the variable branch. This difference results in different transmission coefficients of the light, which have been calculated considering perfect mirrors (flat and free of contamination). For the fixed-length branch the transmission of the 4 mirrors, in the wavelength range from 4 to 100 nm is about 80% for s polarized radiation and about 50–65% for p polarization. The transmission of the other branch is about 70% for s polarization and about 30–50% for p polarization. For selected wavelength ranges, the length of each branch can be further extended by inserting 4 more multilayer (ML) mirrors operating at 45° incidence, thus introducing an additional delay variable between 0.3 ns and 1.3 ns. The type of multilayers must be chosen according to the experimental needs; we note that even at their design wavelength, four additional ML mirrors reduce considerably the light transmission. Seven out of eight mirrors have motorized pitch and roll movements, providing fine control of the alignment and the attainment of very good spatial overlap of the half beams in the experimental stations. Overlap is visually evaluated by inspecting the two beams on a YAG screen at the center of the end-station, and later optimized by maximizing a suitable experimental signal. It is possible to filter the radiation independently in the two branches of the AC/DC unit: before the recombination mirror, an easily accessible section that can host three filters for each branch gives users the possibility of mounting filters suited to their experimental needs. To install filters from air into vacuum requires a downtime of about twelve hours.

The 3-way switching mirror chamber selects which beamline is in use. The plane switching mirror (SW) serving LDM deflects the beam in the horizontal direction, and has a dual coating (graphite and iridium, each covering half the width of the mirror), to maximize the reflectivity for FEL-1 and FEL-2, respectively. Downstream of the switching mirror, the beam undergoes three further reflections: from a vertical deflecting mirror (VD) and from two Kirkpatrick-Baez (K-B) mirrors.

The K-B system consists of two thin plane mirrors clamped at their sides and bent via two mechanical pushers acting independently on their respective clamps in order to attain the best elliptical profile as shown in Figure 5 of Reference [147]. The Kirkpatrick-Baez configuration [148], decouples the horizontal and vertical focusing. The active shape allows users to finely adjust the focal length, making provision for the fact that the position of the last undulator (i.e., the nominal source points) of FEL-1 and FEL-2 differ by ~ 7 m.

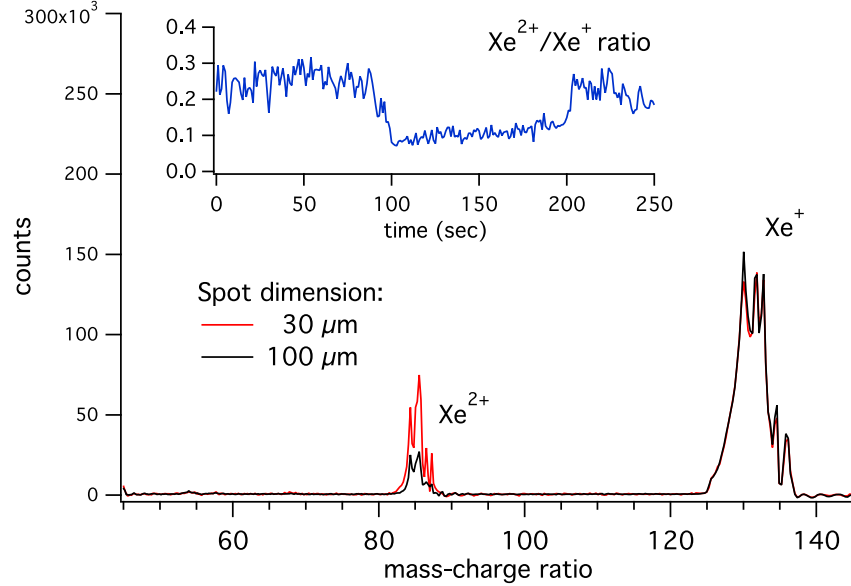


Figure 5.9: Ion time-of-flight (TOF) mass/charge spectra of Xe taken at $\lambda = 52.22$ nm (23.74 eV) for different focusing conditions. Each spectrum is a sum over several spectra; all spectra have been recorded with the same FEL intensity. In the inset (blue line) we show the $\text{Xe}^{2+}/\text{Xe}^+$ intensity ratio as a function of time while changing the curvature of the K-B mirrors.

Likewise, the K-B active optics can compensate and correct astigmatism and defocusing effects originating from non-ideal profiles of the preceding plane mirrors, that are discussed in the next section.

5.2.3 Commissioning and present status of the beamline

During the beamline construction period, commissioning measurements were performed with a prototype end-station equipped with a Velocity Map Imaging/ion time-of-flight spectrometer (VMI/TOF). The original VMI spectrometer and its further improvements have been described previously[149].

One of the test measurements is shown in Fig. 5.9. At the time of the commissioning, the FEL pulse length was 120 fs and the energy per pulse was $60 \mu\text{J}$. In order to test the capabilities of the adjustable focusing system we measured ion TOF spectra of Xe atoms exposed to FEL pulses, observing charge states indicative of multi-photon absorption; the intensity ratio of different charge states as a function of time while changing the bending of the K-B mirrors (inset to Fig. 5.9) is a good indicator of the reproducibility of the focusing

system for small curvature changes. While highly charged states of Xe obtained upon FEL irradiation have been reported in the literature [150] for photon energies within the $4d \rightarrow \epsilon f$ giant resonance (93 eV), to our knowledge only sequential double ionization of Xe has been reported at 23.0 and 24.3 eV [151], at average intensities of $2 - 3 \times 10^{13}$ W/cm².

The LDM beamline now features a modular end-station accommodating a broad range of detectors and systems for producing targets. The combined capabilities of the photon source (high-brilliance, short-pulse length, variable polarization, coherence), photon transport (variable-focusing optics) and endstation allow the investigation of many targets, such as very dilute systems, matter under extreme irradiation conditions (multiple electronic excitation, multiple ionization, Coulomb explosion, non-linear optics), and dichroism. The split-and-delay line described above, as well as a synchronized optical laser [152] allow time-resolved experiments with different combinations of femtosecond pulses.

Chapter 6

Conclusions and perspectives

The argument of the present thesis was the experimental investigation experimentally the electronic structure of molecules by means of advanced spectroscopical methods. The goal was to start with the characterization of the molecules in the simplest form possible - as isolated systems - and afterwards increasing the complexity. Possible applications of all this work are illustrated here, as well as completely new experiments that originated from the results of this thesis, like the continuation of recent experiments in the gas of even in the condensed phase.

In the study of the short chain thiophenes in gas phase, by using oligomers with a varying number of monomer units it was possible to evaluate the effect of increasing conjugation length as well as to estimate the properties of more complex polymers. In particular, the initial investigation continued with 1,3-di- (thiophen-2-yl)benzo[*c*]thiophene (DTBT, Fig. 6.1) a synthetic system produced by our collaborators [153] and, as expected, a different reactivity was been displayed with respect to the reference compound 3T. Guarnaccio *et al.* performed also a study of DTBT and the brominated analogue Br-DTBT-Br (Fig. 6.1) deposited on a metallic surface [154].

The experimental and theoretical work on pyridines is an important step towards the inclusion of vibrational effects in the analysis of NEXAFS, whose inclusion has proven to be necessary for an accurate description of the experiment. It is worth to remind that vibrational effects were also often referred to in the discussion about the thiophenes absorption spectra, especially for 1T molecule. In pyridines it was found that the vibrations are responsible for strong intensity redistribution and we believe that their treatment can be extremely useful in the analysis of analogous molecules.

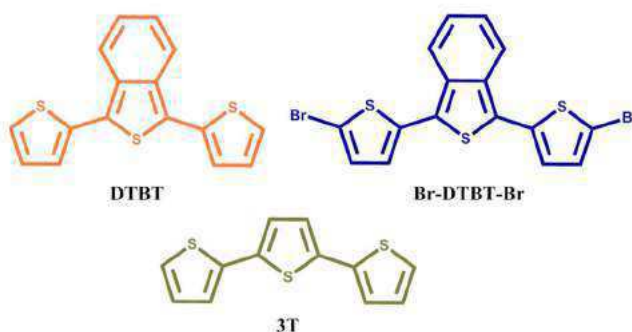


Figure 6.1: Molecular structures of 1,3-di(thiophen-2-yl)benzo[*c*]-thiophene (DTBT), 1,3-bis(4,5-dibromothiophen-2-yl)benzo[*c*]-thiophene (Br-DTBT-Br), and 2,2':5',2'-terthiophene (3T) oligothiophenes.

The electronic structure of the biphenylene molecule was studied. This molecule has a pronounced anti-aromatic character, that is proven by the MO nodal planes shown in 3.2. This character is due to a not completely delocalization of valence electron over the whole molecule and it was evidenced in the analysis of the PES spectra. The detailed PES and NEXAFS characterization was preliminary to the study of the molecular architecture of biphenylene deposited on Cu(111); it was found to be oriented almost flat when directly on the substrate, in a low coverage deposition, while standing when at the top of a thicker film. The investigation of the arrangement and the self-organization of biphenylene films deserves further experimental and theoretical efforts. Lüder *et al.* [11], in fact, performed a theoretical characterization of the electronic and optical properties of the 2D network biphenylene carbon and found excitonic features of great interest for solar energy and quantum information technology.

The electronic structure of metal Pcs was also characterized. FePc and MnPc were studied and compared to the reference molecule H₂Pc. When a class of molecules is chosen for specific applications the understanding of how the outermost orbitals are formed and the influence of different metal atoms on their electronic structure is of primary importance. Moreover, two consecutive investigations were performed on adsorption of LuPc₂ onto the reactive Si(100)2×1. The adsorption mechanisms are, as expected, very different between the clean and the passivated Si(100)2×1 surface, due to the very different chemical reactivities of the two surfaces. The changes in the electronic properties of LuPc₂ in the molecular architectures were also studied. The results by photoemission and absorption spectroscopies are also confirmed by STM [84].

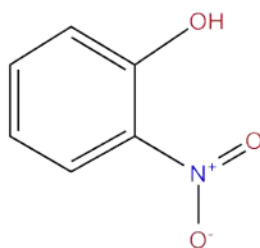


Figure 6.2: Molecular structure of ortho-nitrophenol ($C_6H_5NO_3$).

6.1 Experiments with novel light sources

The advent of LDM and CITIUS has significantly changed the opportunities for experimentalists in atomic and molecular physics to measure ultrafast dynamics after photoexcitation. These two novel XUV/X-ray short pulse light sources can be focused onto an atomic or molecular target, a series of new phenomena can be investigated.

Besides the well-known advantages of TRPES, the use of probe photon energies in the VUV-XUV region produced by HHG is a recently emerging approach which is highly useful for the study of ultrafast non-adiabatic processes and spin-orbit coupling in polyatomic molecules. Indeed, VUV-XUV light produced by HHG allows direct single photon ionization of low-lying molecular orbitals as well as the ionization of photoreaction products, with high temporal resolution. Furthermore, VUV-XUV ionization greatly reduces the difficulties in the interpretation of the experimental results that are encountered when pump-probe experiments are carried out with conventional vis-UV lasers involving multiphoton ionization. Indeed, multiphoton ionization often brings on several drawbacks which smear out the information on the spectra. In the following, one of the first experiments at CITIUS of on gaseous ortho-nitrophenol is described.

Nitrophenols belong to a group of aromatic hydrocarbons playing an important role in chemical reactions in the troposphere [155]. The photoexcitation of (o-NP, shown in Fig. 6.2) leads to release of nitrous acid and the photolysis of o-NP is considered a non-negligible daytime source of nitrous acid in the atmosphere and consequently of hydroxyl-radicals formed by the photolysis of HNO_2 [156].

In comparison with other nitrophenols, the orthoisomer, is endowed to some extent with different photophysical and photochemical properties, due to the presence of an intramolecular hydrogen bond, which is relevant for excited-state proton-transfer reactions. The gas-phase ultraviolet absorption spectrum of o-NP above 250

nm consists of two broad bands, centered at about 338 and 260 nm that can be assigned to $S_1 \leftarrow S_0$ and $S_4 \leftarrow S_0$ electronic transitions. Both transitions are of $\pi - \pi^*$ type and involve a charge transfer from the phenyl ring to the NO_2 substituent. The early stage photophysical and photochemical processes taking place after excitation have not been clearly elucidated so far.

We made use of UV pump - VUV probe time-resolved photoelectron spectroscopy (TRPES) methodology. Ultrafast vacuum ultraviolet (VUV) radiation at 53,7 nm ($h\nu = 23.1$ eV) from the CITIUS High Harmonic Generation (HHG) source] was employed to probe the excited state dynamic of o-NP prepared by a fs-laser pulse at 268 nm. As a matter of fact, from a recent vis-UV TPRES experiment [157] on o-NP excited in the S_1 state and probed with 400 nm radiation, the lifetime of the S_1 excited state was obtained. It was suggested that two processes may contribute to the measured time constant: an $S_1 \rightarrow S_0$ relaxation via a conical intersection (CI) and an ultrafast intersystem crossing (ISC) into a triplet manifold. We will show in the following that TRPES by high harmonic pulses allowed to directly measure the timescales of the processes contributing to the deactivation of the S_1 state, and to obtain other new and valuable experimental information.

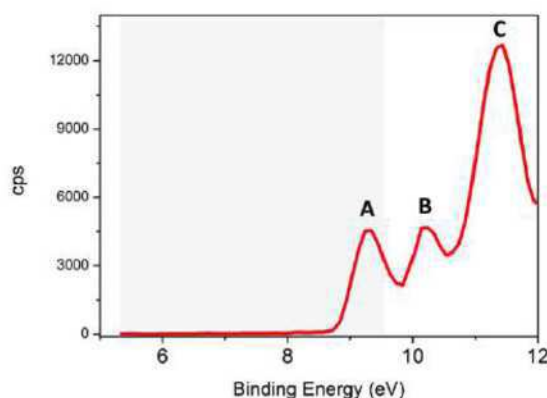


Figure 6.3: Valence photoelectron spectrum of o-NP, heated at 35°C , taken at $h\nu=23.2$ eV (15^{th} HH). Pump probe spectra have been measured in the grey marked region.

All TRPES experiments have been performed at the CITIUS light source facility. The laser system Legend Elite Duo was operated at 5 kHz and generating pulses of about 3.1 mJ, with a duration of about 35 fs, centered at 805 nm (see 5.1 for details). Two thirds of this energy was used to generate the VUV probe pulses

(about at 23.1 eV) by laser-induced high-order harmonic generation (HHG) in gas (Ar). The remaining fraction was used to produce the UV pump pulses (about 25 μJ at 268 nm) by frequency tripling of the 805 nm radiation. The gas phase experimental end station ULLA (Sec. 2.2.3) was coupled to the CITIUS light source. Ortho-nitrophenol (> 99% by Sigma Aldrich) was evaporated in a temperature-controlled reservoir (35°C) and continuously expanded into the chamber through a pinhole. Photoelectron spectra were acquired at time delays spanning from -1 to 4 ps with steps of either 50 or 100 fs.

Initially, the photoelectron spectra arising by the pump beam and by the probe beam were acquired. No photoelectron signals originating from multiphoton ionization processes due to the pump laser at 268 nm were detected in the 5-12 eV range. Fig. 6.3 shows the photoelectron spectrum of *o*-NP recorded by using only the 15th harmonic pulse at 23.1 eV. In the 5-12 eV range, three main bands (A, B, C in Fig. 6.3), that are comparable with those measured by He(I) [158] and synchrotron radiation [159] photoelectron spectroscopy. The first two bands (A at 9.21 and B at 10.17 eV) originate mainly from the removal of electrons from delocalized π orbitals. Band C is centered at 11.37 eV and can be interpreted as originating from the overlap of three states corresponding to the removal of electrons from MOs localized mainly on the σ and π_{NO} molecular orbitals.

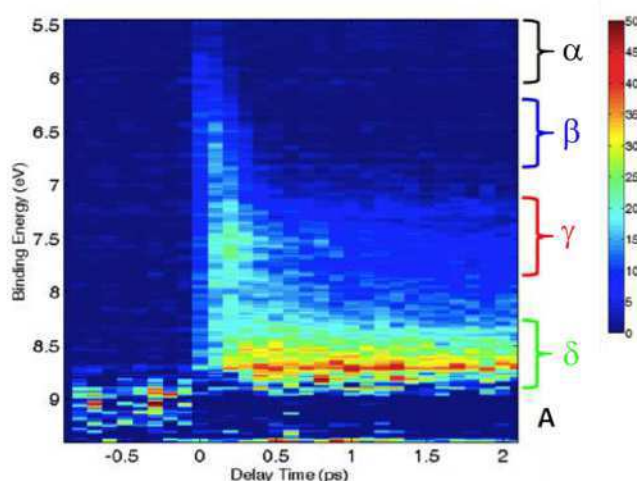


Figure 6.4: TRPES 2D-map resulting from *o*-NP excited by a fs-pump laser pulse at 268 nm, and probed by 23.2 eV VUV photons. The ionization energy is given by subtracting the measured photoelectron energy from the energy of just the ionizing probe photon.

Fig. 6.4 shows a 2D map of the integrated intensity of the TRPES signal in the 5.4-9.3 eV ionization energy range (13.9-17.8 eV kinetic energy range), resulting from excitation by a fs 268 nm pulse (pump) and ionization with the 15th harmonic pulse at 23.1eV (probe) in the pump-probe delay range: -900 ÷ 2100 fs and with steps of 100 fs. Since the signal from the non-excited o-NP molecules obscures the time dependence of the spectrum, the signal arising from negative (-900 fs) pump-probe delays was subtracted from the total intensity. At positive times, one can observe in Fig. 6.4 the rise of several bands which are energetically broadened. We can identify four zones that we call α (5.6- 6.1eV), β (6.1-6.9 eV), γ (7.2-7.9 eV), and δ (8.3-8.9 eV).

List of papers

Papers included in this thesis

Here I provide a list of the publications that have been included in this thesis. The whole work presented in the papers has been a collaboration with other coauthors. For all the publications listed here I actively made my contribution to the discussion, preparation and collection of the experimental data. In paper **II** I took part to the writing, while for the ones in which I am first or corresponding author (**I** and **VII**) I have written the manuscripts.

I Study of the electronic structure of short chain oligothiophenes C. Grazioli, O. Baseggio, M. Stener, G. Fronzoni, M. de Simone, M. Coreno, A Guarnaccio, S. Orlando, A. Santagata, *Journal of Chemical Physics* **146**, 054303 (2017); <http://dx.doi.org/10.1063/1.4974841>

II Electronic structure investigations of biphenylene films R. Totani, C. Grazioli, T. Zhang, I. Bidermane, J. Lüder, V. Lanzilotto, M. de Simone, M. Coreno, B. Brena, L. Lozzi and C. Puglia, *Journal of Chemical Physics* **146**, 054705 (2017); <http://dx.doi.org/10.1063/1.4975104>

III Vibrationally resolved NEXAFS at C and N K-edges of pyridine, 2-fluoropyridine and 2,6-difluoropyridine: A combined experimental and theoretical assessment A. Baiardi, M. Mendolicchio, V. Barone, G. Fronzoni, G. A. Cardenas Jimenez, M. Stener, C. Grazioli, M. de Simone, and M. Coreno, *Journal of Chemical Physics* **143**, 204102 (2015); <http://dx.doi.org/10.1063/1.4935715>

- IV Atomic Contributions to the Valence Band Photoelectron Spectra of Metal-free, Iron and Manganese Phthalocyanines** I. Bidermane, I.E. Brumboiu, R. Totani, C. Grazioli, M.N. Shariati-Nilsson, H.C. Herper, O. Eriksson, B. Sanyal, B. Ressel, M. de Simone, L. Lozzi, B. Brena, C. Puglia, *Journal of Electron Spectroscopy and Related Phenomena* **205**, 92-97 (2015); <http://dx.doi.org/doi:10.1016/j.elspec.2015.09.004>
- V Characterization of Gas Phase of Iron Phthalocyanine with X-ray Photoelectron and Absorption Spectroscopies** I. Bidermane, R. Totani, C. Grazioli, M. de Simone, M. Coreno, A. Kivimaäki, J. Åhlund, L. Lozzi, C. Puglia, *Physica Status Solidi (B) Basic Research* **252**, 1259-1265 (2015) <http://dx.doi.org/doi:10.1002/pssb.201451147>
- VI The electronic characterization of biphenylene - Experimental and theoretical insights from core and valence level spectroscopy** J. Lüder, M. de Simone, R. Totani, M. Coreno, C. Grazioli, B. Sanyal, O. Eriksson, B. Brena, C. Puglia, *Journal of Chemical Physics* **142**, 074305 (2015); <http://dx.doi.org/10.1063/1.4907723>
- VII The Low Density Matter (LDM) beamline at FERMI: Optical layout and first commissioning** C. Svetina, C. Grazioli, N. Mahne, L. Raimondi, C. Fava, M. Zangrando, S. Gerusina, M. Alagia, L. Avaldi, G. Cautero, M. de Simone, M. Devetta, M. Di Fraia, M. Drabbels, V. Feyer, P. Finetti, R. Katzy, A. Kivimäki, V. Lyamayev, T. Mazza, A. Moise, T. Möller, P. O’Keeffe, Y. Ovcharenko, P. Piseri, O. Plekan, K. C. Prince, R. Sergo, F. Stienkemeier, S. Stranges, M. Coreno and C. Callegari, *Journal of Synchrotron Radiation* **22**, 538-543 (2015) <http://dx.doi.org/doi:10.1107/S1600577515005743>
- VIII Elucidating the 3d electronic configuration in manganese phthalocyanine** I. E. Brumboiu, R. Totani, M. de Simone, M. Coreno, C. Grazioli, L. Lozzi, H. C. Herper, B. Sanyal, O. Eriksson, C. Puglia, B. Brena, *Journal of Physical Chemistry A* **118**, 927-932 (2014) <http://dx.doi.org/10.1021/jp4100747>

Papers not included in this thesis

- IX Document Combined theoretical and experimental study of the valence, Rydberg and ionic states of fluorobenzene** M. H. Palmer, T. Ridley, S. V. Hoffmann, N. C. Jones, M. Coreno, M. de Simone, C. Grazioli, T. Zhang, M. Biczysko, A. Baiardi, and K. A. Peterson, *Journal of Chemical Physics* **144**, 204305 (2016); <http://dx.doi.org/doi:10.1063/1.4949548>
- X Combined theoretical and experimental study of the valence, Rydberg, and ionic states of chlorobenzene** M. H. Palmer, T. Ridley, S. V. Hoffmann, N. C. Jones, M. Coreno, M. de Simone, C. Grazioli, T. Zhang, M. Biczysko, A. Baiardi, and K. A. Peterson, *Journal of Chemical Physics* **144**, 124302 (2016); <http://dx.doi.org/doi:10.1063/1.4944078>
- X1 Interpretation of the photoelectron, ultraviolet, and vacuum ultraviolet photoabsorption spectra of bromobenzene by ab initio configuration interaction and DFT computations** M. H. Palmer, T. Ridley, S. V. Hoffmann, N. C. Jones, M. Coreno, M. de Simone, C. Grazioli, T. Zhang, M. Biczysko, A. Baiardi and K. Peterson, *Journal of Chemical Physics* **143**, 164303 (2015); <http://dx.doi.org/10.1063/1.4933419>
- XII Two-photon resonant excitation of interatomic coulombic decay in neon dimers** A. Dubrouil, M. Reduzzi, M. Devetta, C. Feng, J. Hummert, P. Finetti, O. Plekan, C. Grazioli, M. Di Fraia., V. Lyamayev, A. La Forge, R. Katzy, F. Stienkemeier, Y. Ovcharenko, M. Coreno, N. Berrah, K. Motomura, S. Mondal, K. Ueda, K. C. Prince, C. Callegari, A. I. Kuleff, Ph. V. Demekhin and G Sansone, *Journal of Physics B: Atomic, Molecular and Optical Physics* **48**, 204005 (2015); <http://dx.doi.org/10.1088/0953-4075/48/20/204005>
- XIII Interpretation of the vacuum ultraviolet photoabsorption spectrum of iodobenzene by ab initio computations** M. H. Palmer, T. Ridley, S. V. Hoffmann, N. C. Jones, M. Coreno, M. de Simone, C. Grazioli, M. Biczysko, A. Ba-

iardi, and P. Limão-Vieira, *Journal of Chemical Physics* **142**, 134302 (2015) <http://dx.doi.org/10.1063/1.4916121>

XIV The ionic states of iodobenzene studied by photoionization and ab initio configuration interaction and DFT computations M. H. Palmer, T. Ridley, S. V. Hoffmann, N. C. Jones, M. Coreno, M. de Simone, C. Grazioli, M. Biczysko, and A. Baiard, *Journal of Chemical Physics* **142**, 134301 (2015) <http://dx.doi.org/10.1063/1.4916120>

XV Photoionization and Velocity Map Imaging spectroscopy of atoms, molecules and clusters with Synchrotron and Free Electron Laser radiation at Elettra M. Di Fraia, R. Sergo, L. Stebel, D. Giuressi, G. Cautero, M. Tudor, C. Callegari, P. O’Keeffe, Y. Ovcharenko, V. Lyamayev, V. Feyer, A. Moise, M. Devetta, P. Piseri, C. Grazioli, M. Coreno, *Nuclear Instruments and Methods in Physics Research Section B: Beam Interactions with Materials and Atoms* **364**, 16-19 (2015) <http://dx.doi.org/doi:10.1016/j.nimb.2015.07.112>

XVI Magnetism and morphology of Co nanocluster superlattices on GdAu₂/Au(111)-(13x13) A. Cavallin, L. Fernández, M. Ilyn, A. Magaña, M. Ormaza, M. Matena, L. Vitali, J. E. Ortega, C. Grazioli, P. Ohresser, S. Rusponi, H. Brune, and F. Schiller, *Physical Review B* **90**, 235419 (2014) <http://dx.doi.org/doi:10.1103/PhysRevB.90.235419>

XVII Spectrometer for X-ray emission experiments at FERMI free-electron-laser L. Poletto, F. Frassetto, P. Miotti, A. Di Cicco, P. Finetti, C. Grazioli, F. Iesari, A. Kivimaäki, S. Stagira, and M. Coreno, *Review of Scientific Instruments* **85**, 103112 (2014) <http://dx.doi.org/10.1063/1.4898315>

XVIII Novel Collective Autoionization Process Observed in Electron Spectra of He Clusters Y. Ovcharenko, V. Lyamayev, R. Katzy, M. Devetta, A. LaForge, P. O’Keeffe, O. Plekan, P. Finetti, M. Di Fraia, M. Mudrich, M. Krikunova, P. Piseri, M. Coreno, N. B. Brauer, T. Mazza, S. Stranges, C. Grazioli, R. Richter, K. C. Prince, M. Drabbels, C. Callegari, F. Stienkemeier, and T. Möller, *Physical Review Let-*

ters **112**, 073401 (2014) [http://dx.doi.org/doi:10.1103/
PhysRevLett.112.073401](http://dx.doi.org/doi:10.1103/PhysRevLett.112.073401)

Bibliography

- [1] R. P. Feynman. “There’s Plenty of Room at the Bottom”. In: *Engineering and Science* 23 (1960), pp. 22–36 (cit. on p. 1).
- [2] Hyunwook Song et al. “Observation of molecular orbital gating”. In: *Nature* 462.7276 (Dec. 2009), pp. 1039–1043 (cit. on p. 1).
- [3] Martin Fuechsle et al. “A single-atom transistor”. In: *Nat Nano* 7.4 (Apr. 2012), pp. 242–246 (cit. on p. 1).
- [4] David S. Goodsell. *Bionanotechnology - Lessons from Nature*. John Wiley & Sons, Inc., 2004. ISBN: 9780471469575. DOI: [10.1002/0471469572.fmatter](https://doi.org/10.1002/0471469572.fmatter) (cit. on p. 1).
- [5] “The Molecule-Metal Interface”. In: *The Molecule–Metal Interface*. Wiley-VCH Verlag GmbH & Co. KGaA, 2013, pp. I–XIV. ISBN: 9783527653171. DOI: [10.1002/9783527653171.fmatter](https://doi.org/10.1002/9783527653171.fmatter) (cit. on p. 1).
- [6] Amaresh Mishra, Chang-Qi Ma, and Peter Bäuerle. “Functional Oligothiophenes: Molecular Design for Multidimensional Nanoarchitectures and Their Applications”. In: *Chemical Reviews* 109.3 (2009). PMID: 19209939, pp. 1141–1276. DOI: [10.1021/cr8004229](https://doi.org/10.1021/cr8004229) (cit. on p. 3).
- [7] R. J. Kline et al. “Critical Role of Side-Chain Attachment Density on the Order and Device Performance of Polythiophenes”. In: *Macromolecules* 40.22 (2007), pp. 7960–7965. DOI: [10.1021/ma0709001](https://doi.org/10.1021/ma0709001) (cit. on pp. 3, 40).
- [8] Itaru Osaka et al. “High-Lamellar Ordering and Amorphous-Like π -Network in Short-Chain Thiazolothiazole-Thiophene Copolymers Lead to High Mobilities”. In: *Journal of the American Chemical Society* 131.7 (2009). PMID: 19183045, pp. 2521–2529. DOI: [10.1021/ja801475h](https://doi.org/10.1021/ja801475h) (cit. on pp. 3, 40).
- [9] A. T. Balaban, C. C. Rentia, and E. Ciupitu. “Chemical Graphs. 6. Estimation of Relative Stability of Several Planar and Tridimensional Lattices for Elementary Carbon”. In: *Rev. Roum. Chim.* 13 (1968), p. 231 (cit. on pp. 4, 55).
- [10] G. Brunetto et al. “Nonzero Gap Two-Dimensional Carbon Allotrope from Porous Graphene”. In: *The Journal of Physical Chemistry C* 116.23 (2012), pp. 12810–12813. DOI: [10.1021/jp211300n](https://doi.org/10.1021/jp211300n) (cit. on pp. 4, 55).
- [11] Johann Lüder et al. “Many-body effects and excitonic features in 2D biphenylene carbon”. In: *The Journal of Chemical Physics* 144.2 (2016). DOI: [dx.doi.org/10.1063/1.4939273](https://doi.org/dx.doi.org/10.1063/1.4939273) (cit. on pp. 4, 55, 140).

- [12] H. Zandvliet. “Energetics of Si(001)”. In: *Rev. Mod. Phys.* 72.2 (Apr. 2000), pp. 593–602. ISSN: 0034-6861. DOI: [10.1103/RevModPhys.72.593](https://doi.org/10.1103/RevModPhys.72.593) (cit. on p. 4).
- [13] RM Tromp, RJ Hamers, and JE Demuth. “Si(001) dimer structure observed with scanning tunneling microscopy”. In: *Phys. Rev. Lett.* 55.12 (1985), pp. 1303–1306 (cit. on p. 4).
- [14] M J Dresser, P A Taylor, and J T Yates. “THE ADSORPTION AND DECOMPOSITION”. In: *Surf. Sci.* 218 (1989), pp. 75–107 (cit. on p. 4).
- [15] M. C. Hersam, N. P. Guisinger, and J. W. Lyding. “Isolating, imaging, and electrically characterizing individual organic molecules on the Si(100) surface with the scanning tunneling microscope”. In: *J. Vac. Sci. Technol. A* 18.4 (2000), p. 1349. ISSN: 07342101. DOI: [10.1116/1.582352](https://doi.org/10.1116/1.582352) (cit. on p. 4).
- [16] R. Coustel et al. “Pyridine on Si(001)-(2 × 1): Density functional theory simulations compared with spectroscopic measurements”. In: *Phys. Rev. B* 85 (3 2012), p. 035323. DOI: [10.1103/PhysRevB.85.035323](https://doi.org/10.1103/PhysRevB.85.035323) (cit. on pp. 4, 74).
- [17] Tonghui Wang, Yongfu Zhu, and Qing Jiang. “Molecular orientation transformation in initial growth stage of disk-like phthalocyanine during organic vapor deposition process”. In: *Chem. Sci.* 3.2 (2012), p. 528. ISSN: 2041-6520. DOI: [10.1039/c1sc00681a](https://doi.org/10.1039/c1sc00681a) (cit. on p. 4).
- [18] J. F. Moulder et al. *Handbook of X-ray Photoelectron Spectroscopy*. Perkin-Elmer Corporation, Physical Electronics Division, 1992 (cit. on p. 9).
- [19] *NIST data for full tabulation*. URL: <http://physics.nist.gov/PhysRefData/XrayMassCoef/intro.html> (cit. on p. 9).
- [20] S. Hüfner. *Photoelectron spectroscopy: Principles and applications. Third Revised and Enlarged Edition*. Springer-Verlag Berlin Heidelberg New York, 1996 (cit. on pp. 10, 111).
- [21] Y. Luo, H. Ågren, and F. Gel'mukhanov. In: *Journal of Physics B: At. Mol. Opt. Phys.* 27.4169 (1994) (cit. on p. 10).
- [22] H. A. Kramers and W. Heisenberg. “Über die Streuung von Strahlung durch Atome”. In: *Zeitschrift für Physik* 31.1 (1925), pp. 681–708. ISSN: 0044-3328. DOI: [10.1007/BF02980624](https://doi.org/10.1007/BF02980624) (cit. on p. 12).
- [23] J.J. Yeh and I. Lindau. “Atomic subshell photoionization cross sections and asymmetry parameters: 1 ≤ Z ≤ 103”. In: *Atomic Data and Nuclear Data Tables* 32.1 (1985), pp. 1–155. ISSN: 0092-640X. DOI: [dx.doi.org/10.1016/0092-640X\(85\)90016-6](https://doi.org/10.1016/0092-640X(85)90016-6) (cit. on p. 12).
- [24] J.J. Yeh. *Atomic Calculation of Photoionization Cross-sections and Asymmetry Parameters*. Gordon & Breach Science, Publishers, 1993. ISBN: 9782881245855. URL: https://books.google.it/books?id=_aK1kQEACAAJ (cit. on pp. 12, 93).
- [25] J. W. Cooper. “Photoelectron-angular-distribution parameters for rare-gas subshells”. In: *Phys. Rev. A* 47 (3 1993), pp. 1841–1851. DOI: [10.1103/PhysRevA.47.1841](https://doi.org/10.1103/PhysRevA.47.1841) (cit. on p. 12).

- [26] J. Stöhr. *NEXAFS spectroscopy*. Springer Series in Surface Science, 1992 (cit. on pp. 14, 16, 24, 25, 67).
- [27] J.G. Chen. “NEXAFS investigations of transition metal oxides, nitrides, carbides, sulfides and other interstitial compounds”. In: *Surface Science Reports* 30.1 (1997), pp. 1–152. ISSN: 0167-5729. DOI: [10.1016/S0167-5729\(97\)00011-3](https://doi.org/10.1016/S0167-5729(97)00011-3) (cit. on p. 14).
- [28] P. Hohenberg and W. Kohn. “Inhomogeneous Electron Gas”. In: *Phys. Rev.* 136 (3B 1964), B864–B871. DOI: [10.1103/PhysRev.136.B864](https://doi.org/10.1103/PhysRev.136.B864) (cit. on p. 17).
- [29] R. De Francesco, M. Stener, and G. Fronzoni. “Theoretical Study of Near-Edge X-ray Absorption Fine Structure Spectra of Metal Phthalocyanines at C and N K-Edges”. In: *The Journal of Physical Chemistry A* 116.11 (2012), pp. 2885–2894. DOI: [10.1021/jp2109913](https://doi.org/10.1021/jp2109913) (cit. on pp. 18, 72).
- [30] Settimio Mobilio, Federico Boscherini, and Carlo Meneghini. *Synchrotron radiation: basics, methods and applications*. Berlin: Springer, 2014. URL: <https://cds.cern.ch/record/1752603> (cit. on p. 20).
- [31] K Wille. “Synchrotron radiation sources”. In: *Reports on Progress in Physics* 54.8 (1991), p. 1005 (cit. on p. 21).
- [32] K. C. Prince et al. “The gas-phase photoemission beamline at Elettra”. In: *Journal of Synchrotron Radiation* 5.3 (1998), pp. 565–568. DOI: [10.1107/S090904959800065X](https://doi.org/10.1107/S090904959800065X) (cit. on p. 22).
- [33] R.R. Blyth et al. “The high resolution Gas Phase Photoemission beamline, Elettra”. In: *Journal of Electron Spectroscopy and Related Phenomena* 101–103 (1999), pp. 959–964. DOI: [dx.doi.org/10.1016/S0368-2048\(98\)00381-8](https://doi.org/dx.doi.org/10.1016/S0368-2048(98)00381-8) (cit. on p. 22).
- [34] R. Nyholm et al. “Beamline {I311} at MAX-LAB: a VUV/soft X-ray undulator beamline for high resolution electron spectroscopy”. In: *Nuclear Instruments and Methods in Physics Research Section A: Accelerators, Spectrometers, Detectors and Associated Equipment* 467–468, Part 1 (2001). 7th Int.Conf. on Synchrotron Radiation Instrumentation, pp. 520–524. ISSN: 0168-9002. DOI: [dx.doi.org/10.1016/S0168-9002\(01\)00399-0](https://doi.org/dx.doi.org/10.1016/S0168-9002(01)00399-0) (cit. on p. 23).
- [35] Ralf Nyholm et al. “A soft X-ray monochromator for the MAX synchrotron radiation facility”. In: *Nuclear Instruments and Methods in Physics Research Section A: Accelerators, Spectrometers, Detectors and Associated Equipment* 246.1 (1986), pp. 267–271. ISSN: 0168-9002. DOI: [dx.doi.org/10.1016/0168-9002\(86\)90088-4](https://doi.org/dx.doi.org/10.1016/0168-9002(86)90088-4) (cit. on p. 24).
- [36] Anton S. Tremsin et al. *Microsphere plate electron multiplier: measurements and modeling*. 1995. DOI: [10.1117/12.218391](https://doi.org/10.1117/12.218391) (cit. on p. 26).
- [37] URL: <http://www.scienta.se> (cit. on p. 27).
- [38] N. Mårtensson et al. “A very high resolution electron spectrometer”. In: *Journal of Electron Spectroscopy and Related Phenomena* 70.2 (1994), pp. 117–128. DOI: [10.1016/0368-2048\(94\)02224-N](https://doi.org/10.1016/0368-2048(94)02224-N) (cit. on pp. 27, 29, 130).

- [39] F. Reinert and S. Hüfner. “Photoemission Spectroscopy with Very High Energy Resolution: Studying the Influence of Electronic Correlations on the Millielectronvolt Scale”. In: *Very High Resolution Photoelectron Spectroscopy*. Ed. by Stefan Hüfner. Berlin, Heidelberg: Springer Berlin Heidelberg, 2007, pp. 13–53. ISBN: 978-3-540-68133-5. DOI: [10.1007/3-540-68133-7_2](https://doi.org/10.1007/3-540-68133-7_2) (cit. on p. 27).
- [40] U. Gelius et al. “A new ESCA instrument with improved surface sensitivity, fast imaging properties and excellent energy resolution”. In: *Journal of Electron Spectroscopy and Related Phenomena* 52 (1990), pp. 747–785. ISSN: 0368-2048. DOI: [dx.doi.org/10.1016/0368-2048\(90\)85063-F](https://doi.org/10.1016/0368-2048(90)85063-F) (cit. on p. 28).
- [41] D. W. Turner et al. *Molecular Photoelectron Spectroscopy*. Wiley-Interscience, London, 1970 (cit. on p. 29).
- [42] G C King et al. “An investigation of the structure near the L 2,3 edges of argon, the M 4,5 edges of krypton and the N 4,5 edges of xenon, using electron impact with high resolution”. In: *Journal of Physics B: Atomic and Molecular Physics* 10.12 (1977), p. 2479 (cit. on p. 29).
- [43] M. Jurvansuu, A. Kivimäki, and S. Aksela. “Inherent lifetime widths of Ar $2p^{-1}$, Kr $3d^{-1}$, Xe $3d^{-1}$, and Xe $4d^{-1}$ states”. In: *Phys. Rev. A* 64 (1 2001), p. 012502. DOI: [10.1103/PhysRevA.64.012502](https://doi.org/10.1103/PhysRevA.64.012502) (cit. on pp. 32, 33).
- [44] GasPhase beamline Tables&Links. *Grating 5 resolution vs Slit sizes*. URL: <http://www.elettra.trieste.it/lightsources/elettra/elettra-beamlines/gas-phase/g5-vs-slits.html> (cit. on pp. 32, 33).
- [45] J. Jauhiainen et al. “A method to determine a transmission correction for electron spectrometers using synchrotron radiation”. In: *Journal of Electron Spectroscopy and Related Phenomena* 69.3 (1994), pp. 181–187. ISSN: 0368-2048. DOI: [dx.doi.org/10.1016/0368-2048\(94\)02197-8](https://doi.org/10.1016/0368-2048(94)02197-8) (cit. on pp. 35, 37).
- [46] Geoffrey R. Hutchison et al. “Intermolecular Charge Transfer between Heterocyclic Oligomers. Effects of Heteroatom and Molecular Packing on Hopping Transport in Organic Semiconductors”. In: *Journal of the American Chemical Society* 127.48 (2005). PMID: 16316233, pp. 16866–16881. DOI: [10.1021/ja0533996](https://doi.org/10.1021/ja0533996) (cit. on p. 40).
- [47] André Moliton and Roger C Hiorns. “Review of electronic and optical properties of semiconducting π -conjugated polymers: applications in optoelectronics”. In: *Polymer International* 53.10 (2004), pp. 1397–1412. ISSN: 1097-0126. DOI: [10.1002/pi.1587](https://doi.org/10.1002/pi.1587) (cit. on p. 40).
- [48] V Myrseth et al. “Adiabatic and vertical carbon 1s ionization energies in representative small molecules”. In: *Journal of Electron Spectroscopy and Related Phenomena* 122.1 (2002), pp. 57–63. ISSN: 0368-2048. DOI: [dx.doi.org/10.1016/S0368-2048\(01\)00321-8](https://doi.org/10.1016/S0368-2048(01)00321-8) (cit. on pp. 41, 57).
- [49] A. Giertz et al. “High resolution C1s and S2p photoelectron spectra of thiophene”. In: *The Journal of Chemical Physics* 117.16 (2002), pp. 7587–7592. DOI: [dx.doi.org/10.1063/1.1508374](https://doi.org/10.1063/1.1508374) (cit. on pp. 41, 42, 52).

- [50] Giovanna Fronzoni et al. “Vibrationally resolved high-resolution NEX-AFS and XPS spectra of phenanthrene and coronene”. In: *The Journal of Chemical Physics* 141.4, 044313 (2014). DOI: [dx.doi.org/10.1063/1.4891221](https://doi.org/10.1063/1.4891221) (cit. on pp. 44, 62).
- [51] M Tronc, G C King, and F H Read. “Carbon K-shell excitation in small molecules by high-resolution electron impact”. In: *Journal of Physics B: Atomic and Molecular Physics* 12.1 (1979), p. 137 (cit. on pp. 46, 58).
- [52] A. P. Hitchcock, J. A. Horsley, and J. Stöhr. “Inner shell excitation of thiophene and thiolane: Gas, solid, and monolayer states”. In: *The Journal of Chemical Physics* 85.9 (1986), pp. 4835–4848 (cit. on p. 48).
- [53] P. Väterlein et al. “Orientation and bonding of thiophene and 2,2'-bithiophene on Ag(111): a combined near edge extended X-ray absorption fine structure and X α scattered-wave study”. In: *Surface Science* 452.1-3 (2000), pp. 20–32. ISSN: 0039-6028. DOI: [dx.doi.org/10.1016/S0039-6028\(00\)00292-2](https://doi.org/10.1016/S0039-6028(00)00292-2) (cit. on p. 50).
- [54] I. Minkov et al. “Core excitations of naphthalene: Vibrational structure versus chemical shifts”. In: *The Journal of Chemical Physics* 121.12 (2004), pp. 5733–5739 (cit. on pp. 55, 59, 60, 65).
- [55] I. Minkov et al. In: *Journal of Physical Chemistry A* 109.1330 (2005) (cit. on pp. 55, 59, 60, 65).
- [56] T. C. W. Mak and J. Trotter. “1. The crystal and molecular structure of biphenylene”. In: *J. Chem. Soc.* (0 1962), pp. 1–8. DOI: [10.1039/JR9620000001](https://doi.org/10.1039/JR9620000001) (cit. on p. 56).
- [57] H.-H. Perkampus. “D. W. Turner: Molecular Photoelectron Spectroscopy. Unter Mitarbeit von C. Baker, A. D. Becker und C. R. Brundle, Wiley-Interscience, John Wiley & Sons Ltd., London, New York, Sydney, Toronto 1970. 386 Seiten. Preis: 140 sh.” In: *Berichte der Bunsengesellschaft für physikalische Chemie* 75.2 (1971), pp. 181–181. ISSN: 0005-9021. DOI: [10.1002/bbpc.19710750223](https://doi.org/10.1002/bbpc.19710750223) (cit. on p. 57).
- [58] Chiara Baldacchini et al. “Molecule–metal interaction of pentacene on copper vicinal surfaces”. In: *Surface Science* 601.13 (2007). International Conference on NANO-Structures Self-Assembling International Conference on NANO-Structures Self-Assembling, pp. 2603 –2606. ISSN: 0039-6028. DOI: [dx.doi.org/10.1016/j.susc.2006.12.016](https://doi.org/10.1016/j.susc.2006.12.016) (cit. on p. 63).
- [59] Norbert Koch et al. “Adsorption-Induced Intramolecular Dipole: Correlating Molecular Conformation and Interface Electronic Structure”. In: *Journal of the American Chemical Society* 130.23 (2008). PMID: 18479108, pp. 7300–7304. DOI: [10.1021/ja800286k](https://doi.org/10.1021/ja800286k) (cit. on p. 63).
- [60] M. P. Keane et al. In: *Physical Review B* 45 (1992), p. 6390 (cit. on p. 65).
- [61] C. Enkvist et al. In: *Journal of Chemical Physics* 103 (1995), p. 63333 (cit. on p. 65).
- [62] Christer Enkvist et al. “C_{1s} shakeup spectrum of C₆₀: Global charge-transfer satellites and their relation to the x-ray threshold singularities in macroscopic systems”. In: *Phys. Rev. B* 48 (19 1993), pp. 14629–14637. DOI: [10.1103/PhysRevB.48.14629](https://doi.org/10.1103/PhysRevB.48.14629) (cit. on p. 65).

- [63] M. P. Seah and W. A. Dench. “Quantitative electron spectroscopy of surfaces: A standard data base for electron inelastic mean free paths in solids”. In: *Surface and Interface Analysis* 1.1 (1979), pp. 2–11. ISSN: 1096-9918. DOI: [10.1002/sia.740010103](https://doi.org/10.1002/sia.740010103) (cit. on p. 66).
- [64] John Åhlund et al. “The electronic structure of iron phthalocyanine probed by photoelectron and x-ray absorption spectroscopies and density functional theory calculations”. In: *The Journal of Chemical Physics* 125.3, 034709 (2006). DOI: [dx.doi.org/10.1063/1.2212404](https://doi.org/dx.doi.org/10.1063/1.2212404) (cit. on pp. 67, 99, 108, 115).
- [65] Ieva Bidermane et al. “Characterization of gas phase iron phthalocyanine with X-ray photoelectron and absorption spectroscopies”. In: *physica status solidi (b)* 252.6 (2015), pp. 1259–1265. ISSN: 1521-3951. DOI: [10.1002/pssb.201451147](https://doi.org/10.1002/pssb.201451147) (cit. on p. 68).
- [66] C. Kolczewski et al. “Detailed study of pyridine at the C1s and N1s ionization thresholds: The influence of the vibrational fine structure”. In: *The Journal of Chemical Physics* 115.14 (2001), pp. 6426–6437. DOI: [dx.doi.org/10.1063/1.1397797](https://doi.org/dx.doi.org/10.1063/1.1397797) (cit. on pp. 72, 74, 76–78).
- [67] W. Eberhardt et al. “Fine structure at the carbon 1s K edge in vapours of simple hydrocarbons”. In: *Chemical Physics Letters* 40.2 (1976), pp. 180–184. ISSN: 0009-2614. DOI: [dx.doi.org/10.1016/0009-2614\(76\)85054-3](https://doi.org/dx.doi.org/10.1016/0009-2614(76)85054-3) (cit. on p. 72).
- [68] A.P. Hitchcock and C.E. Brion. “Carbon K-shell excitation of C₂H₂, C₂H₄, C₂H₆ and C₆H₆ by 2.5 keV electron impact”. In: *Journal of Electron Spectroscopy and Related Phenomena* 10.3 (1977), pp. 317–330. ISSN: 0368-2048. DOI: [dx.doi.org/10.1016/0368-2048\(77\)85029-9](https://doi.org/dx.doi.org/10.1016/0368-2048(77)85029-9) (cit. on p. 72).
- [69] Hans Ågren et al. “Direct, atomic orbital, static exchange calculations of photoabsorption spectra of large molecules and clusters”. In: *Chemical Physics Letters* 222.1 (1994), pp. 75–81. ISSN: 0009-2614. DOI: [dx.doi.org/10.1016/0009-2614\(94\)00318-1](https://doi.org/dx.doi.org/10.1016/0009-2614(94)00318-1) (cit. on p. 72).
- [70] M Stener, G Fronzoni, and M de Simone. “Time dependent density functional theory of core electrons excitations”. In: *Chemical Physics Letters* 373.1–2 (2003), pp. 115–123. ISSN: 0009-2614. DOI: [dx.doi.org/10.1016/S0009-2614\(03\)00543-8](https://doi.org/dx.doi.org/10.1016/S0009-2614(03)00543-8) (cit. on pp. 72, 73).
- [71] Vincenzo Barone et al. “Implementation and validation of a multi-purpose virtual spectrometer for large systems in complex environments”. In: *Phys. Chem. Chem. Phys.* 14 (36 2012), pp. 12404–12422. DOI: [10.1039/C2CP41006K](https://doi.org/10.1039/C2CP41006K) (cit. on p. 73).
- [72] Alberto Baiardi, Julien Bloino, and Vincenzo Barone. “General Time Dependent Approach to Vibronic Spectroscopy Including Franck–Condon, Herzberg–Teller, and Duschinsky Effects”. In: *Journal of Chemical Theory and Computation* 9.9 (2013). PMID: 26592403, pp. 4097–4115. DOI: [10.1021/ct400450k](https://doi.org/10.1021/ct400450k). eprint: <http://dx.doi.org/10.1021/ct400450k> (cit. on p. 73).

- [73] G. Vall-llosera et al. “The C 1s and N 1s near edge x-ray absorption fine structure spectra of five azabenzenes in the gas phase”. In: *The Journal of Chemical Physics* 128.4, 044316 (2008). DOI: [dx.doi.org/10.1063/1.2822985](https://doi.org/10.1063/1.2822985) (cit. on pp. 74, 76, 78).
- [74] M. Romeo et al. “N1s and C1s Near-Edge X-ray Absorption Fine Structure Spectra of Model Systems for Pyridine on Si(100): A DFT Simulation”. In: *The Journal of Physical Chemistry C* 118.2 (2014), pp. 1049–1061. DOI: [10.1021/jp409846m](https://doi.org/10.1021/jp409846m) (cit. on p. 74).
- [75] Alberto Baiardi et al. “Vibrationally resolved NEXAFS at C and N K-edges of pyridine, 2-fluoropyridine and 2,6-difluoropyridine: A combined experimental and theoretical assessment”. In: *The Journal of Chemical Physics* 143.20, 204102 (2015). DOI: [dx.doi.org/10.1063/1.4935715](https://doi.org/10.1063/1.4935715) (cit. on pp. 77, 78).
- [76] Fabrizio Santoro et al. “Effective method for the computation of optical spectra of large molecules at finite temperature including the Duschinsky and Herzberg–Teller effect: The Qx band of porphyrin as a case study”. In: *The Journal of Chemical Physics* 128.22, 224311 (2008). DOI: [dx.doi.org/10.1063/1.2929846](https://doi.org/10.1063/1.2929846) (cit. on p. 82).
- [77] Junhua Wang et al. “Magnetization and magnetic anisotropy of metallophthalocyanine molecules from the first principles calculations”. In: *Applied Physics Letters* 94.12, 122502 (2009). DOI: [dx.doi.org/10.1063/1.3100783](https://doi.org/10.1063/1.3100783) (cit. on pp. 88, 97).
- [78] M. Grobosch et al. “Engineering of the Energy Level Alignment at Organic Semiconductor Interfaces by Intramolecular Degrees of Freedom: Transition Metal Phthalocyanines”. In: *The Journal of Physical Chemistry C* 113.30 (2009), pp. 13219–13222. DOI: [10.1021/jp901731y](https://doi.org/10.1021/jp901731y) (cit. on pp. 88–90).
- [79] Barbara Brena et al. “Valence-band electronic structure of iron phthalocyanine: An experimental and theoretical photoelectron spectroscopy study”. In: *The Journal of Chemical Physics* 134.7, 074312 (2011). DOI: [dx.doi.org/10.1063/1.3554212](https://doi.org/10.1063/1.3554212) (cit. on pp. 88, 89).
- [80] Iulia Emilia Brumboiu et al. “Elucidating the 3d Electronic Configuration in Manganese Phthalocyanine”. In: *The Journal of Physical Chemistry A* 118.5 (2014). PMID: 24428172, pp. 927–932. DOI: [10.1021/jp4100747](https://doi.org/10.1021/jp4100747) (cit. on pp. 88–90).
- [81] Kazunari Yoshizawa. “An Orbital Rule for Electron Transport in Molecules”. In: *Accounts of Chemical Research* 45.9 (2012). PMID: 22698647, pp. 1612–1621. DOI: [10.1021/ar300075f](https://doi.org/10.1021/ar300075f) (cit. on p. 88).
- [82] I. Bidermane et al. “Atomic contributions to the valence band photoelectron spectra of metal-free, iron and manganese phthalocyanines”. In: *Journal of Electron Spectroscopy and Related Phenomena* 205 (2015), pp. 92–97. ISSN: 0368-2048. DOI: [dx.doi.org/10.1016/j.elspec.2015.09.004](https://doi.org/10.1016/j.elspec.2015.09.004) (cit. on p. 89).
- [83] I. Bidermane et al. “Experimental and theoretical study of electronic structure of lutetium bi-phthalocyanine”. English. In: *J. Chem. Phys.* 138.23 (2013). ISSN: 0021-9606 (cit. on pp. 89, 115).

- [84] I. Bidermane et al. “When the Grafting of Double Decker Phthalocyanines on Si(100)-2 x 1 Partly Affects the Molecular Electronic Structure”. In: *The Journal of Physical Chemistry C* 120.26 (2016), pp. 14270–14276. DOI: [10.1021/acs.jpcc.6b05552](https://doi.org/10.1021/acs.jpcc.6b05552) (cit. on pp. 89, 119, 140).
- [85] R. Kraus, M. Grobosch, and M. Knupfer. “Full electronic excitation spectrum of condensed manganese phthalocyanine”. In: *Chemical Physics Letters* 469.1–3 (2009), pp. 121–124. ISSN: 0009-2614. DOI: [10.1016/j.cplett.2008.12.090](https://doi.org/10.1016/j.cplett.2008.12.090) (cit. on p. 92).
- [86] J. Berkowitz. “Photoelectron spectroscopy of phthalocyanine vapors”. In: *The Journal of Chemical Physics* 70.6 (1979), pp. 2819–2828. DOI: [dx.doi.org/10.1063/1.437867](https://doi.org/10.1063/1.437867) (cit. on p. 92).
- [87] Artur F. Izmaylov, Gustavo E. Scuseria, and Michael J. Frisch. “Efficient evaluation of short-range Hartree-Fock exchange in large molecules and periodic systems”. In: *The Journal of Chemical Physics* 125.10, 104103 (2006). DOI: [dx.doi.org/10.1063/1.2347713](https://doi.org/10.1063/1.2347713) (cit. on p. 93).
- [88] Vicente Parra et al. “On the effect of ammonia and wet atmospheres on the conducting properties of different lutetium bisphthalocyanine thin films”. In: *Thin Solid Films* 516.24 (2008). The Tenth European Conference on Organised Films (ECOF-10), pp. 9012–9019. ISSN: 0040-6090. DOI: [dx.doi.org/10.1016/j.tsf.2007.11.092](https://doi.org/10.1016/j.tsf.2007.11.092) (cit. on p. 99).
- [89] J. Brunet et al. “An optimised gas sensor microsystem for accurate and real-time measurement of nitrogen dioxide at ppb level”. In: *Sensors and Actuators B: Chemical* 134.2 (2008), pp. 632–639. ISSN: 0925-4005. DOI: [dx.doi.org/10.1016/j.snb.2008.06.010](https://doi.org/10.1016/j.snb.2008.06.010) (cit. on p. 99).
- [90] J. D. Baran et al. “Theoretical and experimental comparison of SnPc, PbPc, and CoPc adsorption on Ag(111)”. In: *Phys. Rev. B* 81 (7 2010), p. 075413. DOI: [10.1103/PhysRevB.81.075413](https://doi.org/10.1103/PhysRevB.81.075413) (cit. on p. 99).
- [91] Katharina Nilson et al. “Rubidium Doped Metal-Free Phthalocyanine Monolayer Structures on Au(111)”. In: *The Journal of Physical Chemistry C* 114.28 (2010), pp. 12166–12172 (cit. on p. 99).
- [92] E. Salomon et al. “Lead Phthalocyanine Films by Near Edge X-ray Absorption Fine Structure Spectroscopy”. In: *The Journal of Physical Chemistry C* 111.33 (2007), pp. 12467–12471. DOI: [10.1021/jp073373w](https://doi.org/10.1021/jp073373w) (cit. on p. 99).
- [93] R. P. Berkelaar et al. “Molecular Bridges”. In: *The Journal of Physical Chemistry C* 115.5 (2011), pp. 2268–2272. DOI: [dx.doi.org/10.1021/jp1105967](https://doi.org/10.1021/jp1105967) (cit. on p. 99).
- [94] S. Boudet et al. “Growth mode and self-organization of LuPc₂ on Si(001)-2 x 1 vicinal surfaces: An optical investigation”. In: *Phys. Rev. B* 86 (11 2012), p. 115413. DOI: [10.1103/PhysRevB.86.115413](https://doi.org/10.1103/PhysRevB.86.115413) (cit. on p. 99).
- [95] Falko Seidel et al. “Spectroscopic ellipsometry and reflection anisotropy spectroscopy of lutetium diphthalocyanine films on silicon”. In: *physica status solidi (c)* 7.2 (2010), pp. 222–226. ISSN: 1610-1642. DOI: [10.1002/pssc.200982464](https://doi.org/10.1002/pssc.200982464) (cit. on p. 99).

- [96] Li Wang et al. “Molecular Orientation and Ordering during Initial Growth of Copper Phthalocyanine on Si(111)”. In: *The Journal of Physical Chemistry C* 11.8 (2007), pp. 3454–3458. DOI: [10.1021/jp066600n](https://doi.org/10.1021/jp066600n) (cit. on p. 100).
- [97] B. N. Holland et al. “Adsorption of lead phthalocyanine on the hydrogen-passivated Ge(001)-2x1 surface”. In: *physica status solidi (c)* 7.2 (2010), pp. 218–221. ISSN: 1610-1642. DOI: [10.1002/pssc.200982463](https://doi.org/10.1002/pssc.200982463) (cit. on p. 100).
- [98] J. Gardener et al. “A scanning tunnelling microscopy investigation into the initial stages of copper phthalocyanine growth on passivated silicon surfaces”. In: *Surface Science* 602.4 (2008), pp. 843–851. ISSN: 0039-6028. DOI: [dx.doi.org/10.1016/j.susc.2007.11.031](https://doi.org/dx.doi.org/10.1016/j.susc.2007.11.031) (cit. on p. 100).
- [99] Y Borensztein and N Witkowski. “Optical response of clean and hydrogen-covered vicinal Si(001) 2 x 1 surfaces”. In: *Journal of Physics: Condensed Matter* 16.39 (2004), S4301 (cit. on p. 101).
- [100] C. Mathieu et al. “Nitrogen 1s NEXAFS and XPS spectroscopy of NH₃-saturated Si(001)-2 × 1: Theoretical predictions and experimental observations at 300 K”. In: *Phys. Rev. B* 79 (20 2009), p. 205317. DOI: [10.1103/PhysRevB.79.205317](https://doi.org/10.1103/PhysRevB.79.205317) (cit. on pp. 100, 101).
- [101] R.I.G. Uhrberg, E. Landemark, and Y.-C. Chao. “High-resolution core-level studies of silicon surfaces”. In: *Journal of Electron Spectroscopy and Related Phenomena* 75 (1995), pp. 197–207. ISSN: 0368-2048. DOI: [dx.doi.org/10.1016/0368-2048\(95\)02538-3](https://doi.org/dx.doi.org/10.1016/0368-2048(95)02538-3) (cit. on p. 101).
- [102] H. W. Yeom et al. “High-resolution core-level study of initial oxygen adsorption on Si(001): Surface stoichiometry and anomalous Si 2p core-level shifts”. In: *Phys. Rev. B* 59 (16 1999), R10413–R10416. DOI: [10.1103/PhysRevB.59.R10413](https://doi.org/10.1103/PhysRevB.59.R10413) (cit. on p. 101).
- [103] Marius Toader et al. “Initial Growth of Lutetium(III) Bis-phthalocyanine on Ag(111) Surface”. In: *Journal of the American Chemical Society* 133.14 (2011), pp. 5538–5544. DOI: [10.1021/ja200168a](https://doi.org/10.1021/ja200168a) (cit. on p. 101).
- [104] Lars Smykalla, Pavel Shukrynau, and Michael Hietschold. “Investigation of Ultrathin Layers of Bis(phthalocyaninato)lutetium(III) on Graphite”. In: *The Journal of Physical Chemistry C* 116.14 (2012), pp. 8008–8013. DOI: [10.1021/jp208363x](https://doi.org/10.1021/jp208363x) (cit. on p. 103).
- [105] Barbara Brena et al. “Equivalent core-hole time-dependent density functional theory calculations of carbon 1s shake-up states of phthalocyanine”. In: *Phys. Rev. B* 70 (19 2004), p. 195214. DOI: [10.1103/PhysRevB.70.195214](https://doi.org/10.1103/PhysRevB.70.195214) (cit. on p. 103).
- [106] A. De Cian et al. “Synthesis, Structure, and Spectroscopic and Magnetic-properties of Lutetium(iii) Phthalocyanine Derivatives - Lupc2.ch2cl2 and [lupc(oac)(h2o)2].h2o.2ch3oh”. In: *Inorg. Chem.* 24 (1985), p. 3162 (cit. on p. 107).
- [107] L. Triguero, L. G. M. Pettersson, and H. Ågren. “Calculations of near-edge x-ray-absorption spectra of gas-phase and chemisorbed molecules by means of density-functional and transition-potential theory”. In: *Phys. Rev. B* 58 (12 1998), pp. 8097–8110. DOI: [10.1103/PhysRevB.58.8097](https://doi.org/10.1103/PhysRevB.58.8097) (cit. on p. 107).

- [108] Y. Alfredsson et al. In: *J. of Chem. Phys.* 122.21, 214723 (2005), pp. – (cit. on pp. 108, 118).
- [109] M. Bouvet and J. Simon. In: *Chem. Phys. Lett.* 172 (1990), pp. 299–302 (cit. on p. 111).
- [110] G. Kresse and J. Hafner. “Ab initio”. In: *Phys. Rev. B* 48 (17 1993), pp. 13115–13118. DOI: [10.1103/PhysRevB.48.13115](https://doi.org/10.1103/PhysRevB.48.13115) (cit. on p. 112).
- [111] G. Kresse and J. Hafner. “Ab initio”. In: *Phys. Rev. B* 49 (20 1994), pp. 14251–14269. DOI: [10.1103/PhysRevB.49.14251](https://doi.org/10.1103/PhysRevB.49.14251) (cit. on p. 112).
- [112] G. Kresse and J. Furthmüller. “Efficiency of ab-initio total energy calculations for metals and semiconductors using a plane-wave basis set”. In: *Computational Materials Science* 6.1 (1996), pp. 15–50. ISSN: 0927-0256. DOI: [dx.doi.org/10.1016/0927-0256\(96\)00008-0](https://dx.doi.org/10.1016/0927-0256(96)00008-0) (cit. on p. 112).
- [113] G. Kresse and J. Furthmüller. “Efficient iterative schemes for ab initio total-energy calculations using a plane-wave basis set”. In: *Phys. Rev. B* 54 (16 1996), pp. 11169–11186. DOI: [10.1103/PhysRevB.54.11169](https://doi.org/10.1103/PhysRevB.54.11169) (cit. on p. 112).
- [114] P. E. Blöchl. “Projector augmented-wave method”. In: *Phys. Rev. B* 50 (24 1994), pp. 17953–17979. DOI: [10.1103/PhysRevB.50.17953](https://doi.org/10.1103/PhysRevB.50.17953) (cit. on p. 112).
- [115] G. Kresse and D. Joubert. “From ultrasoft pseudopotentials to the projector augmented-wave method”. In: *Phys. Rev. B* 59 (3 1999), pp. 1758–1775. DOI: [10.1103/PhysRevB.59.1758](https://doi.org/10.1103/PhysRevB.59.1758) (cit. on p. 112).
- [116] John P. Perdew, Kieron Burke, and Matthias Ernzerhof. “Generalized Gradient Approximation Made Simple”. In: *Phys. Rev. Lett.* 77 (18 1996), pp. 3865–3868. DOI: [10.1103/PhysRevLett.77.3865](https://doi.org/10.1103/PhysRevLett.77.3865) (cit. on p. 112).
- [117] Alexandre Tkatchenko and Matthias Scheffler. “Accurate Molecular Van Der Waals Interactions from Ground-State Electron Density and Free-Atom Reference Data”. In: *Phys. Rev. Lett.* 102 (7 2009), p. 073005 (cit. on p. 112).
- [118] B. I. Craig and P. V. Smith. In: *Surf. Sci.* 276 (1992), p. 174 (cit. on p. 113).
- [119] J. L. Cabellos et al. “Understanding Charge Transfer in Donor-Acceptor / Metal Systems: A Combined Theoretical and Experimental Study”. In: *J. Phys. Chem. C* 116.34 (2012), pp. 17991–18001. DOI: [10.1021/jp3004213](https://doi.org/10.1021/jp3004213) (cit. on p. 118).
- [120] T. Pfeifer, C. Spielmann, and G. Gerber. “Femtosecond x-ray science”. In: *Reports on Progress in Physics* 69.2 (2006), pp. 443–505. DOI: [10.1088/0034-4885/69/2/R04](https://doi.org/10.1088/0034-4885/69/2/R04) (cit. on p. 121).
- [121] Z. Chang et al. “Generation of coherent soft X Rays at 2.7 nm using high harmonics”. In: *Physical Review Letters* 79.16 (1997), pp. 2967–2970 (cit. on pp. 121, 123).
- [122] Ch. Spielmann et al. “Generation of coherent x-rays in the water window using 5-femtosecond laser pulses”. In: *Science* 278.5338 (1997), pp. 661–664. DOI: [10.1126/science.278.5338.661](https://doi.org/10.1126/science.278.5338.661) (cit. on pp. 121, 123).

- [123] E. Seres et al. “Generation of coherent soft-X-ray radiation extending far beyond the titanium L edge”. In: *Physical Review Letters* 92.16 (2004), pp. 163002–1. DOI: [10.1103/PhysRevLett.92.163002](https://doi.org/10.1103/PhysRevLett.92.163002) (cit. on pp. 121, 123).
- [124] E. Allaria et al. In: *Nature Photon.* 6.10 (2012), pp. 699–704 (cit. on p. 122).
- [125] AllariaE. et al. “Two-stage seeded soft-X-ray free-electron laser”. In: *Nat Photon* 7.11 (Nov. 2013), pp. 913–918 (cit. on p. 122).
- [126] L. Giannessi et al. In: *FEL 2012 - 34th International Free Electron Laser Conference* (2012), pp. 13–18 (cit. on p. 122).
- [127] E. Allaria et al. In: *J. Synchrotron Radiat.* same issue (2015) (cit. on p. 122).
- [128] P.B. Corkum. In: *Phys. Rev. Lett.* 71 (1993) (cit. on p. 123).
- [129] P. B. Corkum and Ferenc Krausz. “Attosecond science”. In: *Nat Phys* 3.6 (June 2007), pp. 381–387 (cit. on p. 123).
- [130] URL: <http://www.ita-slo.eu> (cit. on p. 124).
- [131] URL: <http://www.elettra.trieste.it/lightsources/fermi/fermi-beamlines/ldm/ldmhome-page.html> (cit. on p. 124).
- [132] L. Poletto et al. “Double-configuration grating monochromator for extreme-ultraviolet ultrafast pulses”. In: *Applied Optics* 53.26 (2014), pp. 5879–5888. DOI: [10.1364/AO.53.005879](https://doi.org/10.1364/AO.53.005879) (cit. on p. 126).
- [133] L. Poletto et al. In: *Rev. Sci. Instrum.* 80 (2009), p. 123109 (cit. on p. 126).
- [134] F. Frassetto et al. “Single-grating monochromator for extreme-ultraviolet ultrashort pulses”. In: *Optics Express* 19.20 (2011), pp. 19169–19181. DOI: [10.1364/OE.19.019169](https://doi.org/10.1364/OE.19.019169) (cit. on p. 126).
- [135] L. Poletto and F. Frassetto. “Time-preserving grating monochromators for ultrafast extreme-ultraviolet pulses”. In: *Applied Optics* 49.28 (2010), pp. 5465–5473. DOI: [10.1364/AO.49.005465](https://doi.org/10.1364/AO.49.005465) (cit. on p. 126).
- [136] L. Poletto and F. Frassetto. In: *Appl. Sci.* 3 (2013), p. 1 (cit. on p. 126).
- [137] T.E. Glover et al. “Observation of laser assisted photoelectric effect and femtosecond high order harmonic radiation”. In: *Physical Review Letters* 76.14 (1996), pp. 2468–2471 (cit. on p. 129).
- [138] E.S. Toma et al. “Ponderomotive streaking of the ionization potential as a method for measuring pulse durations in the XUV domain with fs resolution”. In: *Physical Review A - Atomic, Molecular, and Optical Physics* 62.6 (2000), pp. 061801–061801. DOI: [10.1103/PhysRevA.62.061801](https://doi.org/10.1103/PhysRevA.62.061801) (cit. on p. 129).
- [139] D. Gibbs et al. “Polarization and resonance properties of magnetic X-ray scattering in holmium”. In: *Physical Review Letters* 61.10 (1988), pp. 1241–1244. DOI: [10.1103/PhysRevLett.61.1241](https://doi.org/10.1103/PhysRevLett.61.1241) (cit. on p. 131).
- [140] J.P. Hannon et al. “X-ray resonance exchange scattering”. In: *Physical Review Letters* 61.10 (1988), pp. 1245–1248. DOI: [10.1103/PhysRevLett.61.1245](https://doi.org/10.1103/PhysRevLett.61.1245) (cit. on p. 131).

- [141] M. Sacchi et al. “Ultrahigh-vacuum soft x-ray reflectometer”. In: *Review of Scientific Instruments* 74.5 (2003), pp. 2791–2795. DOI: [10.1063/1.1568552](https://doi.org/10.1063/1.1568552) (cit. on p. 131).
- [142] P.N. Argyres. “Theory of the Faraday and Kerr effects in ferromagnetics”. In: *Physical Review* 97.2 (1955), pp. 334–345. DOI: [10.1103/PhysRev.97.334](https://doi.org/10.1103/PhysRev.97.334) (cit. on p. 132).
- [143] E. Beaupaire et al. “Ultrafast spin dynamics in ferromagnetic nickel”. In: *Physical Review Letters* 76.22 (1996), pp. 4250–4253 (cit. on p. 132).
- [144] V Lyamayev et al. In: *J. Phys. B* 46 (2013), p. 164007 (cit. on p. 133).
- [145] M. Zangrando et al. In: *Rev. Sci. Instrum.* 80.11 (2009), p. 113110 (cit. on p. 133).
- [146] C. Svetina et al. In: *Proc. SPIE* 8139 (2011), 81390J. DOI: [10.1117/12.892707](https://doi.org/10.1117/12.892707) (cit. on p. 133).
- [147] L. Raimondi et al. In: *Nucl. Instrum. Methods A* 710 (2013), pp. 131–138 (cit. on p. 135).
- [148] P. Kirkpatrick and A. V. Baez. In: *J. Opt. Soc. America* 38 (1948), pp. 766–773 (cit. on p. 135).
- [149] P. O’Keeffe et al. In: *Nucl. Instr. Meth. B* 284 (2012), p. 69 (cit. on p. 136).
- [150] A. A. Sorokin et al. “Photoelectric Effect at Ultrahigh Intensities”. In: *Phys. Rev. Lett.* 99 (21 2007), p. 213002. DOI: [10.1103/PhysRevLett.99.213002](https://doi.org/10.1103/PhysRevLett.99.213002) (cit. on p. 137).
- [151] S. Mondal et al. “Photoelectron angular distributions for the two-photon sequential double ionization of xenon by ultrashort extreme ultraviolet free electron laser pulses”. In: *J. Phys. B* 46.16 (2013), p. 164022. DOI: [10.1088/0953-4075/46/16/164022](https://doi.org/10.1088/0953-4075/46/16/164022) (cit. on p. 137).
- [152] P. Cinquegrana et al. In: *Phys. Rev. ST Accel. Beams* 17 (2014), p. 040702 (cit. on p. 137).
- [153] Maurizio D’Auria et al. “Synthetic Approach to and Characterization of a Fullerene–DTBT–Fullerene Triad”. In: *Synlett* 24.08 (2013), pp. 943–946. DOI: [10.1055/s-0032-1316902](https://doi.org/10.1055/s-0032-1316902) (cit. on p. 139).
- [154] A. Guarnaccio et al. “Thiophene-Based Oligomers Interacting with Silver Surfaces and the Role of a Condensed Benzene Ring”. In: *The Journal of Physical Chemistry C* 120.1 (2016), pp. 252–264. DOI: [10.1021/acs.jpcc.5b08733](https://doi.org/10.1021/acs.jpcc.5b08733). eprint: <http://dx.doi.org/10.1021/acs.jpcc.5b08733> (cit. on p. 139).
- [155] Jun Chen, John C. Wenger, and Dean S. Venables. “Near-Ultraviolet Absorption Cross Sections of Nitrophenols and Their Potential Influence on Tropospheric Oxidation Capacity”. In: *The Journal of Physical Chemistry A* 115.44 (2011). PMID: 21958133, pp. 12235–12242. DOI: [10.1021/jp206929r](https://doi.org/10.1021/jp206929r). eprint: <http://dx.doi.org/10.1021/jp206929r> (cit. on p. 141).
- [156] Iustinian Bejan et al. “The photolysis of ortho-nitrophenols: a new gas phase source of HONO”. In: *Phys. Chem. Chem. Phys.* 8 (17 2006), pp. 2028–2035. DOI: [10.1039/B516590C](https://doi.org/10.1039/B516590C) (cit. on p. 141).

- [157] Hanna A. Ernst et al. “Ultrafast Dynamics of o-Nitrophenol: An Experimental and Theoretical Study”. In: *The Journal of Physical Chemistry A* 119.35 (2015). PMID: 26266823, pp. 9225–9235. DOI: [10.1021/acs.jpca.5b04900](https://doi.org/10.1021/acs.jpca.5b04900). eprint: <http://dx.doi.org/10.1021/acs.jpca.5b04900> (cit. on p. 142).
- [158] Tsunetoshi Kobayashi and Saburo Nagakura. “Photoelectron spectra of nitrophenols and nitroanisoles”. In: *Journal of Electron Spectroscopy and Related Phenomena* 6.5 (1975), pp. 421–427. ISSN: 0368-2048. DOI: [dx.doi.org/10.1016/0368-2048\(75\)80029-6](https://doi.org/10.1016/0368-2048(75)80029-6) (cit. on p. 143).
- [159] M. Coreno et al. to be published (cit. on p. 143).